UNIVERSITY OF CALIFORNIA

Los Angeles

Modeling the reactivity of Chemical Warfare Agents on metal oxides using computational chemistry methods

A thesis submitted in partial satisfaction

of the requirements for the degree Master of Science

in Chemical Engineering

by

Celine Tesvara

2021

ABSTRACT OF THE THESIS

Modeling the reactivity of Chemical Warfare Agents on metal oxides using computational chemistry methods

by

Celine Tesvara

Master of Science in Chemical Engineering

University of California, Los Angeles, 2021

Professor Philippe Sautet, Chair

To design efficient personal protective equipment against chemical warfare agents, there is a need to understand the fundamental pathway of decomposition of these chemicals on solid surfaces. In this thesis, the author investigates such pathways by employing computational chemistry methods, namely density functional theory (DFT) in link with experimental results obtained by temperature-programmed desorption (TPD), scanning tunneling microscopy (STM), and X-ray Photoelectron Spectroscopy (XPS).

The thesis is divided into three parts, with the first part focused on the thermodynamic analysis of dimethyl methyl phosphonate (DMMP), a simulant of the nerve agent Sarin, interaction on Fe_3O_4(111) films grown on a Fe_2O_3(0001) crystal. DFT calculations reveal that dissociative adsorption of DMMP on Fe_3O_4(111) is very stable, which dissociates DMMP to surface methoxy and methyl methylphosphonate (MMP). Collaborative result of TPD and DFT shows three decomposition channels of DMMP: self-rearrangement of MMP to produce dimethyl ether (DME) at 600 K, surface methoxy disproportion reaction to produce CH_3OH and CH_2O at 700 K, and combustion of the remaining carbon-containing intermediates at 850 K. It was found that the dynamic interaction between Fe_3O_4 and subsurface Fe_2O_3 films results in dimethyl ether as an additional product, a behavior that is unique to this surface.

The second part deals with elucidating the oxidative decomposition pathways of DMMP on pristine and defective rutile TiO_2(110). Pathway searches were performed with the Nudged Elastic Band (NEB) method. Rate constants from Transition State Theory (TST) show that the decomposition of DMMP is slow. DMMP decomposes via O-CH_3 bond cleavage on the pristine surface and P-OCH_3 bond cleavage on the surface with oxygen vacancy, both cleavages happening at 600 K. Thermodynamic analyses show that P-CH_3 bond cleavage of DMMP on pristine and defective surfaces are unlikely. We found that the presence of O vacancy facilitates P-OCH_3 bond cleavage, adding another possible channel for active surface methoxy species creation.

The last part investigates the decomposition of sarin on selected pathways over r-TiO_2(110) to determine if DMMP is an adequate simulant of sarin. We conclude that the chemistry of DMMP does resemble Sarin's well if only P-O_{alko} and O-C bond cleavages are considered, whereas P-F bond dissociation may show a different reactivity not seen on DMMP.

The thesis of Celine Tesvara is approved.

Panagiotis Christofides

Dante Simonetti

Philippe Sautet, Committee Chair

University of California, Los Angeles

2021

Acknowledgments

I would like to express my sincere gratitude to my adviser, Dr. Philippe Sautet, for his time, valuable insights, and patience. Without his support and tutelage, this work would have been impossible for me to complete. I thank Dr. Panagiotis Christofides and Dr. Dante Simonetti for their technical support to oversee my thesis. I would also like to acknowledge the Defense Thread Reduction Agency for the funding needed to complete this study.

Lastly, I would like to dedicate this work and express my thanks to my parents and sister. This is for you, for always supporting my dreams.

Table of Contents

Abstract ii

Committee page iii

Acknowledgments iv

Table of Contents v

List of Tables vii

List of Figures viii

1. Introduction 1

1.1. Motivation 1

1.2. Chemical warfare agents 2

1.2.1. Nerve agents: History and Mechanism 2

1.2.2. Sarin and its simulant 6

1.2.3. Sarin chemistry in the environment 7

1.3. Metal Oxides 8

1.3.1. Interaction of CWA and metal oxides 9

1.3.2. Iron oxide: $Fe_3O_4(111)$ 11

1.3.3. Titanium dioxide: $TiO_2(110)$ 15

2. Methods and Theoretical backgrounds: Density Functional Theory (DFT) 20

2.1. From the Schroedinger equation to DFT 20

2.2. Hubbard U Correction 22

2.3. Appendices 22

3. Results 23

3.1. Part 1: Thermodynamic analysis of dimethyl methylphosphonate DMMP on $Fe_3O_4(111)/Fe_2O_3(0001)$ 23

3.1.1. Computational method 23

3.1.2. Experimental Method 24

3.1.3. Experimental Results: Temperature Programmed Desorption and Scanning Tunneling Microscopy 24

3.1.4. Computational Results: DMMP adsorption modes and decomposition channel 27

3.1.5. Discussion: Thermodynamic analysis 29

3.1.6. Conclusion 32

3.1.7. Acknowledgments 32

3.2. Part 2: Elucidating decomposition pathway of DMMP and Sarin on pristine and defective r-TiO_2(110) 33
3.2.1. Computational method 33
3.2.2. Experimental methods 34
3.2.3. Experimental results: Temperature Programmed Desorption 35
3.2.4. DMMP adsorption and decomposition pathway on pristine r-TiO_2(110) 37
3.2.4.1. DMMP adsorption modes on the pristine surface 37
3.2.4.2. Decomposition on Pristine surface: P-O_{II} bond cleavage-initiated 37
3.2.4.3. Decomposition on the pristine surface: O-CH_3 bond cleavage-initiated 39
3.2.4.4. Decomposition on the pristine surface: P-CH_3 bond cleavage-initiated 42
3.2.5. DMMP adsorption and decomposition pathway on defective r-TiO_2(110) 43
3.2.5.1. DMMP adsorption modes on the defective surface 43
3.2.5.2. Decomposition on the defective surface: P-OCH_3 bond cleavage initiated 44
3.2.5.3. Decomposition on the defective surface: O-CH_3 bond cleavage-initiated 48
3.2.5.4. Decomposition on the defective surface: P-CH_3 bond cleavage-initiated 51
3.2.6. Discussion: Possible reaction pathways 51
3.2.7. Conclusion 53
3.3. Part 3: Comparison of DMMP and Sarin chemistries on pristine and defective r-TiO_2(110) on selected pathways 54
3.3.1. Computational Set-up 54
3.3.2. Sarin decomposition pathway on pristine r-TiO_2(110) 54
3.3.2.1. Sarin adsorption modes on the pristine surface 54
3.3.2.2. P-O and P-F bond cleavage initiated path 55
3.3.2.3. O_{alko}-C bond cleavage initiated path 56
3.3.3. Sarin decomposition pathway on defective r-TiO_2(110) 57
3.3.3.1. Sarin adsorption modes on the defective surface 57
3.3.3.2. P-O and P-F bond cleavage initiated path 58
3.3.4. Conclusion 60
4. Final Conclusions & Closing Remarks 61

List of Tables

Table 1 Selected list of sarin Hydrolysis products and their sources. Data are curated from Munro et. al.[42] 8

Table 2 Selected properties of Iron Oxide bulk phases.[84] 11

Table 3 Selected bulk parameter of TiO_2 polymorphs. 15

Table 4 Stable molecular adsorption modes and adsorption energies of DMMP on Fe_3O_4(111). 28

Table 5 The three energies of dissociative adsorption conformations along with their adsorption energy relative to gas-phase DMMP 29

Table 6 Calculated energies and kinetic rate constants for DMMP decomposition on the pristine r-TiO_2(110) surface via P-OCH_3 cleavage 39

Table 7 Kinetic rate constants on DMMP decomposition on the pristine surface via O-C bond cleavage 42

Table 8 Calculated energies and kinetic rate constants for DMMP decomposition on the defective r-TiO2(110) surface via O-PCH_3 bond cleavage. 48

Table 9 Calculated energies and kinetic rate constants for DMMP decomposition on the defective r-TiO2(110) surface via O-C bond cleavage 50

List of Figures

Figure 1 Chemical Structure of G-Series agents. 4

Figure 2 Base chemical structure of V-series agents and list of all alkyl groups contained within each species of V-series agents. 5

Figure 3 Acetylcholine chemical structure 6

Figure 4 Similarities between the nerve agent Sarin (top) and its simulant dimethyl methylphosphonate (DMMP, bottom). 7

Figure 5 Bulk structure of Fe_3O_4. Fe_3O_4 possesses the inverse spinel structure. 12

Figure 6 Crystal Field Theory Diagram of Fe^{2+} at octahedral sites. The image has been reproduced from Parkinson et. al.[84] 13

Figure 7 All possible terminations on Fe_3O_4(111) surface. 14

Figure 8 Stability diagram of Fe_3O_4(111) surface comparing the 6 different termination modes. Surfaces with defects (dashed line) are also considered here. Image is taken from Noh et.al.[100] 14

Figure 9 Unit cell representation of anatase (a, c) and rutile (b, d).[132] 16

Figure 10 (Left), the Bulk structure of Rutile showcasing the octahedra packing. (Right) Stable termination of r-TiO_2 (110). Indicate atom colors. 17

Figure 11 r-TiO_2(110) surface with the assignment of the atom types (A). Experimental STM images obtained from Sanchez et. al.[140] **Bright protrusions correspond to O2c rows (B). Simulated STM images using PBE+U, U=4.2 eV (C).** 17

Figure 12 (Top) Side and perspective views of Fe_3O_4 slab model. (Bottom) Surface with ¼ ML O coverage. Blue represents Fe atoms and red represents Oxygen atoms. Each supercell contains 4 surface-tetrahedral Fe. 24

Figure 13 Temperature Programmed Desorption Spectra of DMMP thermal decomposition on Fe_3O_4(111)/Fe_2O_3(0001) films. Data obtained after exposure of DMMP to full saturation at 1.0 x 10^{-9} torr for 1 minute. There are 3 main decomposition channels at 600, 700, and 850 K. 25

Figure 14 Scanning Tunneling Microscopy images of (A) the pristine Fe_3O_4(111) thin-film containing both O adatoms and tetrahedral coordinated lattice Fe; (B) surface after exposure to DMMP (7.5×10^{-9} Torr for 60 s) at 300 K; and (C) formation of P-containing islands heating to 750 K. The images were obtained at room temperature with a tunneling current of 0.02 nA and a bias of −2.2 V 26

Figure 15 TPD spectra of the fully saturated sample with DMMP which is then dosed with water prior to reaction (A). TPD spectra of the surface first dosed with water prior to adsorption of DMMP and thermal reaction (B). 27

Figure 16 Molecular adsorption geometries of DMMP on Fe_3O_4(111) and important distances. (1) DMMP adsorbing via OCH_3 group with surface Fe (Fe-OCH_3). (2) DMMP adsorbing via P=O-Fe. 28

Figure 17 Different MMP and methoxy configurations on the Fe_3O_4(111) surface with an oxygen adatom. The respective energies are displayed in Table 5. 29

Figure 18 Possible DME formation pathway from dissociative adsorbed DMMP. Direct self-rearrangement of MMP to produce DME is thermodynamically not possible (path a). Intermediates upon DME production may be stabilized by additional oxygen adatom (path b). 31

Figure 19 Thermodynamic analysis of additional O-adatom obtained from the reduction of hematite to produce Intermediate b on phosphor-containing intermediate upon release of DME. .. 31

Figure 20 Rutile TiO_2(110) Surface Model. (Left) Top view of pristine TiO_2 (110) and (Right) Top view of defect TiO_2(110) with an O_{2c} oxygen vacancy (indicated by a broken line circle, since a subsurface O atom is seen below at the same x,y position). 34

Figure 21 TPD spectra of thermal decomposition of DMMP on reduced TiO_2(110). DMMP desorbs molecularly from the surface between 200 K and 500 K. Simultaneous formation of methanol and formaldehyde fits the temperature of methoxy disproportionation previously observed on TiO_2(110) surface.[203] 36

Figure 22 The Auger electron spectrum of the TiO_2(110) single crystal after a temperature-programmed desorption experiment shows that phosphorous and carbon on the surface indicating residual P-containing species on the surface that is assigned to a DMMP reaction. The elements are identified by their characteristic Auger peak energies: P at 110 eV, C at 272 eV, Ti at 387, and 418 eV and O at 503 eV. 36

Figure 23 Two most stable molecular adsorption geometries of DMMP in TiO_2(110). Most stable adsorption (left) has adsorption energy of -2.35 eV. The second most stable adsorption geometry (right) has an adsorption energy of -1.71 eV. 37

Figure 24 Transition State to 1st P-O bond cleavage of DMMP on pristine TiO_2(110). Bond distances are: P-O_{2c} =1.69 Å, P-O_I =1.60 Å, P-O_{II} =2.02 Å, Ti-O_{II}=2.16 Å and Ti-O_I =1.89 Å. 38

Figure 25 Reaction pathway of DMMP on pristine TiO_2(110) starting by the P-OCH_3 bond cleavage. The reaction proceeds either by breaking a second P-OCH_3 or an O-CH_3 bond. 39

Figure 26 Reaction pathway of DMMP on pristine TiO_2 (110) via O_{II}-C_{II} and O_{III}-C_{III} bond cleavage. Intermediates of decomposition initiated with O_{II}-C_{II} cleavage are highlighted in green boxes (path a), whereas intermediates of decomposition initiated with O_{III}-C_{III} (path b) 41

Figure 27 (top) Dissociative DMMP adsorption via cleavage of P-CH_3 bond, leaving a methyl group on surface O_{2c}. (bottom) dissociated DMMP intermediate upon additional cleavage of P-OCH_3 bond. This system is less stable since P is undercoordinated. 43

Figure 28 Most stable molecular DMMP adsorption on TiO_2(110) with oxygen vacancy. O_I occupies the oxygen vacancy with an extra interaction of a DMMP methoxy group with surface Ti5c. 44

Figure 29 Intermediate isomers upon P-O_{II} bond cleavage on defective TiO_2(110). (left) the methoxy substituent of MMP is facing away from the adsorbed methoxy, decomposition steps follow the 'green pathway'. (right) the methoxy substituent is facing towards the adsorbed methoxy, decomposition steps follow the 'blue pathway'. 45

Figure 30 DMMP decomposition initiated via P-O_{II} bond cleavage on r-TiO_2(110) with one O vacancy. Intermediates in green and blue depict decomposition following two possible isomers after P-OII bond cleavage. 46

Figure 31 (Left) Transition state of P-O cleavage for green isomer, (right) transition state for blue isomer. 47

Figure 32 (left) green pathway intermediate upon second P-O bond cleavage. (right) isomer in the blue pathway 47

Figure 33 DMMP decomposition initiated via P-O_{II} bond cleavage. Intermediates in green and blue depict decomposition following two possible isomers after P-O_{II} bond cleavage. 49

Figure 34 Intermediates from P-O bond cleavage after O-C bond cleavage on the defective surface. (Left) P-O_{II} bond dissociation from S2a (right) PO_{III} bond dissociation from S2b 50

Figure 35 (left) Molecularly adsorbed DMMP on O vacancy. (Right) Subsequent intermediate resulting from P-C bond cleavage. 51

Figure 36 Most stable molecular sarin adsorption geometries 54

Figure 37 Sarin decomposition on pristine TiO_2(110), following the P-O bond cleavage initiated pathway. 55

Figure 38 Sarin decomposition on pristine TiO_2(110) initiated with P-F bond cleavage. 56

Figure 39 O-C bond cleavage on molecularly adsorbed sarin on pristine TiO_2 (110). 57

Figure 40 Stable molecular adsorption of sarin on defective TiO2(110) surface. 58

Figure 41 Decomposition pathway of Sarin on defective TiO_2(110) initiated via P-O_{alko} bond cleavage. 59

Figure 42 Thermodynamic analysis of P-F bond cleavage of Sarin on the defective surface. 60

1. Introduction

1.1. Motivation

Events such as the terrorist attack of Tokyo subway in 1995[1,2] and most recently the Kahn Shaykhun attack in the Syrian civil war in 2017[3] have served to be alarming reminders that chemical warfare agents (CWA) still possess a great risk even to this modern day. Both events involve the use of a deadly nerve agent called Sarin as a weapon in public places which cause the fatalities of 12 people (with 6200 people injured) and 89 people, respectively. The high fatality of CWA gave rise to the Chemical Weapons Convention which prohibits countries that signed and ratified it to produce, develop or stockpile such chemicals and their precursor.[4] The United States is among the countries that ratified the Chemical Weapon Convention and has been actively putting efforts towards disposal and decontamination of CWA.

Consequently, the handling and site decontamination of chemical warfare agents (CWA) demand good and reliable personal protective equipment for officials and civilians.[2,5] In addition to its potency, CWA are known to be persistent in the environment, thus it may possess a risk that may last for days in the case of leakage or attack. For example, a report by the CIA indicates sarin used in Iraq to have a shelf life of a few weeks. Such a long shelf-life in public settings may pose a continuous danger towards civilian and on-duty officers after initial exposure. To design effective personal protective equipment, molecular understanding of the chemistry of CWA is of importance. Effort must be prioritized towards searching materials that can absorb a large concentration of CWA strongly and facilitate its decomposition towards safe, non-toxic products.

Metal oxides are deemed as good candidate materials to help facilitate the decomposition of CWA. On top of their low cost of production and abundance, metal oxides form porous polycrystalline layers that may help 'trap' various organic molecules.[6,7] Reasoning behind this is that metal oxide is known to have a high surface area, suitable for maximum saturation on molecule adsorption. Past studies on metal oxides such as MgO, CaO, Fe_3O_4, Al_2O_3, and TiO_2, for example, demonstrate that metal oxides are able to capture the product of CWA decomposition, particularly the class of nerve agents.[7–13] On the other hand, similarly built semiconductor metal oxides such as SnO_2, ZnO, CuO, InO_3, and WO_3 for example, have long been used as the base materials for gas sensing of chemical warfare agents, adding to the hypothesis that metal oxides are good candidates as the base material for personal protective equipment for personnel.[14–16] However, we have yet to understand the key molecular interaction between CWA and metal oxides. Elucidating molecular interaction between CWA and these surfaces may give us important information in designing more efficient PPE in the future.

In this work, we are interested in bridging the gap between experimental and theoretical knowledge on how CWA interacts with metal oxides. Due to the toxicity of the CWA, the use of computational chemistry is convenient to help interpret experimental results. Additional experimental methods such as temperature-programmed desorption (TPD), scanning tunneling microscopy (STM), and

x-ray photoelectron spectroscopy (XPS), obtained in collaboration, will also be employed to further validate our results.

The following section will start with a short review of chemical warfare agents, their history, and chemistry in nature along with the current scientific understanding of their interaction with metal oxide.

1.2. Chemical warfare agents

Chemical warfare agents (CWA) constitute extremely hazardous chemical compounds that are used to inflict mass destruction towards their victims. The use of CWA was first identified in World War I, where Germany employed chlorine as a weapon to subdue their enemies.[17] Since then, large-scale researches to invent more effective and lethal chemicals for large-scale production has been performed to fulfill the demand of war. While the use and thus the threats of CWA were mainly confined within the military during the World War I and II era, current rising events such as terrorism bring the concern of such threats towards civilians as well.

Chemical warfare agents are commonly classified depending on the target organs being damaged. Several established classes are:[18]

- Nerve Agents: work by disrupting the nerve signals, causing malfunction of organs and muscles.
- Vesicant/Blistering agents: targets the skin of the victims, causing high-level burn degrees/injuries.
- Cyanogenic agents: disrupt blood's energy utilization.
- Pulmonary agents: damage respiratory system (often referred to as the 'choke agents')
- Tear gases: (disruption of visual)
- Psychomimetic agents: hallucinogens and cytotoxins which cause an impaired sense of sight and hearing.[19,20]

Amongst all agents, nerve agents are considered to be the most deadly and persistent amongst agents. Therefore, we propose to put nerve agent as the focus of this study.

1.2.1. Nerve agents: History and Mechanism

Nerve agents belong to a class of organophosphates that disrupt the release of neurotransmitters to the brain if inhaled, causing fatal muscle and organ spasms and eventually, total shutdown of the body of the inhaler. Nerve agents found their most prevalent use in WWII. However, it was not utilized again until the Iraq invasion of Iran in 1981 which causes almost 100,000 Iranian casualties. In 1995 Iraq admitted to the use of Nerve Agents in the war.[21] In the same year, The United States agreed and signed the Chemical Weapon Convention which states that all nations must report their possession of chemical weapons and promptly destroy all their remaining stockpiles.[22,23]

History

The first class of nerve agents called the G-series (G stands for Germany) was initially discovered as an attempt to find superior pesticides. The first of its kind, Tabun, was discovered by Dr. Gerhard Schrader.[24] Upon a leak incident, Dr. Schrader realized that tabun has the ability to induce nerve poisoning within minutes. Due to a part of the Nazi decree in 1935 which requires all possible discoveries beneficial to the military to be reported, Dr. Schrader was invited due to the interesting tabun sample that he had sent. In 1939, a plant at Munster-Lager to produce tabun was established with a capacity of 10,000 tons. As a result of WWII demand, in 1942, the facility was able to produce 30,000 tons of tabun per year. This marks the first mass production of Germany's first nerve agent.[25] Future inventions of nerve agents would put this agent into two major classes, the G-series and V-series.

G-series

Following the success of Tabun, Schrader synthesized a more lethal sister of tabun, named Sarin. Sarin itself was an acronym of the scientist who took a great role in developing it: Schrader, Ambrose, Rudringer, and van der L"in"de. The last of the series, Soman, was synthesized by Dr. Richard Kuhn. Upon the capturing of the production facilities, enemies found the codenames of Tabun, Sarin, and Soman listed as GA, GB, and GD respectively. On an interesting note, GC was deliberately skipped as it represents the medical code for gonorrhea. GA, GB, GD, and later GF (cyclosarin) were the result of weapon research led by Dr. Schrader. These 4 chemicals complete the G-series and its naming is still used as official codenames by NATO.

Chemical structure-wise, all the chemicals in the G-series are organophosphorus compounds exhibiting the $O=P(OR^1)R^2R^3$ formula. The latter developed G-series compounds after tabun (GA), namely soman (GB), sarin (GD), and cyclosarin (GF), resemble each other the most with one of the OR substituents being fluorine, and the other being a type of alkoxy group. The difference between soman, sarin, and cyclosarin lies only in their OR group, with soman substituted with 3-3-dimethyl-2butoxy (O-C6H10), sarin with an isopropoxy (O-iPr) group, and cyclosarin with cyclohexoxy. In the case of Tabun, aside from the P=O bond, the central phosphor is interacting with dimethylamine, propyne, and ethoxy. G-series compounds are colorless and odorless liquid, though there are reports suggesting tabun having a fruity smell.[26]

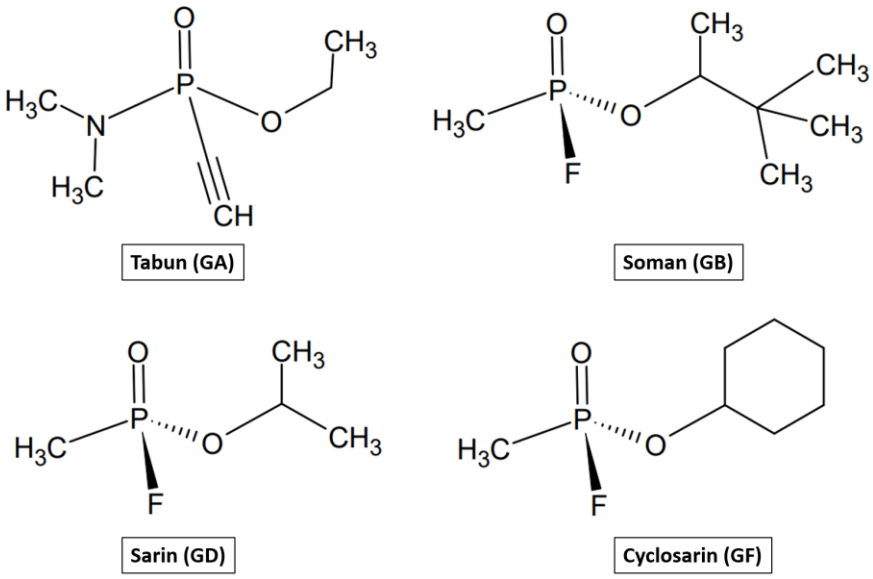

Figure 1 Chemical Structure of G-Series agents.

V-series

The second series developed in 1952 after the G-series is called V-series (V stands for 'Venomous').[18,27] The first of the series, VX was discovered accidentally by a British chemist Dr. Ranajit Ghosh while he was trying to develop an effective pesticide to replace DDT.[26,28] However, since England already had its hand full of the production of the G-series agent, England decided to pass down the formula to the United States. In 1960, the US completes its first mass-production plant of VX in Newport, Indiana. However, the lethality of VX impacted not only the enemies but also US soldiers. In 1968, VX leaked from a military spray tank in Utah, subsequently injured herds and animals in the area. The looming leakage threat forces President Richard Nixon to pass a mandate forcing the stoppage of all chemical weapon production and testing. [26] The formula that the British passed down to the US somehow leaked during the war and the Soviets were able to concoct their version of VX, namely VR-55 (V'R' for Russia). There is little historical information for the rest of the V-series agents namely VE, VG, VM, and VS.[29]

Similar to G-series, the V-series agents are colorless and odorless liquids. The chemical formula of all agents in the V-series are similar, with all compounds following O=P(R_1)(O-R_2)(S-C2H4-X). Complete branch variations between the V-series are listed in table x, taken from the Encyclopedia of Toxicology by Moyer et.al.

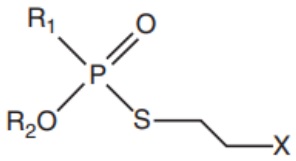

	X	R_1	R_2
VE	$-N(C_2H_5)_2$	$-C_2H_5$	$-C_2H_5$
VG	$-N(C_2H_5)_2$	$-OC_2H_5$	$-C_2H_5$
VM	$-N(C_2H_5)_2$	$-CH_3$	$-C_2H_5$
VR	$-N(C_2H_5)_2$	$-CH_3$	$-CH_2CH(CH_3)_2$
VS	$-N(CH(CH_3)_2)_2$	$-C_2H_5$	$-C_2H_5$

Figure 2 Base chemical structure of V-series agents and list of all alkyl groups contained within each species of V-series agents.

Mechanism of Action

A person inflicted with nerve agents would show signs of nerve system failure within minutes. According to CDC, initial physical symptoms such as miosis (excessive constriction of the pupil), headache, convulsions, restlessness, fainting, and coma. Simultaneously one might experience nausea, abdominal pain, shortness of breath, profuse sweating, and tears. Finally, the muscle will weaken (often with small contractions under the skin) before finally progressing to paralysis. A paralyzed victim is in danger as their organs and cardiovascular function are malfunctioning, causing unpredictable or decreasing heart rate, effectively cutting all lifeline for organs.

The potency of nerve agents relates to the central atom of its molecular structure, phosphor, which specifically takes the form of phosphonates, where the central phosphor is bonded to two alkoxy groups (O-R) an alkyl/halogen group (R, or halogens) and an oxygen (=O). are known to undergo irreversible reactions with acetylcholinesterase (AChE), an enzyme in the human's nervous system that is responsible to transmit neurotransmitters via catalytic reactions with acetylcholine. Acetylcholine is an ester of acetic acid and choline that acts as signals messenger between muscles and brains in many living organisms. Phosphonates readily react with AChE and inhibit its acetylcholine receptor sites via phosphorylation which causes a build-up of acetylcholine in the nervous system. Such build-up of acetylcholine may overstimulate the muscle (involuntary jolting and breakdown), followed by paralysis of muscle, including muscles that are responsible for maintaining organ functions.[18,30,31]

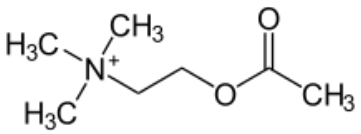

Figure 3 Acetylcholine chemical structure

1.2.2. Sarin and its simulant

Sarin and its simulant DMMP

Sarin is a highly toxic organophosphorus gas and is a member of the nerve agent family namely the series-G (GB). It is an odorless, tasteless and colorless liquid, rendering it the perfect chemical weapon to catch the enemy off guard.[32] Victims who inhale Sarin might face death between one to ten minutes of inhalation.[33] The lethal concentration of Sarin in the air was found between 28-35 mg/m^3, which is very small considering human lungs exchange 15 L of air in only one minute. In comparison to chlorine and cyanide, sarin is found to be 543 and 26 times more lethal. With vapor pressure and volatility of 2.1 mmHg and 22000 mg/m^3, respectively, at 20°C, Sarin is the most volatile nerve agents, making it most lethal due to the ease of inhalation.[27]

Sarin's chemical formula is $C_4H_{10}FO_2P$, or $O=PF(OC_3H_7)(CH_3)$. In this case, the central phosphor is bound tetrahedrally to 4 groups: double-bonded to an oxygen atom, fluorine, a methyl, and an isopropoxide (O-i-Pr) group (fig. 4). Due to the safety risk of Sarin, experimental studies more often than not substitute sarin with a simulant, namely dimethyl methylphosphonate (DMMP).[7,34–36] DMMP chemical structure is $C_3H_9O_3P$. Structurally akin to sarin, DMMP is an organophosphorus compound with $O=P(OR)_2R$ chemical structure. However, in analogous to the fluorine and isopropoxide of sarin, the phosphor center of DMMP is instead bonded with two methoxys ($-OCH_3$). The absence of fluorine in DMMP is deemed to be the reason why DMMP is non-toxic in comparison to sarin. DMMP itself is usually used as a flame retardant or precursor for other phosphonates.[37,38]

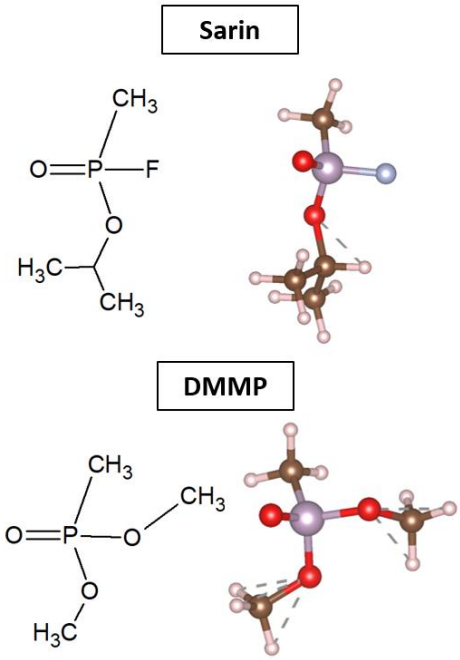

Figure 4 Similarities between the nerve agent Sarin (top) and its simulant dimethyl methylphosphonate (DMMP, bottom).

The similarity of organic groups presents between sarin and DMMP base the argument that this simulant should display similar chemistry, though the chemical pathways might not be fully identical. Particularly in the case of DMMP/Sarin, the absence of F on DMMP may not depict the decomposition pathway that Sarin undergoes as halogen groups are generally more sensitive towards certain reaction pathways. In this thesis, we will investigate whether DMMP exhibits similar chemistry as Sarin for thermal decomposition on an oxide surface.

1.2.3. Sarin chemistry in the environment

When Sarin is exposed to air, it is thus exposed to different gasses such as H_2O, O_2, and other contaminants. The decomposition of sarin may depend accordingly via these interactions between gasses persisting in air. Liquid sarin is miscible with water, with the addition of the presence of a fluoride group (-F) sarin may be subject to immediate basic and acidic hydrolysis. The hydrolysis half-life of Sarin at 20°C and PH of 7 was found to be 8.5 hrs.[27,39] Past investigations showed that hydrolysis is always initiated via the P-F bond cleavage to create fluoride acid and isopropyl methyl phosphonic acid (IMPA)[40,41], although the kinetics depends on several parameters such as temperature, PH, and humidity. Another hydrolysis pathway less commonly found includes the loss of isopropanol, producing methyl phosphonic acid (MPA) instead. Table 1 lists all possible Sarin hydrolysis products, taken from the work of Munro, Small, and Rosenblatt.[42–44] A review by Munro et. al. suggests that alkaline hydrolysis leads to sarin preferring the loss of isopropanol during hydrolysis.[42] On the other hand, Rosenblatt et. al suggest that acidic hydrolysis is more

advantageous as it leads to a shorter half-life of sarin. At 20°C, Rosenblatt found that the half-life of sarin may reach 461 hours at PH of 6.5, in comparison to only 46 hours at PH of 7.5.[44,45]

Fate in water

Due to Sarin having a very low Henry's constant of $5.4 \times \frac{10^{-7} atm}{m^3 mol}$, no volatilization from water is observed. Interestingly, a work by Demek and Epstein found that the presence of ions such as hypochlorite in water speeds up the hydrolysis of sarin.[46]

Following research on metal, cations suggest that sarin hydrolysis may be accelerated.[26] This is corroborated by the same study by Rosenblatt on the effect of pH that suggests that ions in solutions accelerate the hydrolysis of Sarin.

Fate of products

All Sarin hydrolysis products are non-toxic and highly stable. With vapor pressure of 0.0034 mmHg for IMPA, there is a negligible chance of the decomposition products contaminating the air at atmospheric pressure. Additionally, IMPA has a half-life of 1900 years at room temperature and pressure. IMPA is also resistant to bacterial degradation, rendering it inactive and non-toxic species safe for the environment. [44,45,47]

Table 1 Selected list of sarin Hydrolysis products and their sources. Data are curated from Munro et. al.[42]

Name of Products	Formula	Source
Isopropyl methyl phosphonic acid (IMPA)	$C_4H_{11}PO_3$	Hydrolysis of Sarin
Methylphosphonic acid (MPA)	CH_5PO_3	Hydrolysis of Sarin
Diisopropyl methylphosphonate (DIMP)	$C_7H_{17}PO_3$	Impurity
Diisopropyl Carbodiimide (DIPC)	$C_7H_{14}N_2$	Stabilizer

1.3. Metal Oxides

Metal oxides have recently been gaining quite an interest due to their morphology, electronic, and optical properties for catalysis application. Most metal oxides are low-cost, abundant, and easy to produce materials, in addition to exhibiting Lewis acid-base behavior which could be useful to bind oxygen-containing molecules. Additionally, metal oxide exhibits porous morphologies presenting a large surface area needed to trap the maximum concentration of CWA. As such, metal oxides such as TiO_2, SnO_2, GaO_2, and even WO_3 have been used as gas sensing materials for hazardous gasses such as CO and other larger organic molecules.[6,7,48,49]

This chapter will focus on a brief review of the current work relating to CWA and metal oxide. Then we will present the metal oxides studied in this work, iron oxide (Fe_3O_4) and titanium oxide (r-TiO_2). The review will include the morphologies, magnetic properties, and different terminations available for each system.

1.3.1. Interaction of CWA and metal oxides

As experimentalists often exchange Sarin to its non-toxic simulant, dimethyl methyl ether (DMMP) the following review will put more emphasis on studies on DMMP.

Adsorption modes

Previous experimental studies on DMMP chemistry on metal oxide suggest that adsorption of DMMP is stable and molecular desorption is commonly found up to room temperature. Temperature programmed desorption (TPD) and XPS spectra on DMMP adsorption on CeO_2, CuO, CuO_2, MoO_3, and TiO_2 show that adsorption occurs via the interaction between the oxo oxygen and surface metal cation (P=O-M).[50,51,60,61,52–59] Experimental work on metal oxides often used as semiconductor gate stack or gas sensings such as Al_2O_3, MgO, La_2O_3, SiO_2, and Fe_2O_3 dosed with DMMP analyzed with IR spectroscopy also showed that the adsorption of DMMP does proceed via P=O-M bond.[15,62–64]

Decomposition channel

The decomposition of DMMP in UHV conditions has been studied extensively. Thermal decomposition may happen via the P-OCH_3 or O-CH_3 bond cleavage, depending on the metal oxide substrate. Mitchell et. al. performed an infrared study on DMMP adsorption and decomposition on aluminum, lanthanum, magnesium, and iron oxide (Fe_2O_3). Mitchell discovers that DMMP decomposition follows the cleavage of both DMMP's P-OCH_3 bond, subsequently transferring two methoxys to the surface on the oxides of Al, Mg, and La. Judging from the resulting methanol and formaldehyde products, it was concluded that these products result from the reaction between surface methoxy groups. Interestingly, IR does not seem to see any changes in the P-CH_3 bond. On Fe_2O_3 however, decomposition is more complete; almost all C containing species have been eliminated from P.[62] Another study on Al_2O_3 by Weinberg et. al shows a similar result as the IR study by Mitchell on aluminum oxides with DMMP decomposition initiated with P-OCH_3 bond cleavage, forming a methyl methylphosphonate (MMP) at 295 to 473 K. Above 573 K, MMP loses another methoxy to form tridentate phosphonate species.[65] Common thermal decomposition products include methanol, formaldehyde, carbon dioxide, and carbon monoxide.

On reduced oxide, such as ceria, TPD, XPS, and IRAS study by Chen et. al. on DMMP chemistry showed that P-OCH_3 cleavage happens at around 300-500 K, though product formation (methanol and formaldehyde) was not observed until 575 K. The result indicates that methoxy groups are the reactive intermediates on the surface. P-CH_3 bonds are still intact up to 700 K. Though the reaction cycle can be performed multiple times, signs of poisoning appear until the sorbent is completely dead after the third cycle.[50]

Role of Lewis acid and surface defects

There are indications that Lewis acidity is the determining factor in deciding the stability of chemisorbed DMMP, for example, in the case of MoO_3.[60,66–69] A combination of experimental and

computational work by Head et. al. on oxygen terminated MoO_3 (010), using APXPS (Ambient Pressure X-ray Photoelectron Spectroscopy) and DFT, studied the interaction between DMMP and the surface with several types of defects including oxygen vacancies, hydroxyl group, and hydration effects. Since the surface is oxygen terminated, there is a lack of available Lewis acid sites that can create a strong interaction with DMMP. However, the creation of defects such as oxygen vacancy or hydroxyl may help attract the phosphoryl oxygen of DMMP, creating a weak interaction with the surface. Subsequent decomposition is difficult without the availability of surface hydroxyls. Head et. al. conclude that the accessibility of Lewis acid is crucial as a similar test with CuO(111) containing readily available Lewis acid site shows a strong and reactive decomposition of DMMP immediately upon exposure at room temperature. [70]

Additionally, it has been repeatedly found that DMMP forms good interaction with surface hydroxyl as well. This has been the case for TiO_2, as we will explain in section 1.3.2, anatase exposed to water may form P=O…H interaction with gas-phase DMMP.

Exceptions

Interestingly, various oxides can have distinct reactivity. For example, a Temperature Programmed Desorption (TPD) and Auger Electron Spectroscopy (AES) study of DMMP interaction with SiO_2 indicate no DMMP decomposition other than multilayer adsorption below 295 K. Only 10% decomposition was observed on hydrated SiO_2, which yields CH_3O and methylphosphonate surface species, indicating prior P-O bond cleavage.[57] Within the same work, it was found that the decomposition of α-Fe_2O_3 occurs via oxidation of P-CH_3 bond by lattice oxygen. The remaining phosphor containing product migrates towards the bulk to open active sites for the next reaction cycle. This is different from the case of Ti and Ce where the active sites are quickly poisoned by the remaining phosphor products.

Chosen metal oxides for our study: Fe_3O_4 and TiO_2

Current studies of DMMP decomposition on various metal oxides indicate that the chemistry may differ, depending on the surface oxide. There is a need for theoretical calculations to shed light on the elementary decomposition pathway of DMMP, while simultaneously explaining the effects of surface properties towards the reactivity of chemisorbed DMMP.

From the literature review, few key factors keep arising in determining the strength of the interaction between CWA and metal oxides, namely: (A) the accessibility of surface Lewis acid, (B) the presence of defects such as oxygen vacancies and hydroxyls, (C) the availability of Lewis basic oxygen. It seems that the availability of Lewis acid sites is key to have a strong interaction with DMMP and/or sarin. Factor B is an interesting sector to cover, as each metal oxide exhibits different defects. For example, point defects are very much uncommon on reducible oxides such as TiO_2 or CeO_2. Lastly, it is an interesting point to see the effect of surface oxygen (Lewis base) towards DMMP dissociation.

To address these questions, we have decided to focus on two types of metal oxide surfaces: Fe_3O_4(111) and TiO_2(110). The reasoning being is that both metal oxide terminations exhibit exposed surface Lewis acid metal cation and Lewis basic oxygen and have large surface areas which may help facilitate adsorption and subsequent decomposition of DMMP and sarin.

1.3.2. Iron oxide: Fe_3O_4(111)

Iron oxide is arguably one of the most abundant materials on earth as it forms naturally within the earth's crust. This abundance, coupled with low toxicity, stability, and cheap production cost has made iron oxide a commonly used material for biomedical application (materials for MRI scan)[71–73], the catalyst for Fischer-tropsch[74,75] or dehydrogenation reactions[76–79], or even support for nanoparticles. Several works have evidence of iron oxide helping the reaction through its interaction with the supported nanoparticle.[80–83]

Iron oxide can exist in different phases, the main three being wüstite ($Fe_{1-x}O$), magnetite (Fe_3O_4), and hematite (α-Fe_2O_3). In all phases, the oxygen ion is forming the close-packed lattice, with Fe cation occupying the tetrahedral and octahedral empty spaces. In reducing conditions, iron oxide adopts the wüstite phase, in the oxidizing condition the hematite phase, and magnetite is flexible somewhere in between the reducing and oxidizing condition. Table 2 summarizes the selected properties of iron oxide.[84]

Table 2 Selected properties of Iron Oxide bulk phases.[84]

Iron oxide	Wüstite ($Fe_{1-x}O$)	Magnetite (Fe_3O_4)	Hematite (α-Fe_2O_3)
Metal cation	Fe^{2+}	Fe^{2+} and Fe^{3+}	Fe^{3+}
Structure type	Defect rock salt	Inverse spinel	Corundum
Space Group	Fm3m	Fd3m	R$\bar{3}$c
Anion Structure	FCC	FCC	HCP
Lattice parameter	a=0.430-0.428 nm	a=0.8936 nm	a=0.504, b=1.375
Magnetism	Antiferro	Ferri	Weak Ferro/Ferri

Because magnetite (Fe_3O_4) is a commonly used material to adsorb and remove organophosphate pollutants and pesticides, along with its interesting possible terminations that possess the lewis acid required to attract phosphonates, this review will be focused on magnetite.

Bulk structure of Fe_3O_4

Magnetite bulk adopts the inverse spinel structure. Spinel structures have the AB_2O_4 formula, where usually A^{2+} metal cation adopts the tetrahedral sites, and the B^{3+} metal cation sits on the octahedral sites. However, in the case of Fe_3O_4, the Fe^{2+} (A) metal cation greatly stabilize the system, and thus the Fe^{2+} metal cation sits on the octahedral sites as well, forcing half of Fe^{3+} to occupy the tetrahedral site and making the chemical formula adopt the $Fe^{3+}_{tet}Fe^{2+}_{oct}Fe3^{3+}_{oct}O_4$. This

configuration is commonly known as the *Inverse spinel* structure. Each unit cell of bulk Fe_3O_4 contains 24 Fe and 32 O atoms, which brings it to 8 Fe_{tet}^{3+}, 8 Fe_{oct}^{2+}, 8 Fe_{oct}^{3+} cations per unit cell.

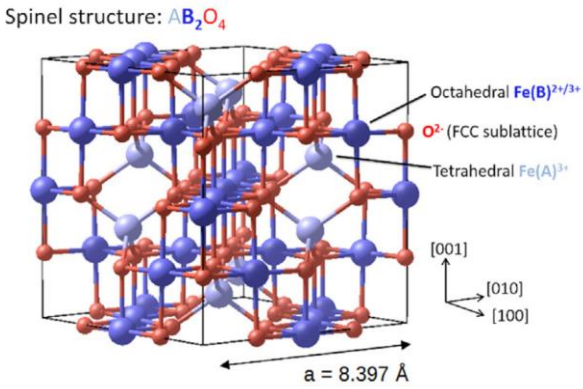

Figure 5 Bulk structure of Fe_3O_4. Fe_3O_4 possesses the inverse spinel structure.

Magnetism

Fe_3O_4 is a ferrimagnetic material stemming from the difference of magnetic moment between the cations occupying the octahedral and tetrahedral sites. The cation that occupies tetrahedral and octahedral sites have a different magnetic moment between each other. Following the $Fe_{tet}^{3+}Fe_{oct}^{2+}Fe3_{oct}^{3+}O_4$ formulation, $Fe_{tet}^{3+}Fe3_{oct}^{3+}$ cation residing in the octahedral site have exact 1:1 ration and thus their magnetic moment cancels each other out. The total magnetic moment of Fe_3O_4 stems from the Fe_{oct}^{2+} cation.[84]

The magnetic moment of Fe_{oct}^{2+} can be trailed back to its d orbitals occupation using crystal field theory. Figure 6 shows the d-orbitals splitting diagram of Fe_{oct}^{2+}. There is an exchange split causing an energy difference of 3.5 eV between orbitals that are occupied by spin up and spin down electrons. Since the Fe in question occupies the octahedral site, the t_{2g} orbitals are more stable by 2 eV in energy, compared to the e_g orbitals. Valence Fe atom had 8 electrons in d-orbital, which makes Fe_{oct}^{2+} to have 6 electrons ready to occupy both t_{2g} and e_g orbitals. 5 out of 6 electrons occupy the more stable spin up t_{2g} and e_g orbitals, with one electron in each orbital. The last electron occupies the spin-down t_{2g} orbital, hence canceling one electron on the spin-up moment. Looking at the diagram, one can predict that the total magnetic moment amount to $4\mu_B$. This agrees well with the experimental measurement of total magnetic moment at $4.07\mu_B$.[85]

The unique magnetic properties of Fe_3O_4 in which the octahedral sites consist of both by Fe_{oct}^{2+} and Fe_{oct}^{3+} equally to result in $Fe_{oct}^{2.5+}$ like behavior may cause some problems in DFT and incorrect prediction of properties. DFT+U method is often employed to correct this charge order. Hubbard U correction around 4 eV is deemed to be suitable to separate and distinguish the two Fe_{oct} cations. The U effective correction value is parameterized to selected properties such as bandgap and phase transition temperatures.[84,86–90]

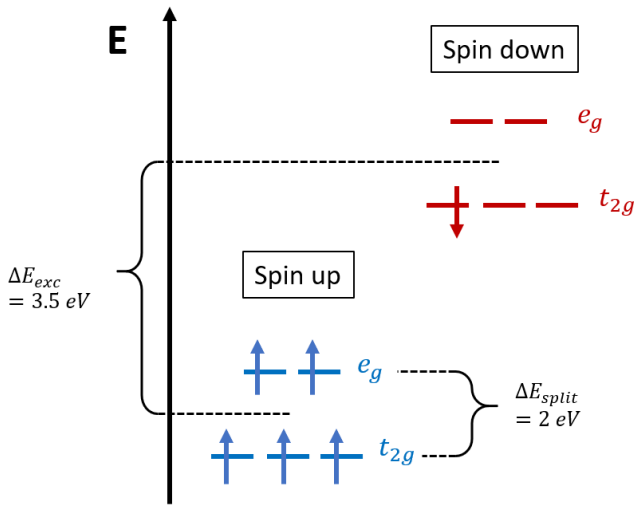

Figure 6 Crystal Field Theory Diagram of Fe^{2+} at octahedral sites. The image has been reproduced from Parkinson et. al.[84]

Surfaces: $Fe_3O_4(111)$

In nature, Fe_3O_4 crystal often exists in (111) facets. Synthetic Fe_3O_4 thin films grown on many different metals including Pt and Au have been shown to prefer the 111 direction during growth.[76,91–95] Nowadays most $Fe_3O_4(111)$ films could also be grown α-$Fe_2O_3(0001)$ single crystals in UHV conditions.[25] LEED experiments on thin films Fe_3O_4 shows that the (111) facet is favored as well.[92–94] DFT calculations, however, predict that the most stable surface facet is the (100) facet, followed by the (111) and the (110) facets.[88,90,96] Due to $Fe_3O_4(111)$ being able to retain its magnetic properties from the bulk, the (111) facet is often being the customary choice material for CWA gas sensing.[76,97]

The $Fe_3O_4(111)$ surface is unique as it has 6 different possible terminations from 3 possible atoms of different coordination: oxygen (O), tetrahedral Fe (Fe_{tet}), and octahedral Fe (Fe_{oct}), each denoted with 1 and 2 annotation due to symmetry placements. The 6 termination planes, named in the order are Fe_{tet1}, O_1, Fe_{oct1}, O_2, Fe_{tet2}, Fe_{oct2}, Fe_{tet1}, O_1, and repeating (figure 7).

Amongst the 6 possible terminations, ab initio thermodynamics and DFT studies have previously been performed to determine the most stable terminations.[86,98–100] It was found from combinations of LEED experiments and DFT that the most stable termination across a huge span of oxygen chemical potentials belongs to the Fe_{tet1} termination in UHV condition. Figure 8 showcase the stability diagram of the 6 different terminations, calculated with the DFT+U method.[100]

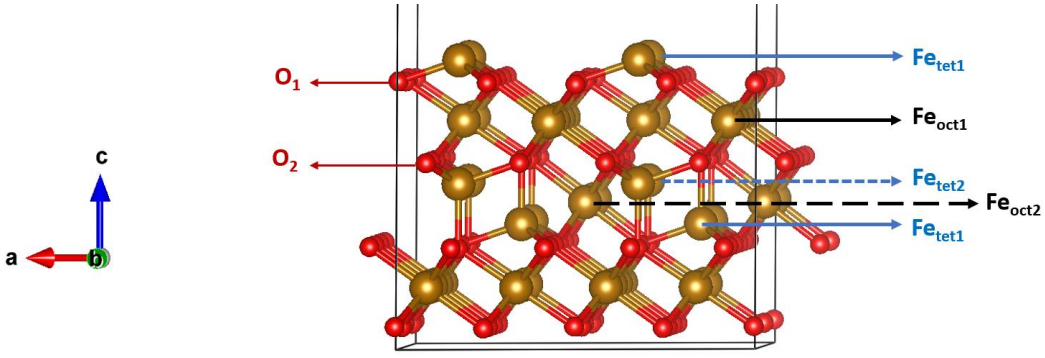

Figure 7 All possible terminations on Fe_3O_4(111) surface.

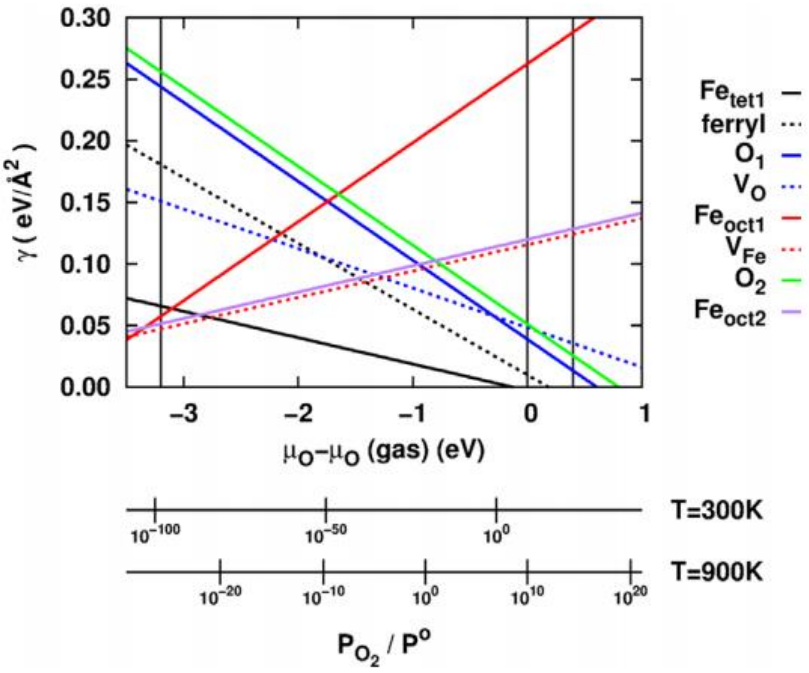

Figure 8 Stability diagram of Fe_3O_4(111) surface comparing the 6 different termination modes. Surfaces with defects (dashed line) are also considered here. Image is taken from Noh et.al. [100]

Fe_3O_4 with DMMP

While there have been few works on Fe_2O_3 to study its interaction with DMMP,[56,57,63] works on Fe_3O_4 are rare. Due to the magnetic properties that Fe_3O_4 possesses, there has been effort to create a bio-assay capable to detect exposure of chemical warfare agents to potential victims.[101,102] Liang et. al. manages to prepare Fe_3O_4 magnetic nanoparticles (MNP) which are capable to sense sarin down to 1 nM sensitivity. Other works have been focused on sensing applications by supporting Fe_3O_4 with metal-organic frameworks such as UiO-66-NH_2.[103,104] However, a detailed account of

the interaction and decomposition of DMMP and/or sarin on Fe_3O_4 is still an open research question in which the author will attempt to answer.

1.3.3. Titanium dioxide: TiO_2(110)

Titanium dioxide (or often called titania) is a material most households known for its use as a white pigment. However, in the scientific field, titania's applications span wide from the world of heterogeneous catalysis (biodiesel production[105]), photocatalysis (water splitting[106–112], solar/photovoltaic cells[113–116], CO_2 reduction[109,117]), to gas sensing[64] and support for active nanoparticles[118–124]. Additionally, recent works have put effort into using titania assisted with UV-light for the degradation of organic molecules.[125–129]

Bulk TiO_2

Titania exists in three crystalline phases: brookite, anatase, and rutile. In general, rutile is the more stable phase in ambient conditions. Anatase and brookite are metastable states, as both can transform irreversibly to rutile at high temperature and pressure. The characteristically high surface area for this metal oxide helps increase its reflectiveness which gives off its white colors.[130,131] Table 3 summarizes key geometric parameters between anatase, rutile, and brookite. Rutile and anatase are the only phases that have been heavily studied and used for industrial applications.

Table 3 Selected bulk parameter of TiO_2 polymorphs.

Phase	Rutile	Anatase	Brookite
Crystal structure	Tetragonal	Tetragonal	Rhobohedrical
Space Group	P4/mnm	I4/amd	Pbca
Lattice parameter [Å]	a=b=4.58 c=2.95	a=b=3.78 c=9.50	a=5.44 b=9.17 c=5.14

The geometric differences between anatase and rutile are not very stark. Both phases possess tetragonal unit cells. An easy way to visualize TiO_2 is to see the crystal as a set of repeating TiO_6 octahedra. One key yet subtle difference between rutile and anatase is the way TiO_6 octahedra is sharing edges. Anatase's TiO_6 is line edges with other TiO_6, whereas TiO_6 octahedra in rutile only share point edges. Due to the edge-sharing, the transformation from rutile to anatase requires bond breaking in the process (fig. 9). Ti^{+4} in anatase sharing edges with 4 other TiO6 gives rise to a slight bent on its equatorial bond in comparison to rutile where all its equatorial bonds are in one plane.[132,133]

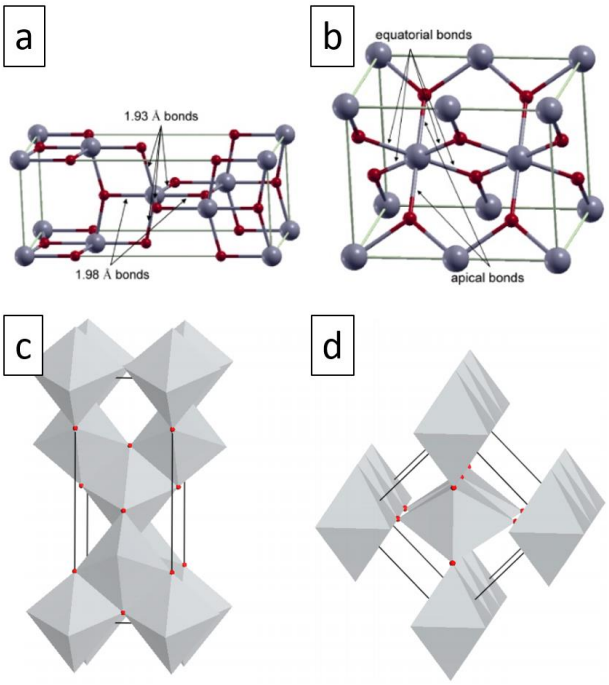

Figure 9 Unit cell representation of anatase (a, c) and rutile (b, d).[132]

Magnetism

TiO_2 is known to be diamagnetic, meaning that it possesses no magnetic moment. This can be explained by the valence of Ti^{4+} cation in bulk TiO_2. Ti has a valence electron of [Ar] 3d2 4s2; thus, the creation of Ti^{4+} brings the Ti valence to be fully octet. Unlike Fe_3O_4, there is no partial occupancy in the d orbitals, and thus TiO_2 does not have any net magnetic moments. However, in the case of small nanoparticles or thin films, experimental measurements can find net magnetic moment up to 7.2 μ_B/nm^2 as a side effect of bulk termination.[134]

r-TiO_2(110) surface

The most stable surface of rutile TiO_2 is the (110) facet.[135] The (110) direction in the rutile bulk shows TiO_6 octahedra stacked vertically and horizontally, in an alternating manner (Fig. 9). There are few ways to terminate the bulk in this direction, though only one termination fully compensates the charges on the surface (see figure 9, dashed lines A and B).[136] This termination has been time and time again observed in many experimental works.[137]

Upon surface cut, 4 different atoms can be identified, denoted by their coordination numbers: Ti_{5c}, Ti_{6c}, O_{2c}, and O3c (see figure 10). On the topmost layer both Ti_{5c} and O_{2c} form alternating rows along [001]. The Ti_{5c} rows are sandwiched between two O_{3c} rows, whereas the Ti_{6c} rows are located beneath O_{2c} rows (O_{2c} rows are often called bridging oxygen rows as well).

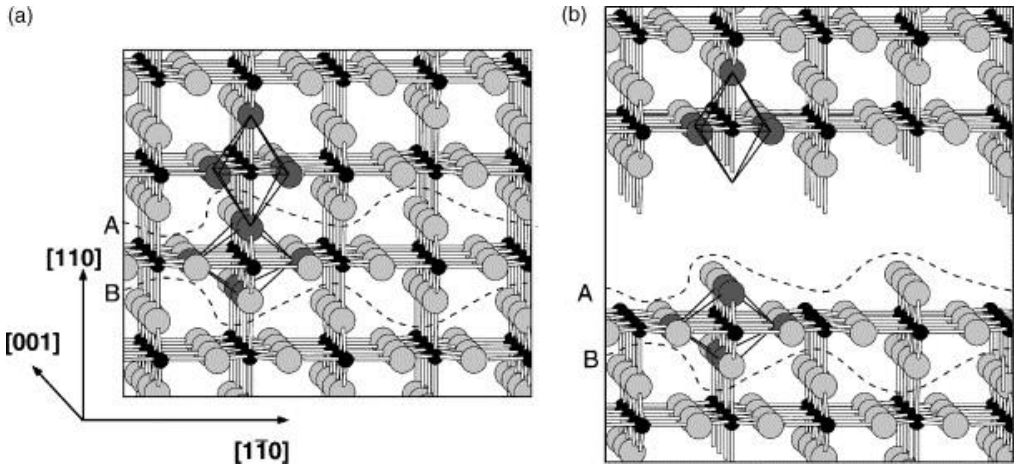

Figure 10 (Left), the Bulk structure of Rutile showcasing the octahedra packing. (Right) Stable termination of r-TiO_2 (110). Indicate atom colors.

Experimental results corroborate the proposed termination plane of r-TiO_2(110). STM work using bias voltage up to 2 V to probe the occupied states shows clear bright protrusion hypothesized to be the O_{2c} rows.[138–141] DFT calculations have been employed to verify this hypothesis. An STM image simulation from our DFT results, and for a bias voltage addressing occupied state, shows bright rows on O_{2c} rows, Ti_{5c} rows are depicted as dark rows, signaling an unoccupied state on the surface.

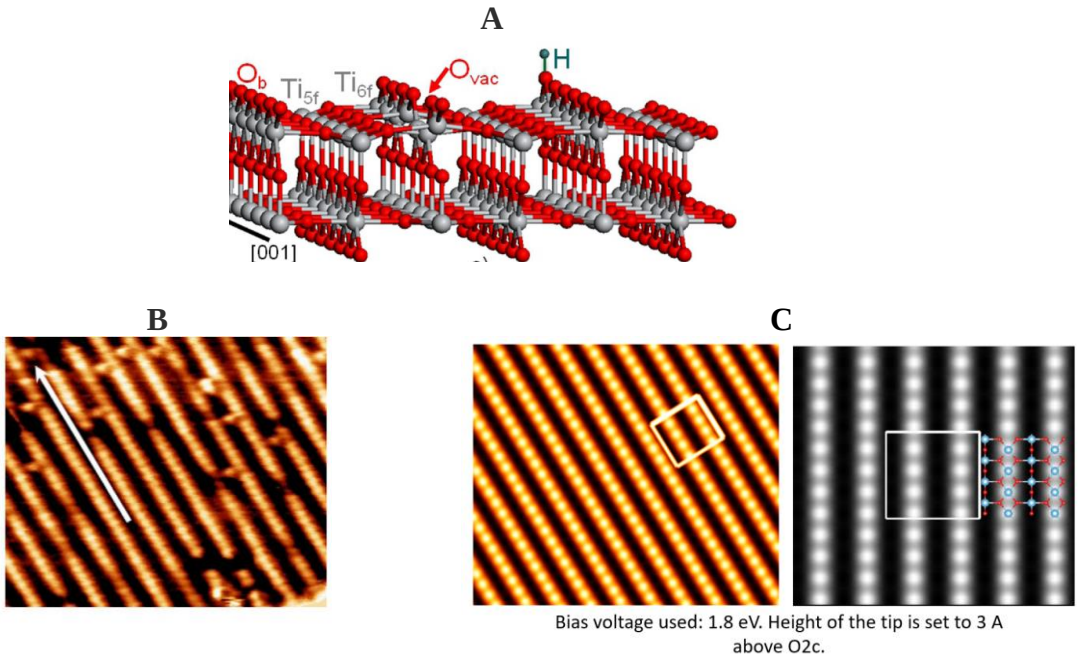

Figure 11 r-TiO_2(110) surface with the assignment of the atom types (A). Experimental STM images obtained from Sanchez et. al.[140] Bright protrusions correspond to O2c rows (B). Simulated STM images using PBE+U, U=4.2 eV (C).

It is known that the r-TiO_2(110) surface exhibits defects in UHV conditions.[136,142–150] Most common and interesting defect pertains to the oxygen vacancies on the bridging oxygen rows. The concentration of these defects is small yet significant; in the range of 9-15% of the surface.[120,138,151,152] Particularly oxygen vacancy has been found to be the active sites for reactions such as oxygen and water dissociation, including CO oxidations.[117,153–155] As we have seen earlier, there are two types of oxygen atoms that are exposed on the r-TiO_2(110) surface, namely the O_{2c} and O_{3c}. It is thermodynamically more favorable to create vacancies in O_{2c} rows.[156–158] These vacancies can also be healed by dosing the sample either with O_2 or H_2O, leaving an extra oxygen adatom on Ti_{5c} or a hydroxylated surface.[159–161] These point defects may have an interesting reactivity towards the chemical warfare agents' decomposition.

DMMP and TiO2

Most work studying the interaction between CWA and TiO_2 is done on commercial TiO_2 powder (Degussa P25). Work on TiO_2 Degussa powders containing hydroxyls (30% rutile and 70% anatase) by Yates et. al. using FTIR shows interesting conclusions, with DMMP adsorbing via P=O group and interaction with surface hydroxyl; this interaction has been previously postulated in the literature.[10,35,49,162] Yates observed P-OCH_3 bond cleavage at 214 K, accompanied by the loss of hydroxyl on the surface.[10] This agrees with IR studies by Tripp et.al and Panayotov et.al. on the Degussa sample, which showed that DMMP interaction between P=O and surface hydroxyl prompts the creation of methanol. An increase in temperature removes these surface hydroxyls and prompts the formation of covalently bonded and dissociated DMMP on the surface. Both works observe poisoning surface by methyl phosphate like product and saw no changes in the P-CH_3 bond up to temperatures above 750 K.[49,163]

Further FTIR studies by Panayotov on the decomposition of DMMP on Degussa powder showed clear Ti-OCH_3 production on the surface via nucleophilic attack of surface oxygen. Several PO_x species are observed, responsible for surface poisoning from 200-400K. At higher temperatures, lattice oxygen activation was observed to create more Ti-OCH_3 species. These studies indicate that lattice oxygen is key to the chemistry of DMMP on TiO_2 and that anatase and rutile may possess different reactivity towards DMMP decomposition.[164] It has been agreed that many metal oxides including powder TiO_2 do not activate the P-CH_3 bond until very high temperature above 800 K.[10,49,54,59,65] Though there are exceptions such as Fe_2O_3 and CeO_2 which found to be able to activate the P-C bond at lower temperatures below 400 K.[54,55]

Zhou et. al. studied DMMP decomposition on rutile TiO_2(110) in UHV condition using XPS and TPD. Their results indicate that the adsorption occurs primarily via the dative bond between the P=O group and Ti_{5c}. Molecular DMMP desorption occurs up to 550K. Zhou saw little to no evidence of P-O bond cleavage, and further suggest that initial P-C bond cleavage is facile instead. The creation of methoxy initiated by hydroxyl is also not observed. Primary decomposition results consist of methane and hydrogen, with phosphorus species staying on the surface even with heating up to 1000K.[165]

Past ab initio studies on the interaction between DMMP and titania are mostly cluster calculations. Bermudez et. al.[166] and Yang et. al.,[167,168] performed cluster calculations on DMMP interaction with dry and hydrated r-TiO_2(110) clusters. On dry surfaces, adsorption was found to be very weak in the range of -0.74 to -1.06 eV. Most stable adsorption occurs via P=O moiety with surface Ti_{5c}. They collectively agree that adsorption of DMMP on the hydroxylated surface is less stable than those on a dry surface. The adsorption conformation proposed by cluster studies agrees with a DFT-based theoretical study by Quintero et. al.[34] (without Hubbard correction). PBE+D2 predicts molecular adsorption energy of -2.2 eV for DMMP and -1.9 eV for sarin on rutile TiO_2(110). Additionally, Quintero found that the most stable dissociative adsorption is via the O-CH_3 bond cleavage, transferring a methyl to the surface oxygen. In all theoretical studies mentioned here, there is a consensus that the O-CH_3 bond is the most probable first decomposition step thermodynamically. A different work on anatase (001) and (100), cluster calculations show that while molecular adsorption is possible on both dry and hydroxylated surface, dissociative adsorption can only occur on surface with hydroxyls.[169] However, these studies did not perform full decomposition pathway and did not gave insights towards kinetics in each decomposition step, rather, the studies dwell on possible adsorption modes only.

2. Methods and Theoretical backgrounds: Density Functional Theory (DFT)

This chapter provides a brief review of key methods and theorems used within the Density Functional Theory.

2.1. From the Schroedinger equation to DFT

Schrodinger equation and Born-Oppenheimer approximation

Every property of every material (atom) imaginable in the world can be defined by the so-called wavefunction, which depends on the coordinates of electrons in three directions and one spin $\Psi(\mathrm{r}_x, r_y, r_z, s)$. The wavefunction contains all the information about a system, and due to wavefunction being an eigenfunction, the way to extract such information/parameter is via applying the correct operator. Schrödinger equation applies the energy operator, namely a Hamiltonian (H) to the wavefunction to extract the total energy of the system. The non-relativistic Schrödinger equation comes in the form of eq (2-1).

$$H\Psi = E\Psi \tag{2-1}$$

Prior to building the Hamiltonian, it is worth noting that one can simplify the Hamiltonian by using the so-called **Born-Oppenheimer** approximation. In comparison to a nucleus, the electron mass is 1800 times smaller. This mass difference makes the movement of nuclei much slower than that of electrons. Hence, by assuming that the nuclei are static in space, we can simplify the Hamiltonian to be an energy operator that contains only the energy terms associated with the electrons and their interactions. The Hamiltonian therefore can be written into the terms below (eq. 2-3):

$$H = -\frac{1}{2m_e}\sum_{i=1}^{n}\nabla_i^2 + \sum_{i=1}^{n}\frac{e^2}{|r_i - r_j|} + \sum_{i,j}^{n,N}\frac{Z_i e^2}{|r_i - R_j|} \tag{2-2}$$

$$H = T_e + V_{ee} + V_{eN} \tag{2-3}$$

The terms starting on the left, in order are, the electron's kinetic energy contribution, potential energy coming from the interaction between electrons, potential energy from the interaction between nuclei and electrons, and lastly the external potential energy coming from the interaction between nuclei the system. One term, which is the electron-electron interaction is a problematic term to calculate since it depends on the coordinates of two electrons.

One way to simplify this issue is to use the **Mean Field Theorem**, or commonly known as the **Hartree product** rule, where the wavefunction can be approximated as a product of non-interacting individual wavefunction (eq. 2-4). The idea is that, instead of each electron correlating with each and all electrons at the same time, one can model the many-electron wavefunction in terms of one electron 'sensing' the average collective potential from the other electrons in the system.

The electronic density of the system is an observable that can be derived from the wavefunction itself, which equal to the probability of the electrons occupying that space wavefunction (eq. 2-6, multiplied by 2 to account for spin).

$$n(r) = 2\sum_i \Psi_i^*(r)\Psi_i(r) \tag{2-6}$$

Calculating the electron density reduces the initial 4N dimensions of the wavefunction to only 3 variables. Thus, the effort to solve the many-body Schrödinger equation was pushed towards using the density variable instead, marking the start of DFT.

DFT: Hohenberg and Kohn I and II

DFT is built upon two theorems by Hohenberg and Kohn. The first one states that *the ground state energy of the system is a unique functional of the electron density*.

$$E_{ground\ state} = E[n(r)] \tag{2-7}$$

The second Hohenberg and Kohn theory states that the electron density that minimizes the ground state energy is the correct electron density.

$$E[n_{trial}] \geq E_{ground\ state} \tag{2-8}$$

The two Hohenberg and Kohn theorem combined is significant as it implies that the density is the only required variable to explain the ground state energy, which may override the Hamiltonian. However, one problem exists. Despite the rigorous prove, Hohenberg and Kohn specify that the true energy functional is unknown.

In 1965 Kohn & Sham devised an approach to help approximate the optimal density by using the one-electron wavefunction approximation as a basis to build the energy functional. Kohn and Sham suggest building the energy functional by using a 'fictitious' system built from non-interacting electrons (2-10). This fictitious system would have the same ground-state density as the real system of interacting electrons and subsequently. The energy functional can be written in terms of

$$E[n] = T_e[n] + V_H[n] + V_{ext}[n] + E_{XC}[n] \tag{2-9}$$

$$\left[-\frac{\hbar^2}{2m}\nabla^2 + V_H + V_{ext} + E_{XC}\right]\psi_j(r) = E'\psi_j(r) \tag{2-10}$$

$$V_H[n] = e^2\int \frac{|n(r')|^2}{|r-r'|}d^3r' \tag{2-11}$$

The terms on the right-hand side of equation 2-9 are, in order, the kinetic energy of non-interacting electrons (T_e), the interaction between electrons (V_H), the electron-nuclei interaction terms within the system (V_{ext}), and lastly, the exchange and correlation terms which include the correction on the interaction effect between electrons and nuclei that has not yet been accounted for on previous terms. Solving the KS equation requires the self-consistency method, which is described below:

I. Define an initial test electron density $n'(r)$.

II. Using $n'(r)$, solve the Kohn-Sham equation to find the single electron wavefunction $\psi_i(r)$.

III. Recalculate the electron density using the wavefunction found after solving the KS equation:

$$n_{KS}(r) = 2\sum_i \psi_i^*(r)\psi_i(r) \tag{2-12}$$

IV. Compare the calculated KS density $n_{KS}(r)$ with the initial electron density test $n'(r)$. If the two densities are close within an acceptable threshold, then we found the ground-state electron density and can further use this to compute the total energy. However, if the two densities are not the same, then the steps must be performed again until self-consistency is reached.

2.2. Hubbard U Correction

For materials with many-electron states of highly localized electrons, such as transition metal oxides with partially filled d or f shells, DFT often presents errors, resulting from the unphysical self-interaction between electrons, arising from the approximate exchange-correlation functional. This causes artificial electron delocalization which is unphysical and incorrect. For transition-metal oxides, DFT may give the $d^{n-1}s^1$ instead of the $d^{n-2}s^2$ configuration, leading to incorrect cohesive energies.[170]

DFT+U is a method that attempts to correct this self-interaction error by introducing the U and J parameters, in which the two parameters describe the self-interaction to some extent. There are two ways to implement DFT+U, the first one is using the Liechtenstein method in which U and J are parameterized separately, the second one is the Dudarev (Anisimov et.al) method in which the U and J parameters are condensed as the effective Hubbard $U_{eff} = U - J$ parameter.

$$E_{DFT+U}[\rho(r)] = E_{DFT}[\rho(r)] + \frac{\bar{U} - \bar{J}}{2}\sum_\sigma (n_{m,\sigma} - n_{m,\sigma}^2) \tag{2-16}$$

Where $n_{m,\sigma}$ is the occupation matrix in the mth d state, $\bar{U}$ and $\bar{J}$ are the spherically averaged matrix element of the electron-electron interactions. In this thesis, we will use the Dudarev approach to describe the self-interaction between electrons of metal oxide. This concludes the review of the basic theory behind DFT.

2.3. Appendices

This chapter is heavily based on sources below:

[170] Sholl, D. S.; Steckel, J. A. *Density Functional Theory: A Practical Introduction*; 2009. https://doi.org/10.1002/9780470447710.

[171] Koch, W.; Holthausen, M. C. *A Chemist's Guide to Density Functional Theory*; 2001. https://doi.org/10.1002/3527600043.

[172] Cramer, C. J. *Essentials of Computational Chemistry Theories and Models*; 2004. https://doi.org/10.1021/ci010445m.

[173] Marthinsen, A. *Https://Youtu.Be/SXvhDLCycxc*; 2016.

3. Results

3.1. Part 1: Thermodynamic analysis of dimethyl methylphosphonate DMMP on $Fe_3O_4(111)/Fe_2O_3(0001)$

This work studies the interaction of DMMP with $Fe_3O_4(111)$ films grown on $Fe_2O_3(0001)$ in a controlled environment using both computational and experimental methods such as density functional theory (DFT), temperature-programmed desorption (TPD), scanning tunneling microscopy (STM) and X-ray photoelectron spectroscopy (XPS). This result section is adapted from a publication in which the author participated by Walenta et. al.[25] The author performed all the theory part of this publication. For full acknowledgment and copyrights see section 3.1.7.

3.1.1. Computational method

All Spin-polarized DFT calculations were performed using the Vienna ab initio simulation package (VASP)[174]. The projector augmented wave (PAW) method was employed to describe the electron-ion interactions. The Perdew-Burke-Ernzenhof (PBE) exchange-correlation functional, within the generalized gradient approximation (GGA), was used.[175] To account for the van der Waals interactions, the dDsC dispersion correction was added to the total energy.[176,177] The threshold for electronic energy was set to 10^{-6} eV with an atomic force criterion of 0.03 eV/Å for geometry optimizations. The cutoff for the plane-wave basis set was 500 eV for bulk and 400 eV for surface calculations. Due to Fe_3O_4 having partially filled orbitals, the Hubbard U correction is essential to take care of the on-site Coulomb interaction within d orbitals. Dudarev implementation was used with effective U value of 3.61 eV (U = 4.50 eV and J = 0.89 eV).[178] This U effective value yields an optimized surface with the magnetization of -4.02 and 4.07 μ_B for tetrahedral and octahedral Fe cation respectively, in good agreement with the experimental value of 4.05 μ_B.[179,180]

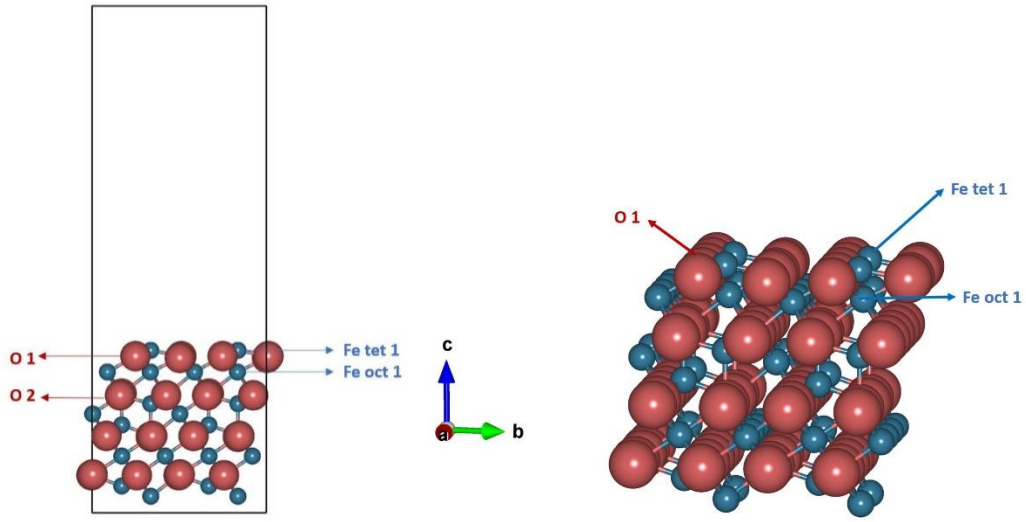

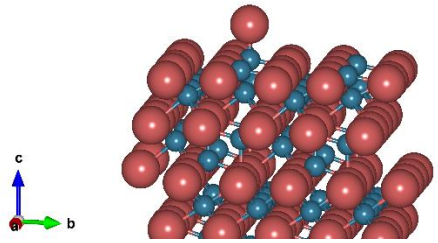

Figure 12 (Top) Side and perspective views of Fe_3O_4 slab model. (Bottom) Surface with ¼ ML O coverage. Blue represents Fe atoms and red represents Oxygen atoms. Each supercell contains 4 surface-tetrahedral Fe.

The unit cell of Fe_3O_4 bulk contains 24 Fe and 32 O atoms. Integration over the Brillouin zone for bulk optimization uses a 5x5x5 Monkhorst Pack k-point mesh. The optimized lattice parameter was found to be 8.43 Å. The surface was then built by cutting the optimized bulk in the (111) direction. The surface is a p(2x2) supercell containing 48 Fe and 64 O atoms (fig. 12). This supercell contains 4 active sites (4 exposed unsaturated Fe cations). Calculations of surfaces use a k-point mesh limited to the Γ-point. A test with higher k-points yields a negligible difference in adsorption energy. The lattice parameter is $\frac{a_0}{\sqrt{2}} = 11.92$ Å (experimental work, $\frac{a_0}{\sqrt{2}} = 11.84$ Å) with a vacuum of 20 Å to avoid inter-layer interaction.[181] Out of the 12 atomic layers, the first 5 layers are frozen to mimic the bulk. One oxygen adatom is added on one of 4 tetrahedral Fe cations which correspond to oxygen coverage of 1/4ML. Harris correction within the Makov-Payne method is used to correct the dipole-dipole interaction between slabs in the z-direction.[182]

3.1.2. Experimental Method

The reactivity measurements were carried out in an ultrahigh vacuum (UHV) apparatus with a base pressure of $< 8\times10^{-11}$ Torr, which has been described in detail before.[183,184] The $Fe_3O_4(111)$ thin film was formed as a result of reductive sample preparation of α-$Fe_2O_3(0001)$ single crystal and has been fully characterized previously.[184–187] The α-$Fe_2O_3(0001)$ single crystal (SurfaceNet GmbH) is mounted and its temperature can be controlled between 130 K and 1000 K.[184] Crystal cleaning is accomplished by Ar^+-ion sputtering (1.0 keV, 1.0×10^{-5} Torr, 15 min, 13 μA sample current) and annealing in vacuo (1000 K, 15 min). Before every experiment, 3 cycles of sputtering and annealing are performed to remove all potential contaminants. For the sake of succinctness, this surface sample is labeled interchangeably between $Fe_3O_4(111)$ or $Fe_3O_4(111)/Fe_2O_3(0001)$ surfaces throughout the thesis. Experiments have been performed by Constantin Walenta in Harvard.

3.1.3. Experimental Results: Temperature Programmed Desorption and Scanning Tunneling Microscopy

Temperature Programmed Desorption: UHV

Figure 13 shows the temperature-programmed desorption (TPD) spectra for DMMP thermal decomposition on $Fe_3O_4(111)$. The most notable decomposition channels happen in three waves. The first decomposition pathway produces dimethyl ether (DME) at around 650 K, following, the second decomposition pathway involves the production of methanol and formaldehyde at 700 K and finally the production of formaldehyde, CO, and CO_2 at around 850 K. The formation of methanol and formaldehyde at 700 K was expected as previous work on methanol on Fe_3O_4 yields similar products.[185] This indicates that the surface-active species would involve methoxy which could only come from DMMP. The final decomposition channel consisting of formaldehyde, CO, and CO_2 correlates to the final combustion product of the remaining carbon species on the surface. The additional sustained yet the low peak of methanol spreading from 350 to 650 K correlates to the interaction of P-OCH_3 with surface defect hydroxyl, prompting the formation of methanol and P-O bond cleavage.

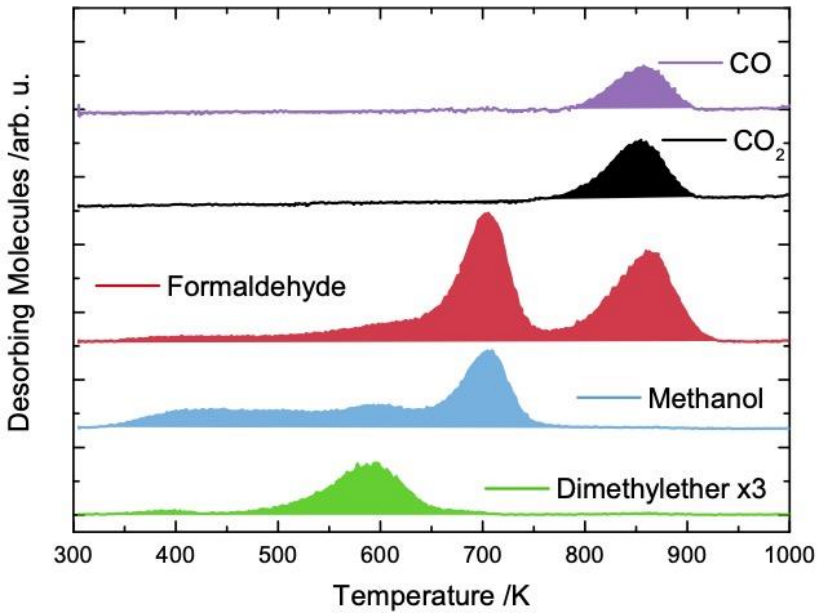

Figure 13 Temperature Programmed Desorption Spectra of DMMP thermal decomposition on $Fe_3O_4(111)/Fe_2O_3(0001)$ films. Data obtained after exposure of DMMP to full saturation at 1.0×10^{-9} torr for 1 minute. There are 3 main decomposition channels at 600, 700, and 850 K.

The interesting result comes from the first decomposition channel, with the production of DME at around 575K. The DME production has been found on other metal oxides before,[188] but its pathway has yet to be determined. To see if whether DME comes from the reactions between surface methoxy species, a test with isotopic labeling by adsorption of both DMMP and CD_3OH was performed. The test showed both formations of active surface CD_3O and CH_3O species, leading to the production of methanol and formaldehyde around 700K. This result indicates that DME production proceeds exclusively from the self-rearrangement of the remaining DMMP or surface-bound MMP.

Scanning Tunneling Microscopy

Figure 14 showed the scanning tunneling microscopy image of the $Fe_3O_4(111)/Fe_2O_3(0001)$ samples prior to and after the thermal decomposition reaction process. The bright feature corresponds to the exposed surface oxygen, with Fe cations hidden in the dark rows, as expected from the used tunneling bias. The image of the as-prepared $Fe_3O_4(111)$ surface suggested O_{ad} termination on top of free Fe cation, corresponding to a 0.67 ML coverage.

After initial adsorption of DMMP, the image does not have a good resolution as there are active diffusion processes of possible active surface species. The STM image obtained after heating the sample to 750 K showed the formation of islands corresponding to PO_x species. X-ray photoelectron spectra suggest that this remaining exhibit PO_3 formula (binding energy of phosphorus peak of 133.1 eV and 134 eV).

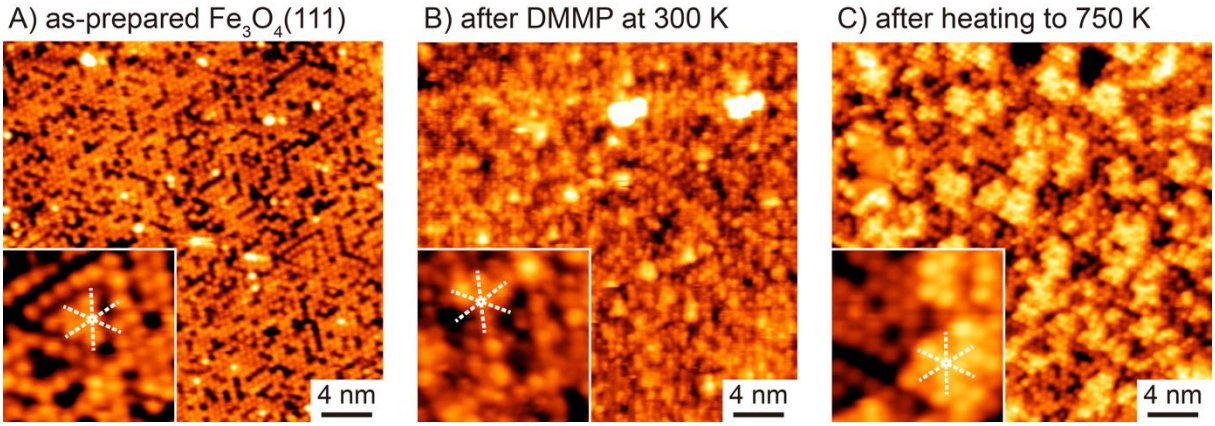

Figure 14 Scanning Tunneling Microscopy images of (A) the pristine $Fe_3O_4(111)$ thin-film containing both O adatoms and tetrahedral coordinated lattice Fe; (B) surface after exposure to DMMP (7.5×10^{-9} Torr for 60 s) at 300 K; and (C) formation of P-containing islands heating to 750 K. The images were obtained at room temperature with a tunneling current of 0.02 nA and a bias of −2.2 V

Temperature Programmed Desorption: Probing the hydrolysis effect.

To see if there is significant hydrolysis as a potential fourth reaction channel, two additional TPD test was performed: (A) fully saturated surface with DMMP was exposed to water at 300 K and (B) clean surface was first exposed to water prior to addition of DMMP (fig 15). In both cases, no substantial effect was observed during the TPD reaction. However, on case B where the water is adsorbed prior, two clear desorption peaks assigned to water are observed at 400 and 600 K. Consistent with previous studies on the $Fe_3O_4(001)$ surface,[189] these bound hydroxyl may be due to surface defects and thus poses no substantial effect to final product composition. Finally, a huge peak at 870K is assigned to water resulting from the combustion of the remaining phosphor-containing compound on the surface. This peak is observed in all cases of TPD, including those without water, and thus is independent of the addition of water earlier. This result is the opposite of that for the DMMP decomposition pathway on other metal oxides[190–192] and surfaces such as

metal-organic framework[67,191], supporting the hypothesis that DMMP decomposition is very much surface sensitive.

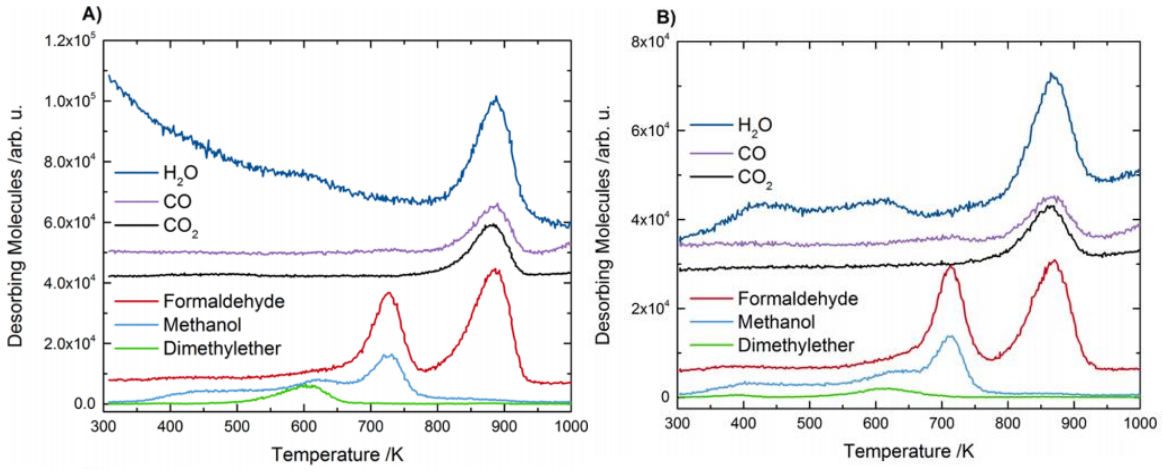

Figure 15 TPD spectra of the fully saturated sample with DMMP which is then dosed with water prior to reaction (A). TPD spectra of the surface first dosed with water prior to adsorption of DMMP and thermal reaction (B).

3.1.4. Computational Results: DMMP adsorption modes and decomposition channel

Molecular Adsorption

DFT calculations showed that the adsorption of DMMP on Fe_3O_4(111) is very stable. Figure 16 showcases the two most stable molecular adsorption modes of DMMP upon exhaustive screening. The adsorption energies are calculated using equation 3-1:

$$E_{adsorption} = E_{surf+DMMP} - E_{surf\frac{1}{4}ML\ O} - E_{DMMP} \qquad (3\text{-}1)$$

The most stable adsorption geometries involve binding of DMMP via the P=O group with surface tetrahedral Fe cation (P=O-Fe) with additional van der Waals interaction between one of DMMP's methoxy group (O-CH_3) with surface oxygen adatom ($H_{methoxy}$---O_{adatom} = 2.44 Å). This configuration ((2) in Table 4) yields adsorption energy of -2.57 eV (-248 kJ/mol). The bond distance between the oxygen of the P=O group and Fe cation is 1.54 Å. This adsorption mode is very much expected, as we have seen in the case of ceria, molybdenum, and cupric oxide.[50,60]

The second most stable adsorption modes correspond to the oxygen of DMMP's methoxy group interacting with surface tetrahedral Fe cation (CH_3O-Ti). There is an additional stabilizing interaction between methyl and oxygen adatom via van der Waals interaction (H_{methyl}---O_{adatom} = 3.33 Å). This configuration ((1) in Table 4) yields adsorption energy that is also quite stable, at -2.06 eV (-198. kJ/mol). This is an adsorption mode that has not been yet seen before in the

literature on iron oxide and shows that DMMP can easily adsorb on the surface not only via one channel of adsorption.

Table 4 Stable molecular adsorption modes and adsorption energies of DMMP on Fe_3O_4(111).

Index	Molecular adsorption modes		Adsorption Energy [eV]	Adsorption Energy [kJ/mol]
	DMMP	Surface		
1	O of methoxy	Fe tet	-2.06	-199
2	O of P=O	Fe tet	-2.57	-248

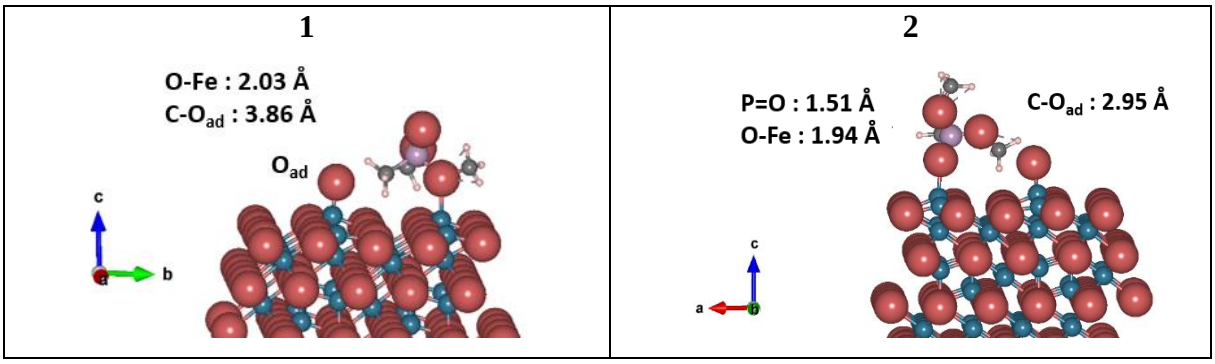

Figure 16 Molecular adsorption geometries of DMMP on Fe_3O_4(111) and important distances. (1) DMMP adsorbing via OCH_3 group with surface Fe (Fe-OCH_3). (2) DMMP adsorbing via P=O-Fe.

Dissociative Adsorption

The next step is to study if the decomposition of DMMP on the surface is thermodynamically favorable. Here we consider the dissociative adsorption of DMMP via the cleavage of the P-OCH_3 bond. Figure 16 showcases the three most stable adsorption modes after exhaustive searches.

The first step is to look at methoxy adsorption on clean Fe_3O_4(111) surface. We found that the dissociated methoxy adsorbs most stable on the surface Lewis acid site, which is the tetrahedral Fe cation. The adsorption energy of dissociated methanol is -2.82 eV, agreeing well with the literature.[193] The next step is the screening of the remaining methyl methyl phosphonate (MMP) adsorption. We found that MMP adsorbs most stable via the interaction between phosphor and surface O adatom (fig. 17, image 5). Along with methoxy on the surface, this makes dissociative DMMP adsorption via P-O bond cleavage thermodynamically downhill by 1.19 eV (or adsorption energy of -3.76 eV with respect to the gas phase). This geometry is probably stable due to MMP now being able to re-establish a P oxygen interaction on the surface. Additionally, there is a stabilizing van der Waals interaction between the free P=O group and nearby surface-bound methoxy. The distance between the phosphor and the oxygen adatom is 1.56 Å (P-O bonding distance).

All other explored dissociative geometry (Table 5) leads to an overall endothermic net reaction. Our result indicates that the oxygen adatom is crucial to initiate dissociative adsorption by helping stabilize the center phosphor of DMMP after the P-OCH_3 bond cleavage.

Table 5 The three energies of dissociative adsorption conformations along with their adsorption energy relative to gas-phase DMMP

Index	Dissociative adsorption modes		Adsorption Energy [eV]	Adsorption Energy [kJ/mol]
	MMP	Surface		
3	CH_3O	Fe_{tet}	-0.23	-22
4	P=O	Fe_{tet}	-0.83	-80
5	P	O-Fe_{tet}	-3.76	-362

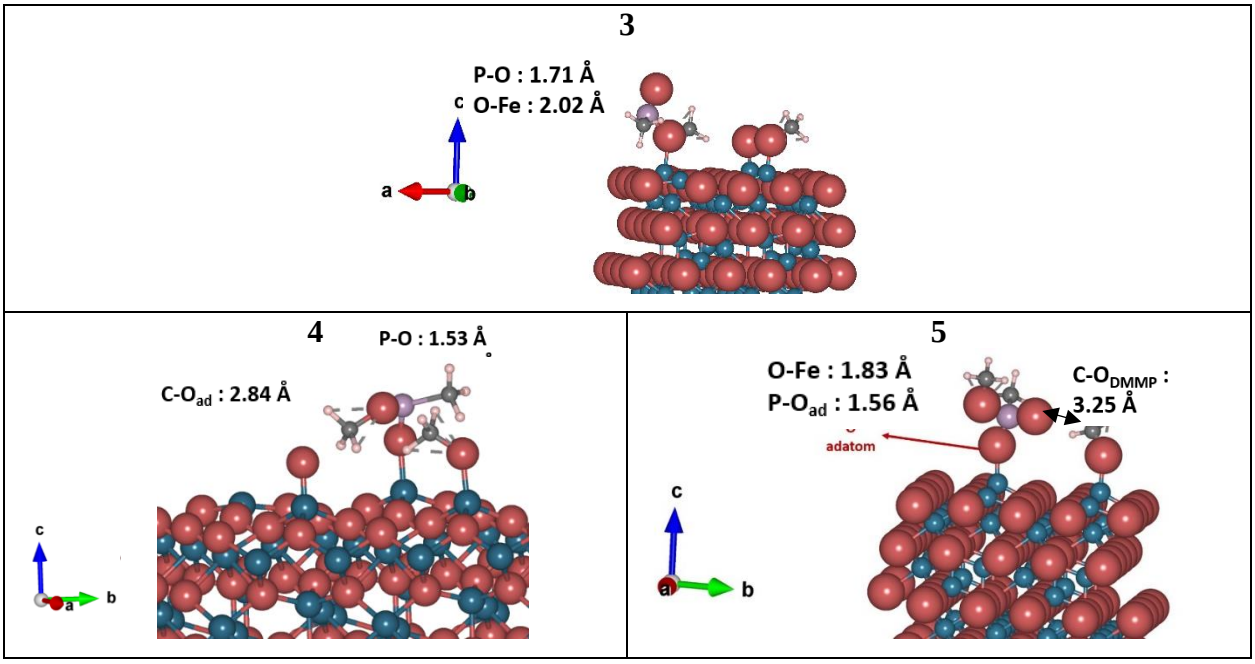

Figure 17 Different MMP and methoxy configurations on the Fe_3O_4(111) surface with an oxygen adatom. The respective energies are displayed in Table 5.

3.1.5. Discussion: Thermodynamic analysis

We look back at the result of TPD which yields the two most interesting reaction channels. The first channel is slightly unusual: the production of DME at 650 K. As the isotopic labeling studies with DMMP and CD_3O species have shown, none of the resulting DME contains deuterium. This indicates that DMMP may initiate self-rearrangement after initial P-OCH_3 bond cleavage to produce DME. Although being a minor pathway, this serves as a way to yield the final PO_x surface structure on the surface.

Unfortunately, DFT calculations show that direct self-rearrangement of DMMP to produce DME is thermodynamically unfavorable! Figure 18 showed that direct DME production into the gas

phase is uphill by 1.38 eV. We hypothesize that this geometry is highly unstable due to phosphor being under coordinated with only 2 oxygen adatoms on the surface.

However, this intermediate can be further stabilized by additional O adatom to establish the tetrahedral coordination of the phosphor center. A possibility of this pathway being true is further evidenced by the previous STM work on the oxidation of methanol where the reaction depends on the oxygen mobility through the film, to drive the reaction towards the product.[185] We then further test the thermodynamic stabilization effect of oxygen adatom production coming from the balance between magnetite and hematite (figure 19).

$$\mathbf{3}\ \boldsymbol{Fe_2O_{3_{bulk}}} \rightarrow \mathbf{2}\ \boldsymbol{Fe_3O_{4_{bulk}}} + \boldsymbol{O} \qquad (3\text{-}2)$$

Indeed, the addition of oxygen near phosphor coming from the balance between magnetite and hematite gives the system up to -1.65 eV stabilization effect. This phenomenon showcases the unique ability of Fe_3O_4 to activate P-CH_3 bond cleavage via self-rearrangement by utilizing extra oxygen from subsurface hematite to drive the reaction downhill.

The phenomenon of Fe_2O_3 being able to activate the P-CH_3 bond has already been mentioned in the literature. Experimental TPD and AES works by White et. al. show the ability of Fe_2O_3 to activate the P-CH_3 bond at a temperature as low as 247 K, due to the availability of surface oxygen to stabilize the decomposition intermediates. White observed that this is opposite to the case of SiO_2.[57] It is probable, that this extra oxygen coming from Fe_2O_3(0001) was the drive for P-CH_3 bond activation, but the lack of available Lewis basic site to receive -CH_3 prompts DMMP to self-rearrange and produce DME instead.

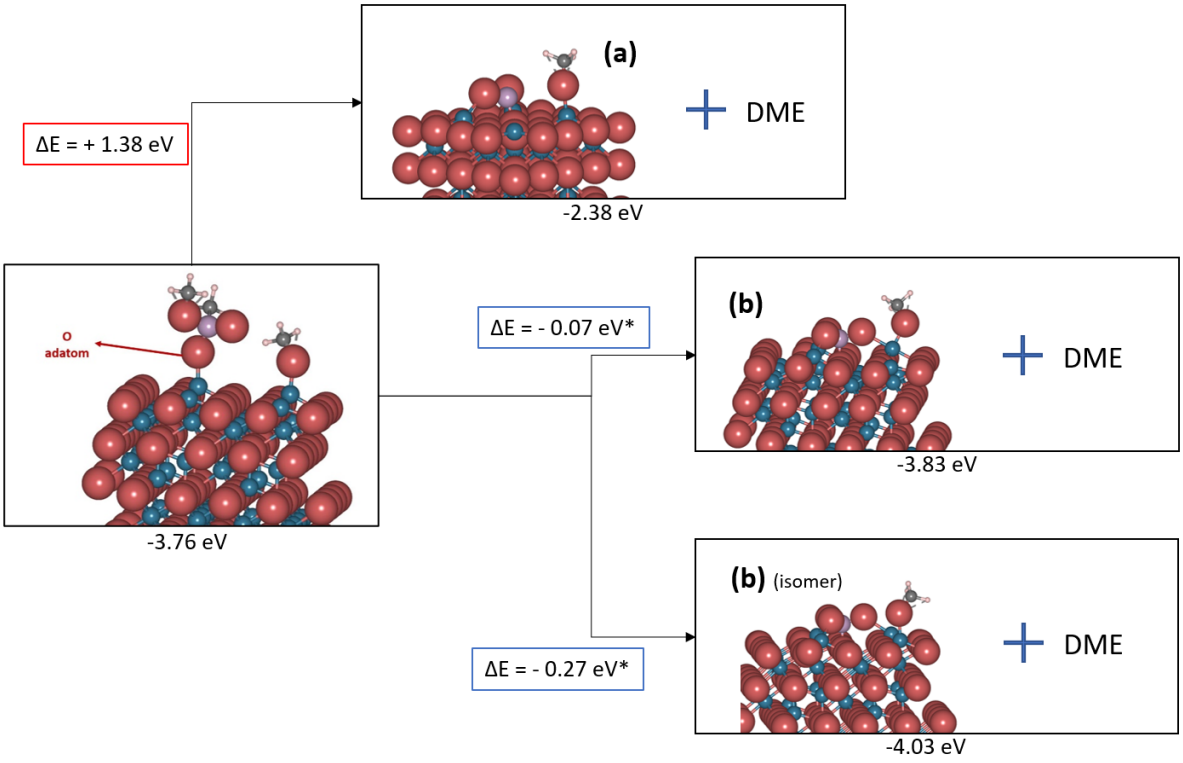

Figure 18 Possible DME formation pathway from dissociative adsorbed DMMP. Direct self-rearrangement of MMP to produce DME is thermodynamically not possible (path a). Intermediates upon DME production may be stabilized by additional oxygen adatom (path b).

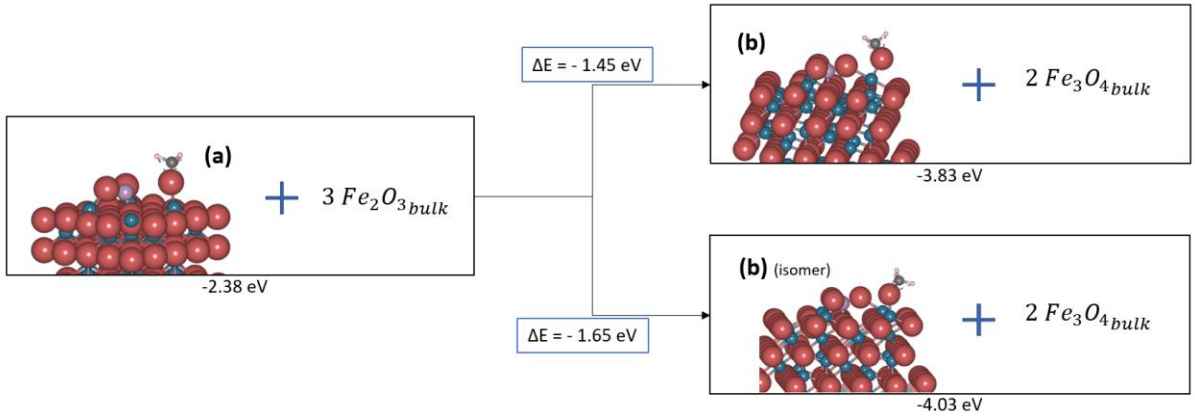

Figure 19 Thermodynamic analysis of additional O-adatom obtained from the reduction of hematite to produce Intermediate b on phosphor-containing intermediate upon release of DME.

The second reaction channel, with the production of methanol and formaldehyde at 720 K indicates that the major decomposition products stem from P-OCH_3 bond cleavage, transferring a methoxy species on the surface Fe cation and an MMP on surface Lewis base site. Additional evidence by

DFT suggests that this step is highly favorable with the help of surface oxygen adatom replenishing the tetrahedral configuration of the phosphor center of MMP.

Lastly, it is worth mentioning that in the final reaction channel at 870 K where the remaining intermediates combust to produce CO, CO_2, CH_2O, and H_2O, there are no phosphorus-containing compounds in the final gas stream products. This indicates that phosphor is accumulating on the surface, poisoning it for further reactivity. This can be seen in the STM images in figure 13. This ability to trap final phosphorus intermediates at room temperature makes Fe_3O_4 an interesting surface in comparison to other metal oxides such as $TiO_2(110)$ or MoO_3 where molecular desorption of DMMP at room temperature was observed.[70] Additionally, unlike metal framework, DMMP decomposition is not affected by exposure to water. In a sense, the surface does not need to be hydroxylated in order to help promote the adsorption and decomposition of DMMP.

3.1.6. Conclusion

Thermal decomposition of DMMP, a simulant for the nerve agent sarin on $Fe_3O_4(111)/Fe_2O_3(0001)$ film was studied by TPD, STM, and DFT. The synergistic result of TPD and DFT shows that DMMP adsorption is very stable, both molecular and dissociative-wise. Two channels of decomposition were proposed, firstly via the P-OCH_3 bond cleavage, initiating methoxy disproportion reaction to produce methanol and formaldehyde. The second channel of decomposition arises from the self-rearrangement of MMP to produce DME, however, this step requires the migration of O atoms from bulk $Fe_2O_3(0001)$ to the surface to stabilize remaining phosphor-containing intermediates. Finally, upon heating to 1000 K, the remaining phosphor intermediate accumulates on the surface as islands, as seen from STM images and DFT calculations. Co-adsorption of water shows no tangible impact on the decomposition process, indicating that the chemistry of DMMP on $Fe_3O_4(111)$ does not depend on hydroxyls defect. This result suggests Fe_3O_4 as a good candidate material for the filtration of nerve agents and pollutants.

3.1.7. Acknowledgments

Special thanks to Dr. Constantin Walenta for the TPD spectra measurements, Dr. Fang Xu for the STM images, Dr. Cynthia Friend and Dr. Philippe Sautet for helpful guidance and discussions, Dr. Wei for the help with the initial computational set-up. The author would also like to acknowledge the grant given by the U.S. Groupy Research Office, under grant no. W911NF1820143 and by the Defense Threat Reduction Agency under Program no. CB3934.

Reprinted (adapted) with permission from

Walenta, C. A.; Xu, F.; Tesvara, C.; O'Connor, C. R.; Sautet, P.; Friend, C. M. Facile Decomposition of Organophosphonates by Dual Lewis Sites on a $Fe_3O_4(111)$ Film. *J. Phys. Chem. C* **2020**. https://doi.org/10.1021/acs.jpcc.0c01708. Copyright 2020 American Chemical Society.

3.2. Part 2: Elucidating decomposition pathway of DMMP and Sarin on pristine and defective r-TiO_2(110)

In this section, we employed DFT to screen various adsorption modes and multiple decomposition pathway scenarios of DMMP on the perfect and defective surface of rutile TiO_2(110). To further validate our result, experimental temperature-programmed desorption (TPD) was also included. This result section is adopted from a submitted manuscript by the author.

3.2.1. Computational method

Density Functional Theory calculations were performed using the Vienna Ab Initio Simulation Package (VASP).[174,194] The calculations employed a generalized gradient approximation (GGA) functional namely the Perdew-Burke-Ernzerhof (PBE) to describe the exchange and correlation energies. Van der Waals correction was accounted for using dDsC dispersion correction within VASP software.[175,176,195] The Projector Augmented Wave (PAW) method was used to describe the electron-ion interactions with a kinetic energy cutoff of 500 eV.[174,196,197] Due to the onsite Coulomb repulsion of the Ti 3d orbitals, the calculations were treated with Hubbard U correction (DFT+U). Dudarev approach was employed with effective U parameter of 4.2 eV on Ti.[178,198] Justification for U value of 4.2 eV was taken because it has shown to adequately depict correct localization of electrons on surfaces in the presence of oxygen vacancies.[147] The electronic convergence criterion was set to 10^{-6} eV, with the maximum atomic force threshold set to 0.03 eV/atom.

Pathway exploration and transition state searches were performed using the Nudged Elastic Band (NEB) method with 8 images created between intermediates. Due to the high degree of freedom of DMMP and Sarin, NEB calculation is stopped once the system reaches a force of 0.1 eV on each image to reduce computational cost. The search of the transition state is further continued with the Quasi-Newton until the system converges with forces under 0.03 eV/atom.

The adsorption energies are calculated with equation 3-3:

$$E_{ads} = E_{surf+DMMP} - E_{surface} - E_{DMMP(g)} \qquad (3\text{-}3)$$

The kinetic rate constant was calculated using the Transition State Theory approximation, with the vibrational contribution of the system neglected:

$$k = \left(\frac{k_b T}{h}\right) * \exp\left[\frac{-(E_{TS} - E_R) * k_b}{R * T}\right] \qquad (3\text{-}4)$$

Where E_{TS} is the relative energy of the transition state and E_R is the energy of the reactant.

To create the periodic slab of rutile TiO_2 (110), bulk TiO_2 was optimized using PBE+U functional with van der Waals correction using the dDsC method.[177] To see the effect of Hubbard U correction towards the lattice constant, rutile TiO_2 bulk was optimized with both PBE and PBE+U methods. The calculated lattice constants of the bulk TiO_2 using PBE+dDsC yield values of a = 4.65 Å and c = 2.94 Å, whereas using PBE+U+dDsC yield lattice constants of a = 4.68 Å and c = 3.03 Å. The

calculated lattice constant agrees with previous studies of TiO_2 using PBE functional. It is known that PBE functional slightly overestimates the lattice constant in comparison to the experimental measurement (a = 4.54 Å and c = 2.94 Å).[124,155,199] All bulk calculations used the gamma centered k-mesh of 4x4x4.

To create the pristine TiO_2(110) surface, a 4x2 supercell with lattice vectors a = 13.16 Å and b = 12.07 Å was cut from the bulk (fig. 20). The surface cell contains four O-Ti-O trilayers (12 atomic layers) with a vacuum distance of 15 Å to avoid interaction between layers. The first O-Ti-O trilayers are frozen to mimic the bulk. The TiO_2(110) surface has two types of oxygen atoms, namely O_{2c} and O_{3c}. Among the two types of oxygen atoms, oxygen vacancy at the bridging oxygen site was found to be more stable[138,140,148], and thus the defect sites considered are the vacancy on the O_{2c} bridging site only. The defective surface was created by removing one O_{2c} from the pristine surface (fig. 20, right). This corresponds to 0.125 ML oxygen vacancy concentration, which is deemed close to the experimental observation ranging between 0.08 to 0.15 ML.[156,200,201] For surface calculations, k-mesh of 1x1x1 gamma centered is found to produce acceptable accuracy. Harris correction within the Makov-Payne method was employed to take care of the dipole-dipole interaction between each slab in the z-direction.[182] Van der Waals interactions have been considered in all calculations using the density-dependent dispersion correction method, dDsC.[176,177]

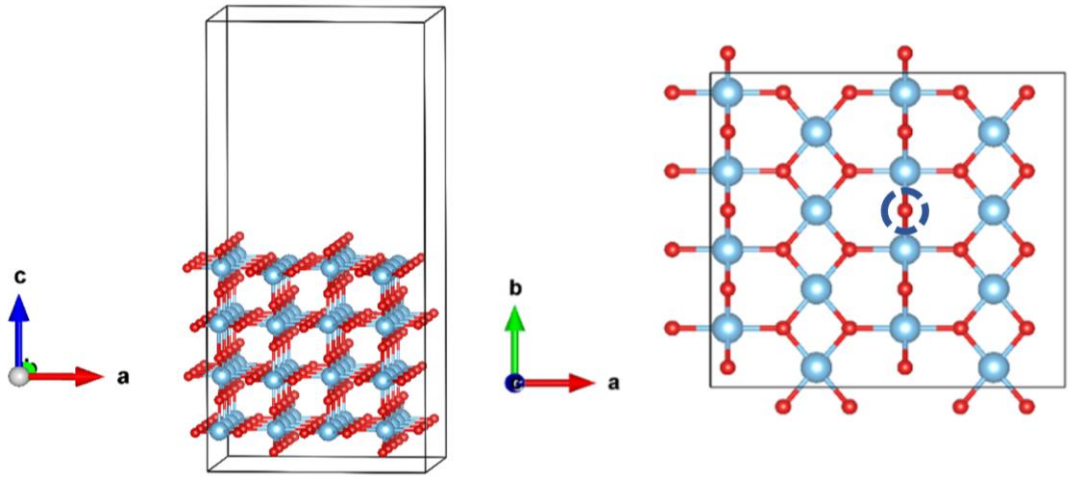

Figure 20 Rutile TiO_2(110) Surface Model. (Left) Top view of pristine TiO_2 (110) and (Right) Top view of defect TiO_2(110) with an O_{2c} oxygen vacancy (indicated by a broken line circle, since a subsurface O atom is seen below at the same x,y position).

3.2.2. Experimental methods

Desorption and reactivity of DMMP are studied in an ultra-high vacuum apparatus described previously.[184,202] A clean TiO_2(110) surface with a bridge-bonding oxygen vacancy concentration of ≤2% of a monolayer was obtained by cycles of Ar^+-sputtering and vacuum annealing 780

K.[202]DMMP (≥97%, Sigma-Aldrich) was purified by pump freeze cycles. Before every experiment, the designated gas line system was flushed and pumped multiple times and further passivated with more than 1 h of DMMP exposure to avoid contamination by hydrolysis products.[25] DMMP exposures were performed with a pressure of 5×10^{-10} Torr for 60 s unless otherwise stated, which lead to a monolayer saturation coverage at a crystal temperature of 200 K. The given exposure parameters do not account for an enhancement factor of the needle doser, that was determined to be 27 previously. Temperature programmed desorption and reaction experiments were performed with the crystal positioned in a line-of-sight geometry with the quadrupole mass spectrometer and a constant heating rate of 1 K/s. The monitored masses include 2, 15, 16, 18, 27, 28, 29, 30, 31, 32, 33, 35, 44, 46, 47, 79 and 124. The desorption products were identified by their fragmentation patterns and corrected fragmentation pattern contributions and mass spectrometer sensitivity.

3.2.3. Experimental results: Temperature Programmed Desorption

Figure 21 shows the temperature-programmed desorption spectra results. A broad desorption peak assigned for DMMP from r-TiO_2(110) can still be seen at a wide range of temperatures (200 K to 500 K). The wide broad of desorption agrees well with previous studies.[51] Products such as methanol and formaldehyde only started to show signs at a high temperature of 650 K, albeit minor. No other reaction products are observed. The simultaneous desorption of methanol and formaldehyde is a characteristic indication of the result of the surface disproportionation reaction of surface-active methoxy species.[203,204] Our hypothesis and previous literature on TiO_2(110) suggest that these surface methoxy species could only be present as the result of DMMP decomposition.[51,52,205] After heating through 800 K, it was observed that some of the $PO_xC_yH_z$ residues stay on the surface based on a small P signal a subsequent Auger Electron Spectrum (Fig. 21).

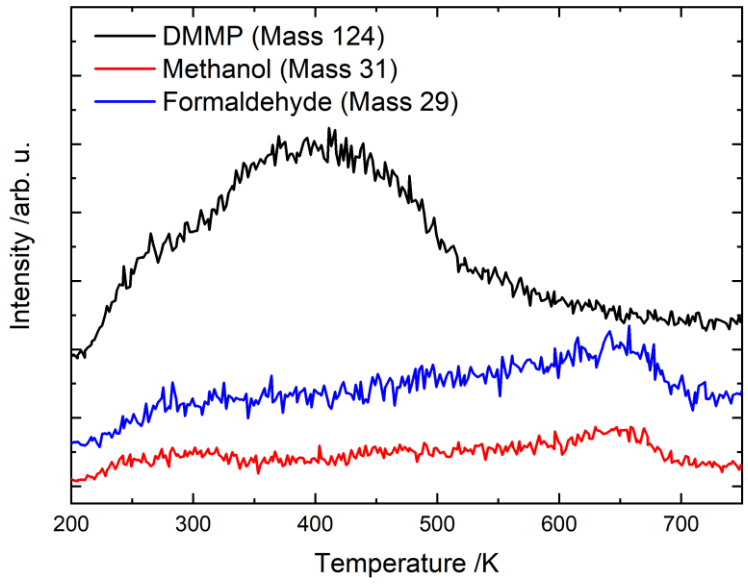

Figure 21 TPD spectra of thermal decomposition of DMMP on reduced TiO_2(110). DMMP desorbs molecularly from the surface between 200 K and 500 K. Simultaneous formation of methanol and formaldehyde fits the temperature of methoxy disproportionation previously observed on TiO_2(110) surface.[203]

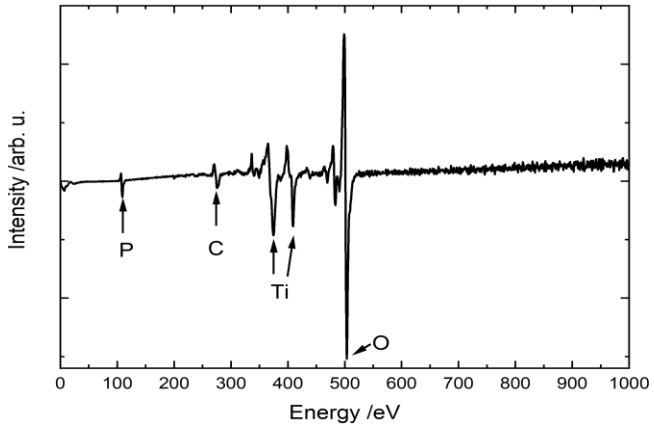

Figure 22 The Auger electron spectrum of the TiO_2(110) single crystal after a temperature-programmed desorption experiment shows that phosphorous and carbon on the surface indicating residual P-containing species on the surface that is assigned to a DMMP reaction. The elements are identified by their characteristic Auger peak energies: P at 110 eV, C at 272 eV, Ti at 387, and 418 eV and O at 503 eV.

The observation of desorbing DMMP is not a surprise, past studies have observed the behavior of DMMP desorbing on reducible oxides such as Ce[50] and particularly on Ti[51,52,205]. This is in opposition to what we have seen in the case of Fe_3O_4(111) supported on hematite shown previously, where DMMP readily reacts on the surface at room temperature due to the availability

of extra oxygen.[25] This observation further adds to our hypothesis that decomposition on TiO_2 requires additional thermal energy and that the reactivity of DMMP decomposition depends on the metal oxide used.

3.2.4. DMMP adsorption and decomposition pathway on pristine r-TiO_2(110)

3.2.4.1. DMMP adsorption modes on the pristine surface

DFT calculations show that DMMP adsorption is stable on pristine TiO_2(110). Adsorption mode screening yields only two stable adsorption modes (figure 23). For the sake of readability, the atoms on DMMP are marked with Latin numbering. The first and most stable adsorption geometry shows DMMP adsorbing via the oxygen of P=O group with surface Lewis acid, Ti^{5+} cation (P=O_I-Ti), with additional interaction between methoxy and neighboring Ti^{5+} (O_{II}-Ti). This geometry has adsorption energy of -2.35 eV (-227 kJ/mol). The distance between the oxygen and surface Ti_{5c} (P=O_I-Ti) is 2.11 Å, while the distance between methoxy and Ti_{5c} (O_{II}-Ti) is 2.42 Å.

The second and only other stable molecular adsorption geometry involves only the bonding between the oxygen of the P=O group and Ti_{5c} without any additional stabilizing interaction. The additional interaction of methoxy and neighboring Ti seems to greatly stabilize the system as this geometry yields significantly less stable adsorption energy of -1.71 eV (-164 kJ/mol).

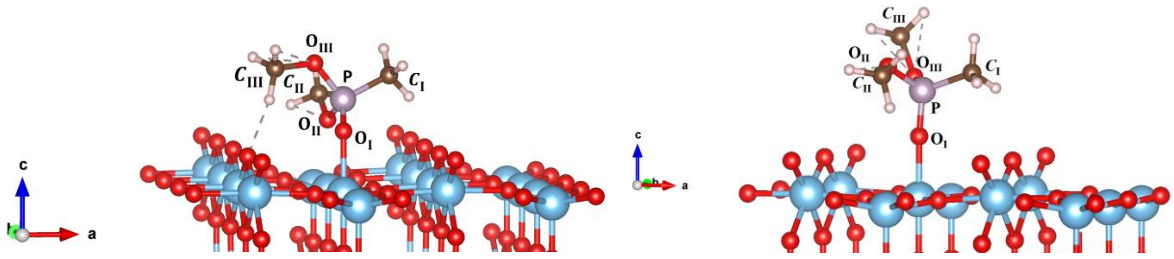

Figure 23 Two most stable molecular adsorption geometries of DMMP in TiO_2(110). Most stable adsorption (left) has adsorption energy of -2.35 eV. The second most stable adsorption geometry (right) has an adsorption energy of -1.71 eV.

Following the most stable molecular adsorption mode, there are 3 possible decomposition pathways initiated via P-OCH_3, O-CH_3, or P-CH_3 bond cleavage, which we will analyze in the following section. Note that we did not investigate the C-H bond cleavage as experimental work shows a small probability of C-H bond cleavage.[165]

3.2.4.2. Decomposition on Pristine surface: P-O_{II} bond cleavage-initiated

Decomposition pathways of DMMP initiated via P-OCH_3 bond cleavage are shown in figure 25. Two P-OCH3 bonds can be cleaved, however, P-O_{II} bond cleavage is rendered to be more accessible as it is already interacting with surface Ti_{5c}. The transition state for this step requires a nucleophilic back attack towards the DMMP phosphor center by surface bridging oxygen, forming

a Penta-coordinated phosphor center (figure 24). Although cleaving the P-O_{II} bond yields an intermediate that is thermodynamically more stable by 0.37 eV from the adsorbed state (figure 25, S2), the barrier to reach this intermediate stood very high at 2.18 eV (210 kJ/mol). Cleavage of the P-O_{II} bond results in a transfer of methoxy species and residual methyl methylphosphonate (MMP) to the surface.

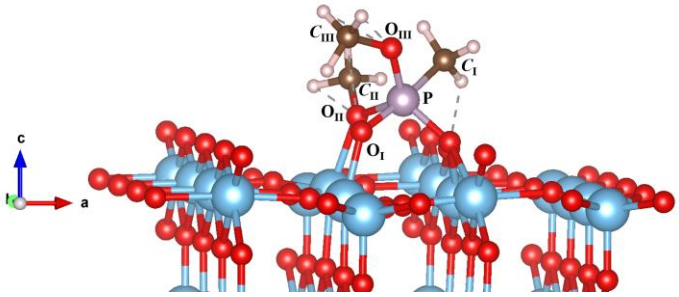

Figure 24 Transition State to 1st P-O bond cleavage of DMMP on pristine TiO_2(110). Bond distances are: P-O_{2c} =1.69 Å, P-O_I =1.60 Å, P-O_{II} =2.02 Å, Ti-O_{II}=2.16 Å and Ti-O_I =1.89 Å.

After P-O_{II} bond cleavage, P-O_{III} bond cleavage to transfer another methoxy to the surface would yield intermediate S3 which is 0.97 eV (93 kJ/mol) less stable than S2. After losing two methoxys, the phosphor center of the remaining intermediate forms a bond with surface O3c to re-establish its tetrahedral coordination. The barrier to break the P-O_{III} bond is 1.44 eV (139 kJ/mol).

An alternative path to the second step of dissociation is to cleave the O_{III}-C_{III} bond instead of the P-O_{III} bond, transferring a methyl to surface O_{2c} (S4). This intermediate is 0.24 eV less stable than S2, with a barrier that is even higher of 2.21 eV (213 kJ/mol). These results indicate that decomposition via P-OCH_3 bond cleavage is very unlikely.

The calculated kinetic rate constant at 300K and 600K for the decomposition step of DMMP on the pristine surface are summarized in table 6. At ambient and high temperatures (300 and 600 K), the rate constant for the first P-O_{II} bond cleavage is unsurprisingly small. We conclude that decomposition starting from P-OCH_3 is unlikely. This result is in agreement with previous work by Zhou et. al. which saw no cleavage of P-OCH_3 bond on r-TiO_2(110) in UHV via XPS.[165]

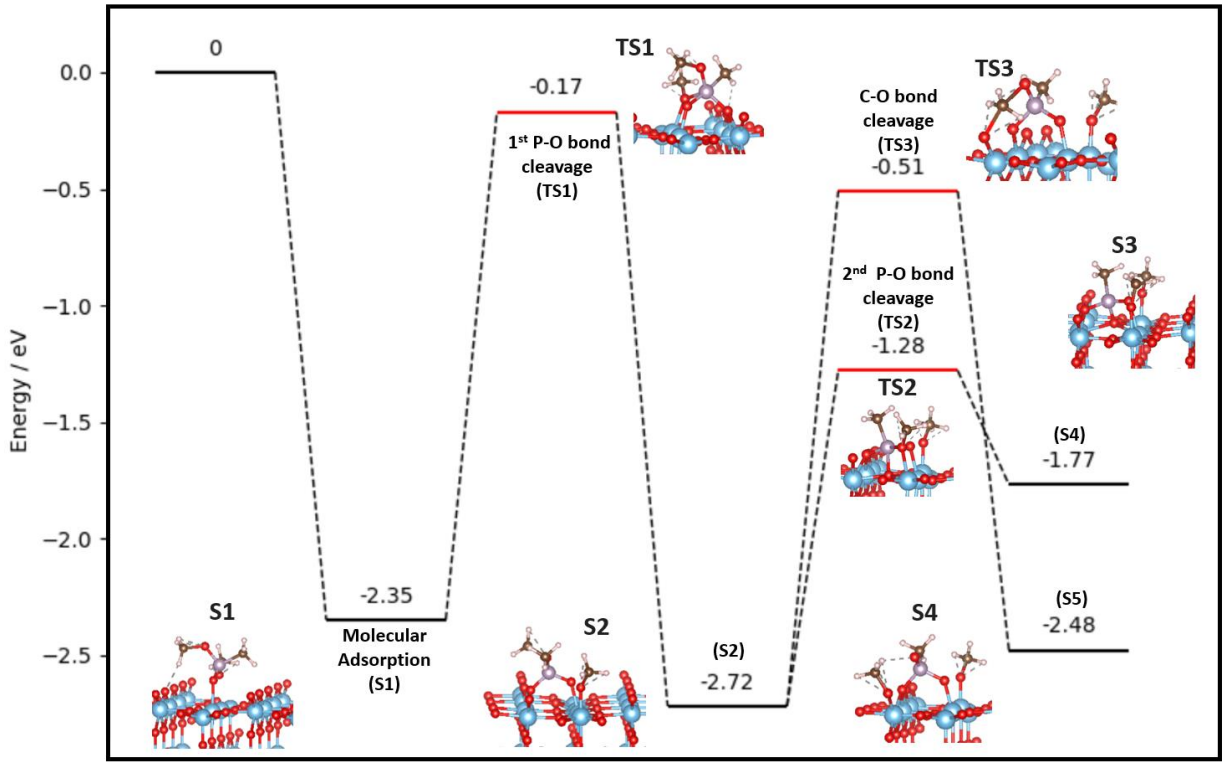

Figure 25 Reaction pathway of DMMP on pristine TiO_2(110) starting by the P-OCH_3 bond cleavage. The reaction proceeds either by breaking a second P-OCH_3 or an O-CH_3 bond.

Table 6 Calculated energies and kinetic rate constants for DMMP decomposition on the pristine r-TiO_2(110) surface via P-OCH_3 cleavage

Reaction coordinate	**S1**	**TS 1**	**S2**	**TS 2**	**S3**	**TS 3**	**S4**
Relative Energy [eV, (kJ/mol)]	-2.35 (-226)	-0.17 (-16)	-2.72 (-262)	-1.28 (-123)	-1.77 (-170)	-0.51 (-49)	-2.48 (-239)
Rate constant at 300K [1/s]	-	2.35E-24	-	5.31E-12	-	9.87E-25	-
Rate constant at 600K [1/s]	-	7.66E-06	-	1.15E+01	-	4.97E-06	-

3.2.4.3. Decomposition on the pristine surface: O-CH_3 bond cleavage-initiated

DMMP decomposition via O-CH_3 bond cleavage may be initiated with the cleavage of O_{II}-C_{II} (methoxy interacting with surface Ti_{5c}) or O_{III}-C_{III} bond. The decomposition pathway via O-CH_3 bond on the pristine surface is depicted in figure 26, with intermediates showcased in the green box representing pathway initiated with O_{II}-C_{II} cleavage and intermediates showcased in the red box representing pathway initiated with O_{III}-C_{III} cleavage.

The barrier to cleave O_{II}-C_{II} bond is expectedly high at 2.17 eV (209 kJ/mol, TS 1a) albeit producing a very stable intermediate S2a at 0.93 eV (89 kJ/mol) lower in energy compared to the adsorbed state. The stability of this intermediate may be attributed to the fact that the phosphor center retains its tetrahedral coordination after bond cleavage. Further O_{III}-C_{III} cleavage yields intermediate S3a, transferring a methyl to nearby O_{2c}. This intermediate is 0.31 eV less stable than intermediate S2a. The barrier to cleave this bond is considerably high at 1.78 eV (172 kJ/mol).

On the other hand, the pathway initiated via O_{III}-C_{III} cleavage has a considerably lower barrier at 1.2 eV. This could be due to C_{III} being positioned closer towards surface O_{2c}. This is ideal for SN_2-like attack by the surface O_{2c}, with inversion of configuration at the carbon, hence shortening the bond cleavage pathway. This step yields intermediate S2b that is 0.29 eV more stable than the molecular adsorption state. As we have seen in the case of pathway a, at this point, cleaving another O-CH_3 bond would bear quite an uphill barrier. Thus, we tried to cleave the P-OCH_3 bond instead, leaving a methoxy on the surface (S3b). Turns out, this intermediate is thermodynamically comparable to S2b with a barrier of 1.53 eV.

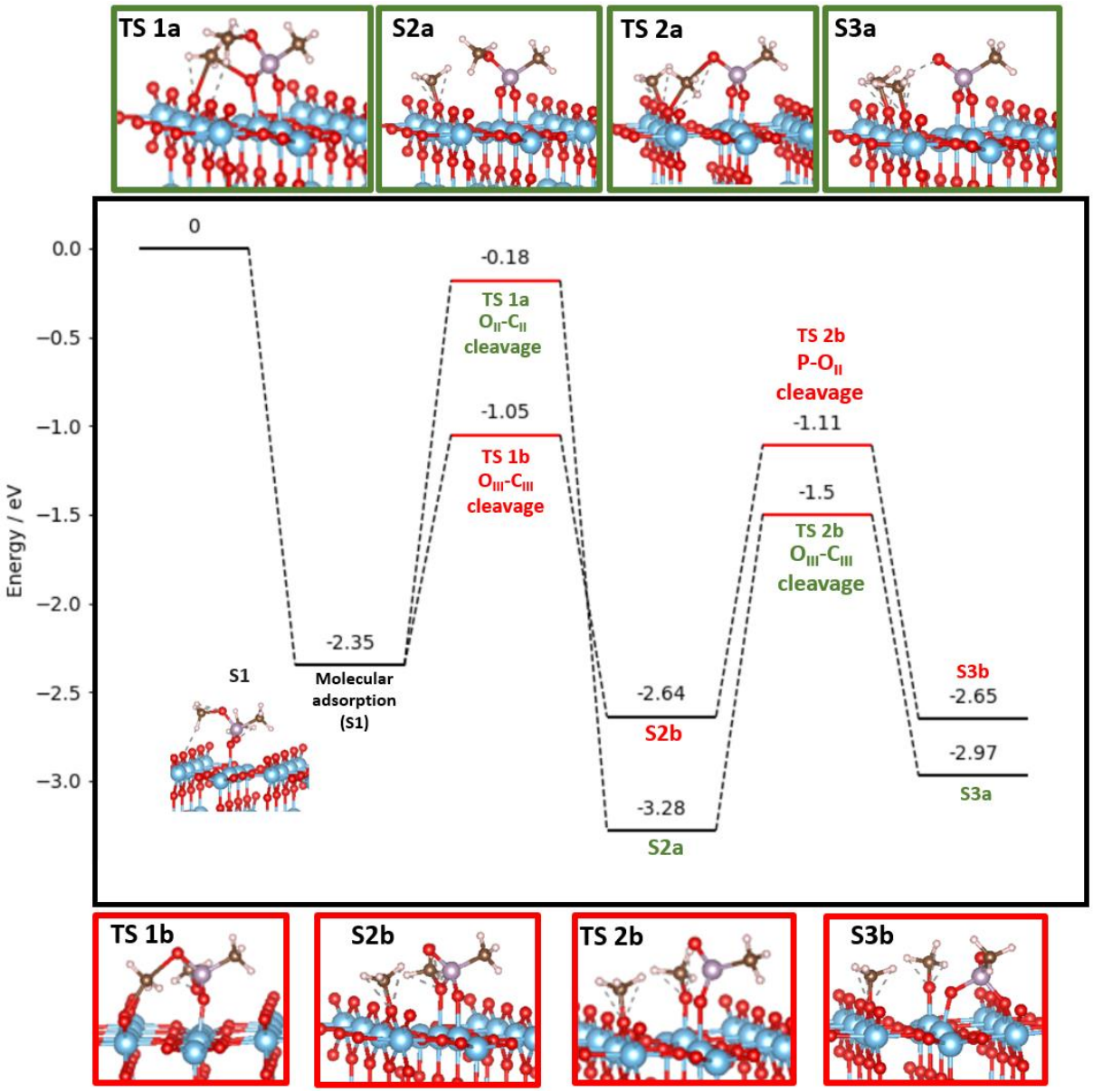

Figure 26 Reaction pathway of DMMP on pristine TiO_2 (110) via O_{II}-C_{II} and O_{III}-C_{III} bond cleavage. Intermediates of decomposition initiated with O_{II}-C_{II} cleavage are highlighted in green boxes (path a), whereas intermediates of decomposition initiated with O_{III}-C_{III} (path b).

Table 7 shows the calculated rate constant of DMMP decomposition initiated by O-CH_3 bond cleavage at 300 K and 600 K. The table shows that decomposition vi O-CH_3 bond cleavage can only be viable at high temperature (600 K) and that it may initiate via O_{III}-C_{III} bond cleavage and not O_{II}-C_{II}.

Table 7 Kinetic rate constants on DMMP decomposition on the pristine surface via O-C bond cleavage

System	**DMMP on TiO2 Pristine, Path O_{II}-C_{II} cleavage**				
Reaction coordinate	**S1**	**TS 1a**	**S2a**	**TS 2a**	**S3a**
Relative Energy [eV, (kJ/mol)]	-2.35 (-226)	-0.18 (-17)	-3.28 (-316)	-1.51 (-145)	-2.97 (-286)
Rate constant at 300K [1/s]	-	3.35E-24	-	1.48E-17	-
Rate constant at 600K [1/s]	-	5.58E-06	-	1.92E-02	-
System	**DMMP on TiO2 Pristine, Path O_{III}-C_{III} cleavage**				
Reaction coordinate	**S1**	**TS 1b**	**S2b**	**TS 2b**	**S3b**
Relative Energy [eV, (kJ/mol)]	-2.35 (-226)	-1.05 (-101)	-2.64 (-254)	-1.11 (-107)	-2.65 (-255)
Rate constant at 300K [1/s]	-	2.36E-09	-	2.14E-13	-
Rate constant at 600K [1/s]	-	2.43E+02	-	2.31E+00	-

3.2.4.4. Decomposition on the pristine surface: P-CH_3 bond cleavage-initiated

Zhou et. al. argues that there is a possibility to observe dissociative adsorption via the P-CH_3 bond.[205] A simple thermodynamic analysis shows that P-CH_3 bond cleavage, transferring a methyl on surface bridging oxygen is unfavorable by 1.14 eV (figure 27a). It is probable that this instability comes stems from phosphor being under-coordinated. We explored the possibility of this geometry being stabilized further by having P interacting with O_{2c} (figure 27b), which still yields a thermodynamically uphill process by 0.39 eV from the molecularly adsorbed state. From geometry c, we then cleaved an additional P-OCH_3 bond (figure 27c). Our calculation showed that the step to cleave additional P-OCH_3 bond yield an intermediate that has higher energy by about 1.49 eV from initial molecular adsorption. There seems to be no tendency for P to interact with surface basal O_{3c}, which causes P to be undercoordinated. This result indicates that further decomposition proceeds via this intermediate are unlikely. Due to uphill thermodynamic analysis of reaction product, pathway searches were not performed to conserve computational time.

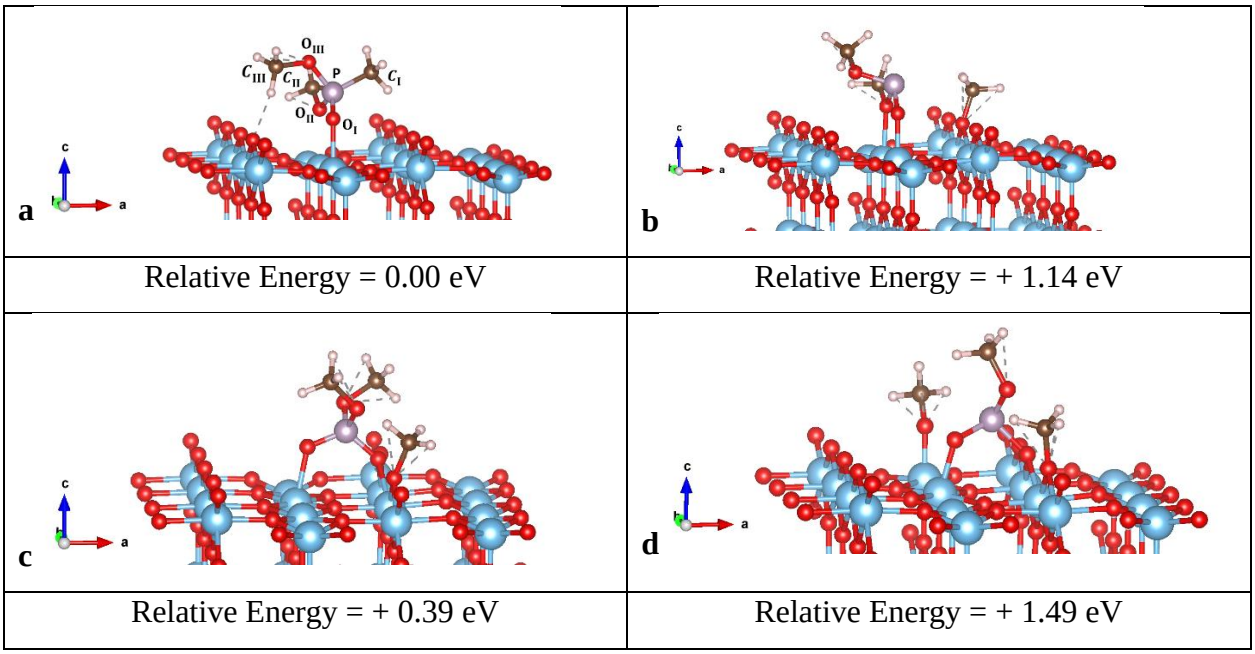

Figure 27 (top) Dissociative DMMP adsorption via cleavage of P-CH_3 bond, leaving a methyl group on surface O_{2c}. (bottom) dissociated DMMP intermediate upon additional cleavage of P-OCH_3 bond. This system is less stable since P is undercoordinated.

3.2.5. DMMP adsorption and decomposition pathway on defective r-TiO_2(110)

3.2.5.1. DMMP adsorption modes on the defective surface

The most stable molecular adsorption modes on the defective surface are showcased in figure 28. DMMP interacts with TiO_2(110) surface via the oxo O_I constituent with the surface oxygen vacancy. Additional interaction of oxygen of DMMP's methoxy group (O_{II}) and neighboring Ti_{5c} further stabilizes this geometry. At a glance, this geometry is akin to the molecular adsorption configuration on pristine TiO_2 surface, with the exception that now O_I is occupying a defect site instead of interacting with a surface Ti_{5c}. This conformation yields adsorption energy of -2.29 eV (221 kJ/mol). The distance between O_I to Ti_{6c} and O_{II} to surface Ti_{5c} is 2.11 Å and 2.42 Å respectively.

Though the P=O prefers to occupy the vacancy, the presence of the oxygen vacancy counterintuitively decreases the adsorption energy by 0.06 eV compared to the pristine surface. This is due to the fact that the formation of the oxygen vacancy leaves two electrons on the surface Ti_{2c} atoms, therefore reducing the Lewis acidity of titania, and weakening the O_{II}-Ti_{2c} interaction.

In comparison to molecularly adsorbed DMMP on the pristine surface, DMMP adsorption on defective surface puts P closer with O_{2c} oxygen on the surface. This can help facilitate the P center to preserve its tetrahedral coordination upon the cleavage of the P-O_{II} by immediately creating a P-O_{2c} bond.

Below we investigate the DMMP decomposition pathway on the defective surface via 3 channels, P-OCH_3, O-CH_3, and P-CH_3 bond cleavage.

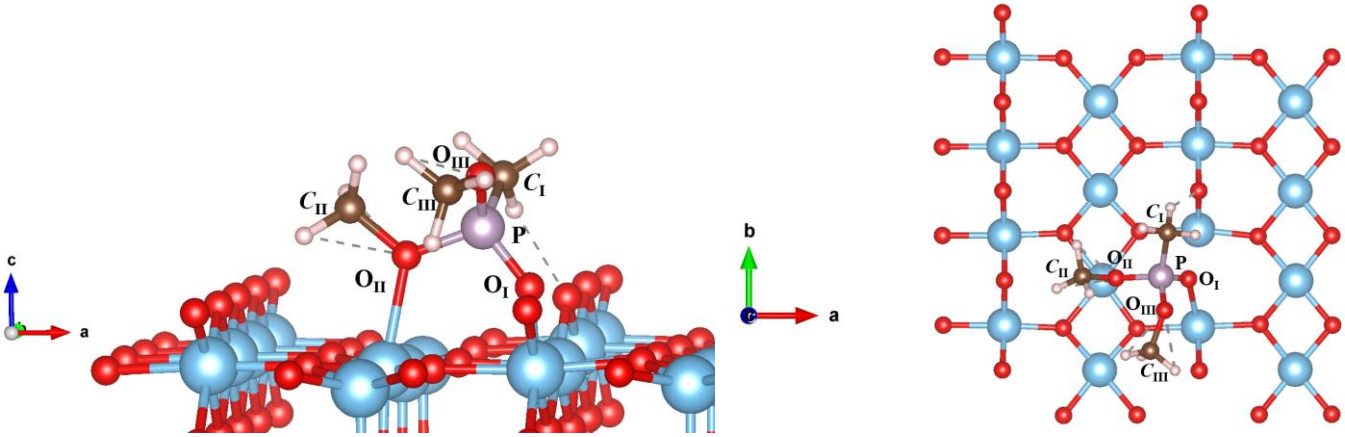

Figure 28 Most stable molecular DMMP adsorption on TiO_2(110) with oxygen vacancy. O_I occupies the oxygen vacancy with an extra interaction of a DMMP methoxy group with surface Ti5c.

3.2.5.2. Decomposition on the defective surface: P-OCH_3 bond cleavage initiated

Starting from the adsorbed state on the defective surface (fig. 28), DMMP decomposition may be initiated via P-O_{II} bond cleavage, leaving a methoxy on surface Ti5c and methyl methyl phosphonate (MMP) whilst adding a new bond between P and surface O2c. Figure 10 shows this DMMP decomposition pathway on the defective surface.

The P-O_{II} bond cleavage yields two possible intermediates (fig. 29), depending on which O_{2c} the phosphor center is interacting with after P-O_{II} bond cleavage. In both cases, the barrier to cleave P-O_{II} bond, yielding intermediates S2 green and blue is significantly lower compared to the barrier to cleave P-OCH_3 bond on the pristine surface. We postulate that this is due to P being geometrically accessible to the surface O_{2c}. P-O_{2c} bond creation after P-O bond cleavage helps stabilize the remaining phosphor-containing intermediate.

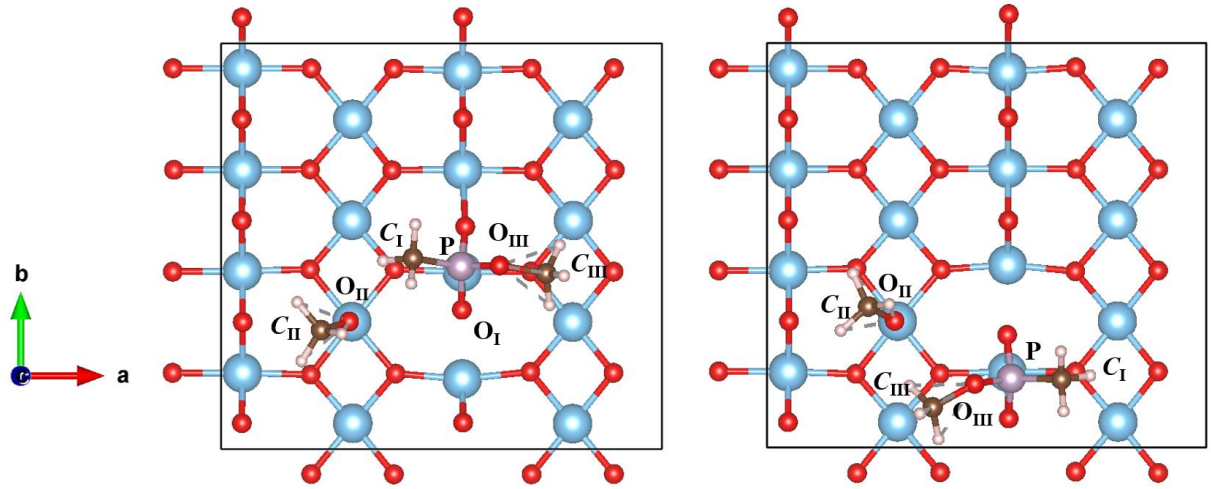

Figure 29 Intermediate isomers upon P-O_{II} bond cleavage on defective TiO_2(110). (left) the methoxy substituent of MMP is facing away from the adsorbed methoxy, decomposition steps follow the 'green pathway'. (right) the methoxy substituent is facing towards the adsorbed methoxy, decomposition steps follow the 'blue pathway'.

The two intermediates isomer upon P-O bond cleavage differs by only the placement of its methoxy substituent of the remaining methyl methylphosphonate (MMP). The first isomer (fig. 28, left) corresponds to the case where the methoxy substituent of MMP (O_{III}-C_{III}) is facing away from the surface-bound cleaved methoxy group. This geometry will start the *'green pathway'*. The second isomer (fig. 9, right) places the methoxy substituent of MMP (O_{III}-C_{III}) facing towards the adsorbed methoxy (O_{II}-C_{II}). The pathway following this second intermediate will be denoted as the *'blue pathway'*.

Both isomers have similar adsorption energy as it can be expected, -2.25 eV and -2.37 eV for green and blue pathways, respectively. This indicates that the P-O_{II} bond cleavage yields intermediates with similar stability as the molecularly adsorbed DMMP (E = -2.29 eV). The barrier to cleave the first P-O_{II} bond is 1.47 eV and 1.41 eV for the green and blue pathways, respectively. The transition state for both isomers involves P interacting with bridging O2c rows prior to the P-O_{II} bond cleavage (see figure 30, TS1 green and blue).

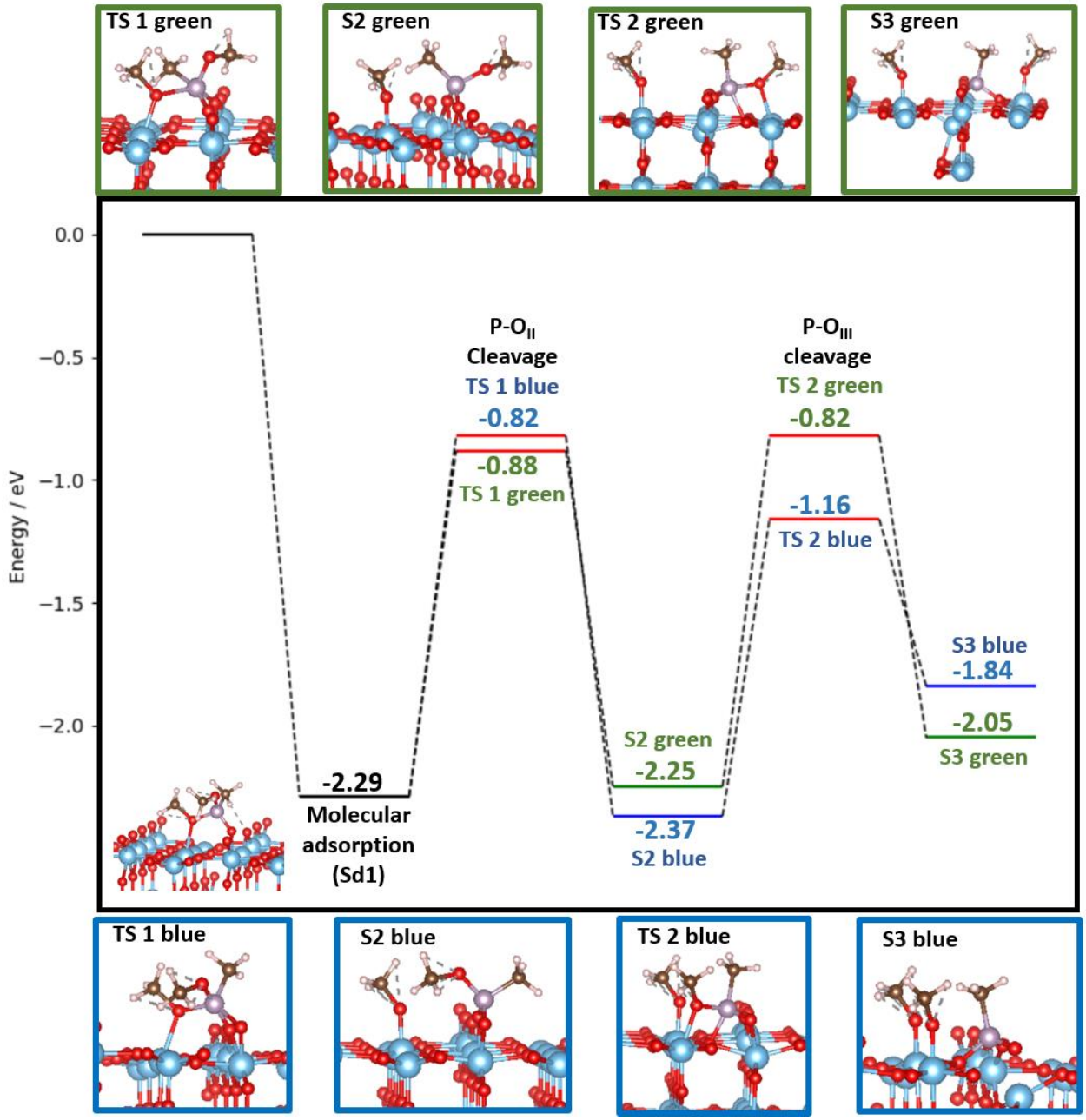

Figure 30 DMMP decomposition initiated via P-O$_{II}$ bond cleavage on r-TiO$_2$(110) with one O vacancy. Intermediates in green and blue depict decomposition following two possible isomers after P-OII bond cleavage.

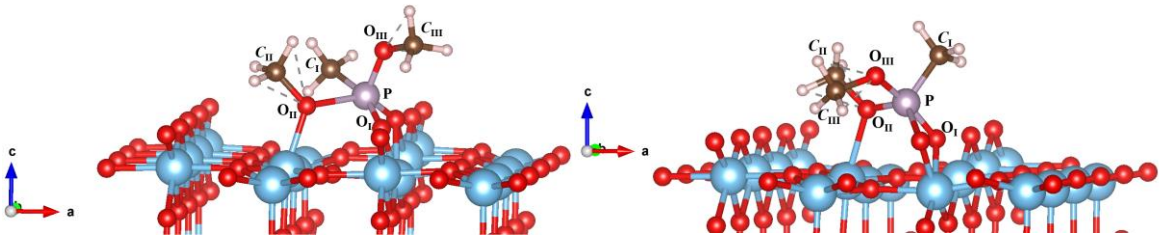

Figure 31 (Left) Transition state of P-O cleavage for green isomer, (right) transition state for blue isomer.

Subsequent P-O_{III} bond cleavage on MMP after the initial P-O_{II} bond cleavage yields two isomers again. This is due to the difference of where the methoxy constituent of MMP was facing prior to the second P-OCH_3 dissociation step, subsequent breaking of the P-OCH_3 bond leads to the transfer of the second methoxy on different Ti_{5c} rows on the surface (figure 32).

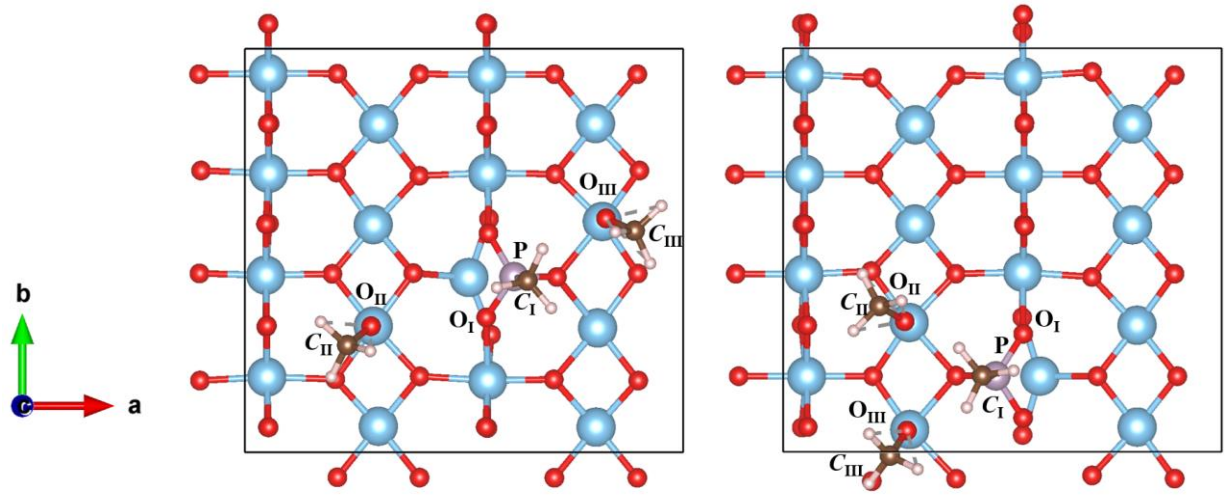

Figure 32 (left) green pathway intermediate upon second P-O bond cleavage. (right) isomer in the blue pathway

Following the green pathway, the subsequent breaking of the P-O_{III} bond forms an intermediate (S3 green on fig 30 and figure 32 left) which is less stable by 0.24 eV (23 kJ/mol) with respect to the molecularly adsorbed DMMP. P clearly tries to conserve its tetrahedral coordination as it creates a new bond with surface O_{3c} upon P-O_{III} bond cleavage. This configuration forces Ti_{6c} underneath P to shift downwards by 0.64 Å. The barrier to break the P-O_{III} is moderate (1.43 eV).

On the blue pathway, however, after the second P-O bond cleavage (P-O_{III}) methoxy groups are adsorbed on the same Ti5c row (Figure 32 right). This intermediate is less stable than its equivalent isomer in the green pathway. This intermediate is higher in energy, less stable by 0.45 eV (43 kJ/mol) with respect to the molecularly adsorbed DMMP. This is likely due to the proximity of the surface-bound methoxy groups. However, the barrier to break the P-O_{III} bond through this isomer is slightly lower (1.21 eV, 117 kJ/mole) in comparison to its counterpart isomer in the green pathway.

Table 8 shows the kinetic rate constants for DMMP P-OCH_3 bond cleavage on the defective surface. In comparison to the case of the pristine surface, the decomposition initiated via P-OCH_3 on the defective surface is kinetically faster. At room temperature, the kinetic rate constant for every decomposition step is extremely small, similar to those on the pristine surface. However, fast rate constants (~10 s^{-1}) are obtained at 600 K, where the first decomposition step is 6 orders of magnitude faster than that on the pristine surface.

Table 8 Calculated energies and kinetic rate constants for DMMP decomposition on the defective r-TiO2(110) surface via O-PCH$_3$ bond cleavage.

System	**DMMP on TiO2 Defect, P-O bond cleavage, Green (2 OCH$_3$ transferred to different Ti$_{5c}$ row)**				
Reaction coordinate	**S1**	**TS 1**	**S2**	**TS 2**	**S3**
Relative Energy [eV, (kJ/mol)]	-2.29 (-220)	-0.88 (-84)	-2.25 (-217)	-0.82 (-79)	-2.05 (-198)
Rate constant at 300K [1/s]	-	1.43E-11	-	9.24E-12	-
Rate constant at 600K [1/s]	-	1.89E+01	-	1.52E-01	-
System	**DMMP on TiO2 Defect, P-O bond cleavage, Blue (2 OCH$_3$ transferred to the same Ti$_{5c}$ rows)**				
Reaction coordinate	**S1**	**TS 1**	**S2**	**TS 2**	**S3**
Relative Energy [eV, (kJ/mol)]	-2.29 (-220)	-0.82 (-79)	-2.37 (-228)	-1.16 (-111)	-1.84 (-177)
Rate constant at 300K [1/s]	-	1.70E-12	-	2.90E-08	-
Rate constant at 600K [1/s]	-	6.51E+00	-	8.52E+02	-

3.2.5.3. Decomposition on the defective surface: O-CH$_3$ bond cleavage-initiated

Figure 33 depicts the reaction pathway initiated via O-CH$_3$ bond cleavage on the defective surface. Upon adsorption, there are again two possible O-CH$_3$ bonds to cleave, O_{II}-C_{II} which interacts with surface $Ti_{5c,}$ and the O_{III}-C_{III} bond which interacts with bridging O_{2c} row via van der Waals interactions.

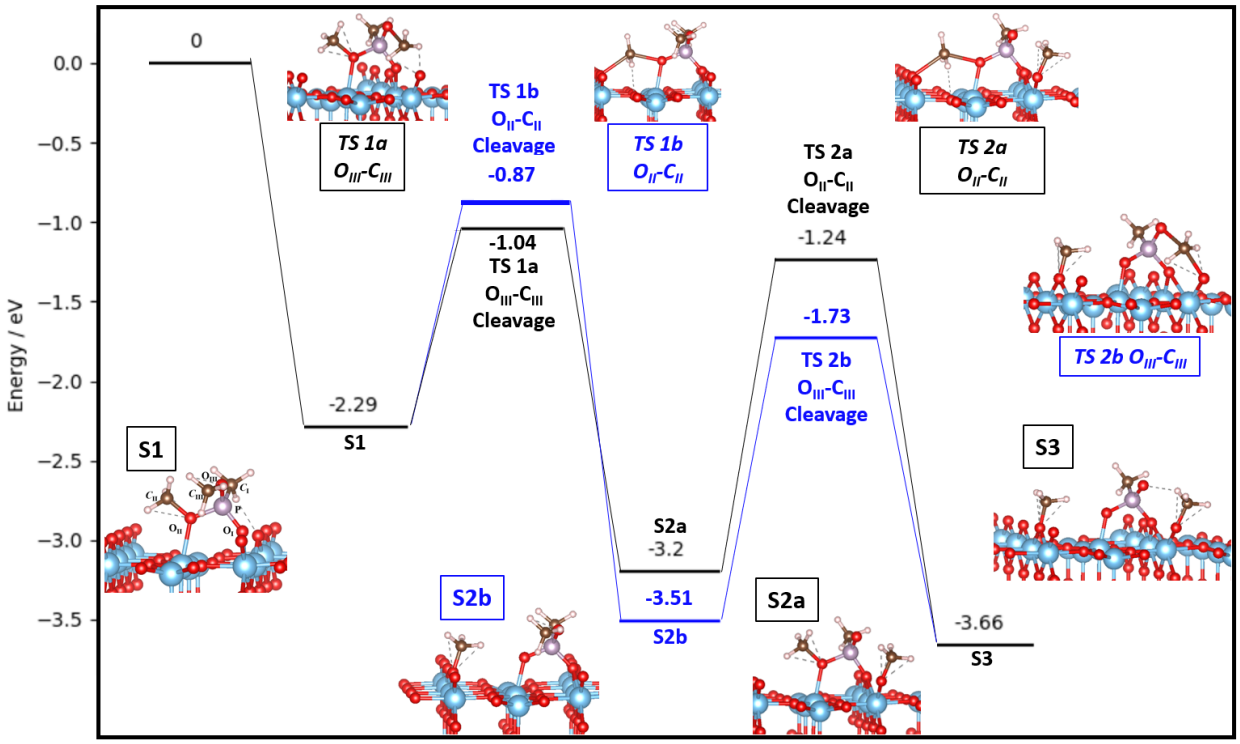

Figure 33 DMMP decomposition initiated via P-O_{II} bond cleavage. Intermediates in green and blue depict decomposition following two possible isomers after P-O_{II} bond cleavage.

The path initiated via O_{III}-C_{III} bond cleavage (denoted as the black path in figure 33), yields a very stable intermediate (S2a), 0.91 eV more stable than chemisorbed DMMP, leaving a methyl on the same bridging oxygen row, beside the remaining $P(OTi_2)(CH_3)(OCH_3)$ surface species. The barrier to cleave this bond is 1.25 eV. A second decomposition step can follow with the O_{II}-C_{II} bond cleavage. The formed intermediate (S3) is 0.46 eV more stable than S2a and the barrier to cleave this O_{II}-C_{II} bond is 1.96 eV.

The path initiated via the O_{II}-C_{II} bond (denoted as the blue path in figure 33), yields an even more stable intermediate (S2b, -3.51 eV), leaving a methyl on the opposite bridging oxygen row of the remaining P fragment. This intermediate is 1.22 eV more stable than the adsorption state. The barrier to cleave this bond is 1.42 eV. A second decomposition step can follow with the O_{III}-C_{III} bond cleavage, yielding S3 after passing a barrier of 1.78 eV.

In both cases above we investigated the P-OCH_3 bond cleavage as a following cleavage step after the first O-CH3 bond cleavage. In both cases, the P-OCH_3 bond cleavage is thermodynamically unfavorable. The possible intermediates from cleaving the P-OCH_3 bond after breaking the O-CH_3 bond are listed in figure 34. From S2a (after O_{III}-C_{III} bond cleavage), cleaving P-O_{II} (fig 33, left) yields an intermediate that is 0.29 eV less stable than S2a. The barrier for this step is 2.22 eV (not depicted in figure 13 for clarity). From S2b (after O_{II}-C_{II} bond cleavage), cleaving P-O_{III} (fig 33, right) yields an intermediate that is 1.6 eV less stable than S2b. Since the intermediates are not thermodynamically stable, we did not calculate the barrier for these steps.

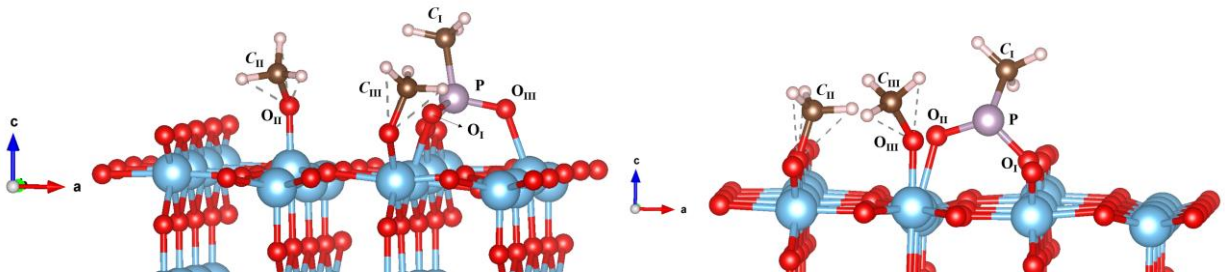

Figure 34 Intermediates from P-O bond cleavage after O-C bond cleavage on the defective surface. (Left) P-O_{II} bond dissociation from S2a (right) PO_{III} bond dissociation from S2b

Table 9 shows the kinetic rate constants for decomposition initiated via O_{III}-C_{III} and O_{II}-C_{II} bond cleavage on the defective surface. We see that at high temperatures (600 K), the first dissociation step either via O_{III}-C_{III} or O_{II}-C_{II} bond cleavage (TS 1a and TS1b) proceeds considerably fast, despite further decomposition seems to be difficult still. Full decomposition is still more viable via P-O bond cleavage on the defective surface.

Table 9 Calculated energies and kinetic rate constants for DMMP decomposition on the defective r-TiO2(110) surface via O-C bond cleavage

System	**O_{III}-C_{III} bond cleavage initiated (Black)**				
Reaction coordinate	**S1**	**TS**	**S2a**	**TS 2**	**S3a**
Relative Energy [eV, (kJ/mol)]	-2.29 (-220)	-1.04 (-100)	-3.20 (-318)	-1.24 (-119)	-3.66 (-353)
Rate constant at 300K [1/s]	-	7.39E-09	-	1.06E-20	-
Rate constant at 600K [1/s]	-	4.30E+02	-	5.14E-04	-
System	**O_{II}-C_{II} bond cleavage initiated (Blue)**				
Reaction coordinate	**S1**	**TS**	**S2b**	**TS 2**	**S3b**
Relative Energy [eV, (kJ/mol)]	-2.29 (-220)	-0.87 (-83)	-3.51 (-338)	-1.73 (-167)	-3.66 (-353)
Rate constant at 300K [1/s]	-	1.14E-11	-	1.35E-17	-
Rate constant at 600K [1/s]	-	1.69E+01	-	1.83E-02	-

3.2.5.4. Decomposition on the defective surface: P-CH_3 bond cleavage-initiated

Finally, we investigated the P-CH_3 bond cleavage-initiated pathway on the surface with O vacancy. The thermodynamic analysis showed that the oxygen vacancy does not help to stabilize the intermediate after P-CH_3 bond cleavage (fig. 35). This intermediate is 0.91 eV less stable than the adsorbed state. There seems to be no tendency for P to interact with surface basal O_{3c}, which causes P to be undercoordinated. Even with an additional P-OCH_3 bond cleaved and with a P-O_{3c} interaction, the stability does not seem to improve (adsorption energy 1.08 eV higher with respect to most stable molecularly adsorbed DMMP). We conclude that the P-CH_3 bond cleavage is unlikely on TiO_2.

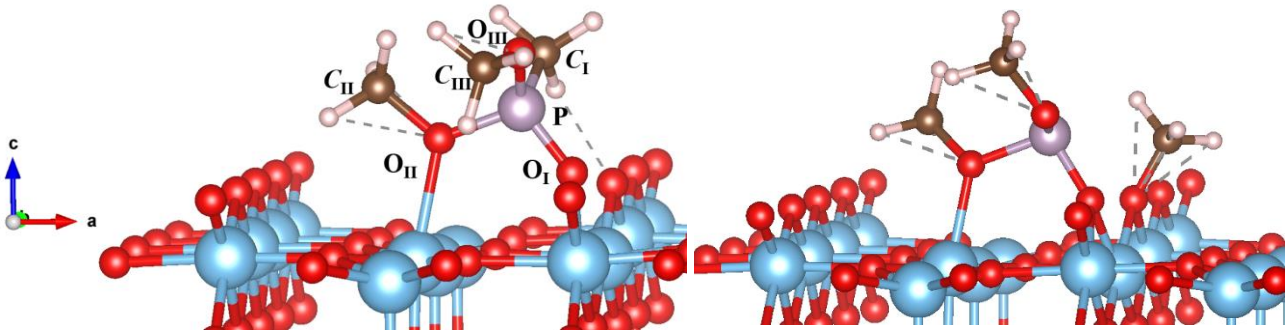

Figure 35 (left) Molecularly adsorbed DMMP on O vacancy. (Right) Subsequent intermediate resulting from P-C bond cleavage.

3.2.6. Discussion: Possible reaction pathways

We observed that on pristine r-TiO_2(110) molecular adsorption is highly stable via the interaction between the oxo constituent and surface Lewis acid Ti_{5c}. This configuration is very often observed in other metal oxide systems and metal-organic frameworks as mentioned in the literature search section. [50,51,60,61,52–59] DFT calculations indicate that decomposition via P-OCH_3 cleavage leads to stable intermediates but is very slow kinetically. Decomposition via P-CH_3 bond is simply thermodynamically uphill. O-CH_3 bond cleavage is the most favorable elementary reaction step, though the barrier can only be passed at high temperature (600 K), forming a surface methoxy species on the bridging oxygen row. This formation of surface methoxy groups agrees with the TPD result which detects a small amount of methanol and formaldehyde at 650 K, suggesting that these products are the result of surface methoxy disproportion. On all decomposition pathways, the remaining PO_3CH_3 species remains stable on the surface, with phosphor center forming tetrahedral coordination with surface oxygens.

Comparison with other rutile-form metal oxide shows similar adsorption geometries of DMMP. A DFT-based thermodynamic analysis of DMMP decomposition by Housaindokht et. al. on r-SnO_2(110) shows two most promising dissociative adsorption of DMMP involves the transfer of methyl to a nearby O_{2c} with the remaining phosphor-containing intermediate preserving its

bidentate structure.[206] Our kinetic analysis further highlights the importance of accessibility of surface metal cation and Lewis basic sites towards reactivity.

Further, we are interested in the effect of surface oxygen vacancy on surface reactivity. A common property of r-TiO_2(110) is the presence of bridging oxygen vacancies in UHV condition which is known to be able to act as active sites for many reactions. We cannot remove the possibility of P-OCH_3 bond cleavage dissociation, facilitated by the surface defect.

DFT calculations found that oxygen vacancy defects on the surface do indeed may serve as active sites. Adsorption of DMMP on the O vacancy is stable, similarly to the adsorption on the pristine surface, though with the P=O group occupying the vacancy instead of interacting with Ti_{5c}. Such adsorption of DMMP on the vacancy was found to lower the barrier of P-OCH_3 bond cleavage, helping in transferring a methoxy to surface Ti5c. The calculated kinetic rate constants suggest that the P-OCH_3 bond cleavage would become favorable at around 600K on the oxygen vacancy-containing surface. Subsequent second P-OCH_3 bond scission was found to be favorable as well at 600K, with the remaining phosphorus group forming tetrahedral coordination with surface oxygen. The alternative option of an O-CH_3 bond cleavage-initiated decomposition is also easier on the vacancy-containing surface, though full decomposition afterward is difficult. Lastly, similar to the case of pristine surface, P-CH_3 bond cleavage on the defective surface was found to be unstable and thus unlikely to happen both on the pristine and defective surface.

The results indicate that the O-CH_3 bonds on DMMP are the easiest to cleave, but that P-OCH_3 bond cleavage can also occur at high temperatures in the presence of O vacancies. The products of DMMP decomposition remain strongly bound to the surface, hence poisoning it. Overall, the reactivity of DDMP on r-TiO_2(110) is weak, leading to partial desorption at low temperature, and decomposition only at high temperature (600 K). TiO_2 appears as a good support to place a DMMP decomposition catalyst since the molecule reactivity is low, but the decomposition products are highly stable on the support. This could help decomposition products migrate from the catalyst to the support, hence freeing the catalyst for the next cycle. Removing decomposition products from the catalytic site is indeed a key question and poisoning of the site by-products has been reported for example on MOF catalysts[67]

Comparison to past experimental studies on TiO_2 systems

Thermal reactivity studies of DMMP on TiO_2 were previously done by Panayotov, Yates, and Zhou. Panayotov and Yates worked on FTIR of DMMP decomposition on Degussa sample. Unsurprisingly, our work does not fully agree with the result done on the Degussa TiO_2 powder sample. IR spectroscopy by Yates suggests that P-OCH_3 bond cleavage is facile at 214 K, and at around 468 K second P-OCH_3 bond dissociation is observed.[10] This was expected and we argue that the P-OCH_3 bond cleavage seen by Yates et. al. is due to the fact that their sample is hydroxylated whereas ours is in UHV condition. However, our results agree with both works where they did not observe P-CH_3 bond cleavage before P-OCH_3 bond cleavage. The stable, final PO_3CH_3 intermediate after full decomposition corroborates the findings of Panayotov et. al. using XPS and FTIR, showing that the P-CH_3 bond is intact up to 800K.[163] Few accounts on DMMP

decomposition on metal oxides such as Al_2O_3 and MOF suggest that surface hydroxyl promote the P-OCH_3 bond dissociation.[62,67,68,70]

On the other hand, XPS, Principal Component Analysis (PCA), and TPD by Zhou et. al. on r-TiO2(110) in UHV condition corroborates our results better.[165] Zhou reported intact P-OCH_3 at room temperature, possibly coming from molecularly adsorbed DMMP. Similar to our TPD results, Zhou saw molecular desorption of DMMP up to 550 K. However, no methanol and formaldehyde production was observed, instead, methane and hydrogen are the primary products under 700 K, with phosphor containing residues stay on the surface even after heating up to 1000K. XPS and PCA analysis suggest that the P-OCH_3 bond cannot be broken before the P-CH_3 bond and suggest that dissociative adsorption via the P-CH_3 bond is a possible pathway. However, this work did not consider dissociation initiated via O-CH_3 bond cleavage to transfer a methyl on surface bridging oxygen. Additionally, Zhou did not confirm the existence of defects on their surface sample. Our work agreed that P-OCH_3 bond cleavage is difficult and suggest a new possible pathway that is kinetically accessible.

3.2.7. Conclusion

In this work, we have performed DFT calculations and TPD experiments on thermal DMMP decomposition on both pristine and defect surfaces of TiO_2 (110). Molecular adsorption on pristine surface happens via P=O group interaction with Ti_{5c} and additional methoxy interaction with the surface. On the defect surface, DMMP adsorbs similarly with P=O occupying the vacancy site. Our reaction pathway search reveals that the O-CH_3 bond is a viable pathway for DMMP decomposition on the pristine surface. We also reveal that oxygen vacancy helps reduce the energy barrier for initial P-OCH_3 breaking to initiate DMMP decomposition. Kinetic rate constant approximation suggests that these reactions may start at a high temperature around 600 K.

3.3. Part 3: Comparison of DMMP and Sarin chemistries on pristine and defective r-TiO_2(110) on selected pathways

This section compares the decomposition of DMMP and Sarin on selected pathways in order to probe whether DMMP is a sufficient simulant in describing the chemical behavior of sarin. For readability purposes during comparison with DMMP, the bond between the phosphor center of sarin and its alkoxy group will be denoted as P-O_{alko}. This work presents key decomposition pathways such as the P-O_{alko}, P-F, and O-C bond cleavage on both pristine and defective surfaces.

3.3.1. Computational Set-up

This work uses the same computational setup as section 3.2.

3.3.2. Sarin decomposition pathway on pristine r-TiO_2(110)

3.3.2.1. Sarin adsorption modes on the pristine surface

DFT calculations showed four stable adsorption geometries of Sarin on pristine TiO_2(110). Two geometries (Figure 25, geometry A and B) are somewhat analogous to the most stable molecular DMMP adsorption state. In both cases, sarin adsorbs via the oxygen of P=O group interaction with surface titanium, alongside with added stabilizing interaction via either fluorine (adsorption energy of -1.94 eV) or alkoxy (adsorption energy of -1.92 eV) interacting with neighboring Ti. Due to the size of the alkoxy group of sarin, there is always a van der Waals interaction with the surface even when sarin adsorbs only via P=O-Ti bond (adsorption energy of -1.80 eV). The unique adsorption mode of sarin involves interaction between fluorine and surface Ti, with additional interaction of alkoxy (adsorption energy of -1.13 eV). This is analogous to DMMP adsorbing via the interaction of two methoxys with the surface.

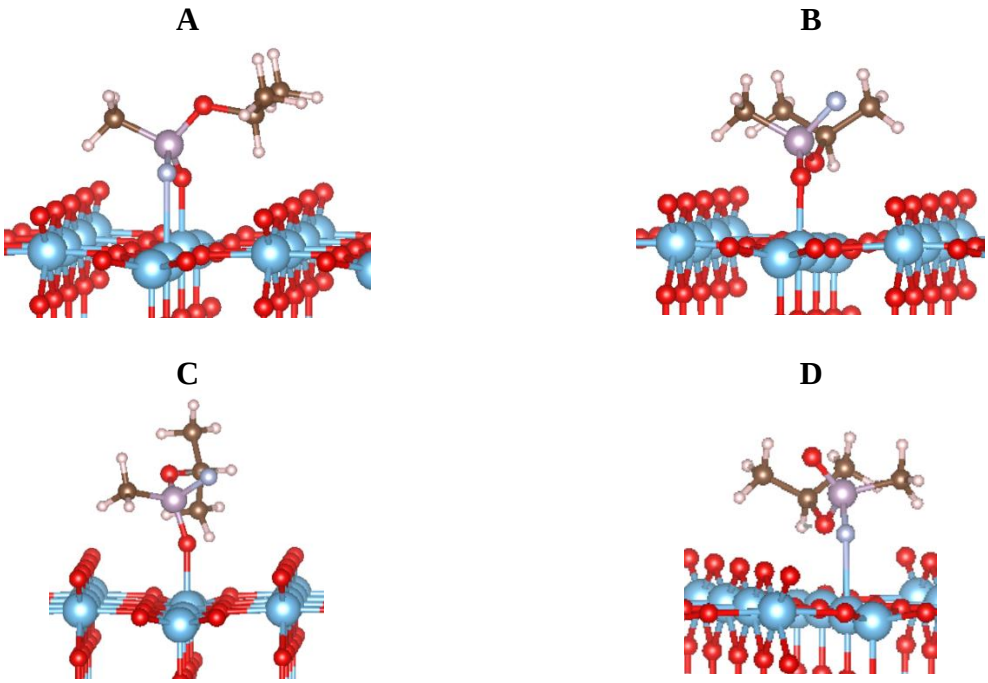

Figure 36 Most stable molecular sarin adsorption geometries

3.3.2.2. P-O and P-F bond cleavage initiated path

As described in the previous sections, the P-O bond cleavage in the case of DMMP is equivalent to two types of bond cleavage in sarin: namely the P-F and the P-O_{alko} bonds. To mimic the decomposition initiated via P-O bond cleavage in the case of DMMP, we start the decomposition of sarin from molecular adsorption geometry A (figure 26) for P-F bond cleavage-initiated decomposition and molecular adsorption geometry B for P-Oalko bond cleavage-initiated decomposition.

Starting from molecular adsorption geometry A, where alkoxy is interacting with surface Ti, the barrier to cleave the P-O_{alko} bond is extremely uphill at 2.27 eV (fig. 37). This is as expected and very much similar in the case of DMMP where the first P-O bond cleavage must overcome a barrier of 2.18 eV. P-O_{alko} bond cleavage yields intermediate S2, which is more stable by 0.64 eV from the adsorbed state. Subsequent P-F bond cleavage is thermodynamically uphill by 0.66 eV from intermediate S2, with a barrier of 1.49 eV.

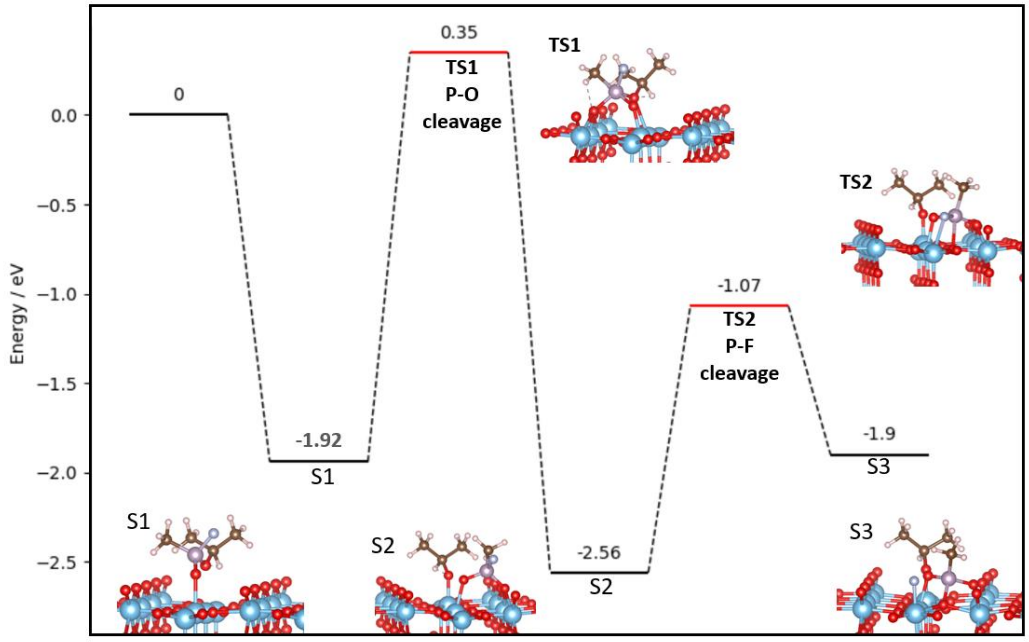

Figure 37 Sarin decomposition on pristine TiO_2(110), following the P-O bond cleavage initiated pathway.

If we instead initiate the decomposition with P-F bond cleavage (starting from molecularly adsorbed geometry B), the barrier to cleave P-F bond is somewhat less than those of P-Oalko, at 1.78 eV. Figure 38 shows the decomposition pathway initiated via P-F bond cleavage. P-F bond cleavage yields intermediate (fig 38, S2) that is 0.96 eV more stable than the adsorbed geometry. It seems that both P-O_{alko} and P-F bond cleavage is thermodynamically very stable, similar to P-O bond cleavage in DMMP. Subsequent P-O_{alko} bond cleavage is however more difficult in comparison to subsequent P-F bond cleavage. The barrier for this P-Oalko cleavage from S2 is 1.67 eV. The fully decomposed phosphor-containing residue is less stable by 0.66 eV from S2, although its stability is comparable to the molecular adsorption state. The two pathways have

consistently shown that it is easier to cleave the P-F bond than to cleave the P-O_{alko} bond. The stability of intermediates is somewhat comparable to the case of DMMP, as both pathways initiated with P-F and P-O_{alko} bond cleavage exhibit a similar pathway to the case of DMMP if compared qualitatively with the first decomposition step having a barrier of around 2 eV, and second decomposition step having a barrier of around 1.5 eV.

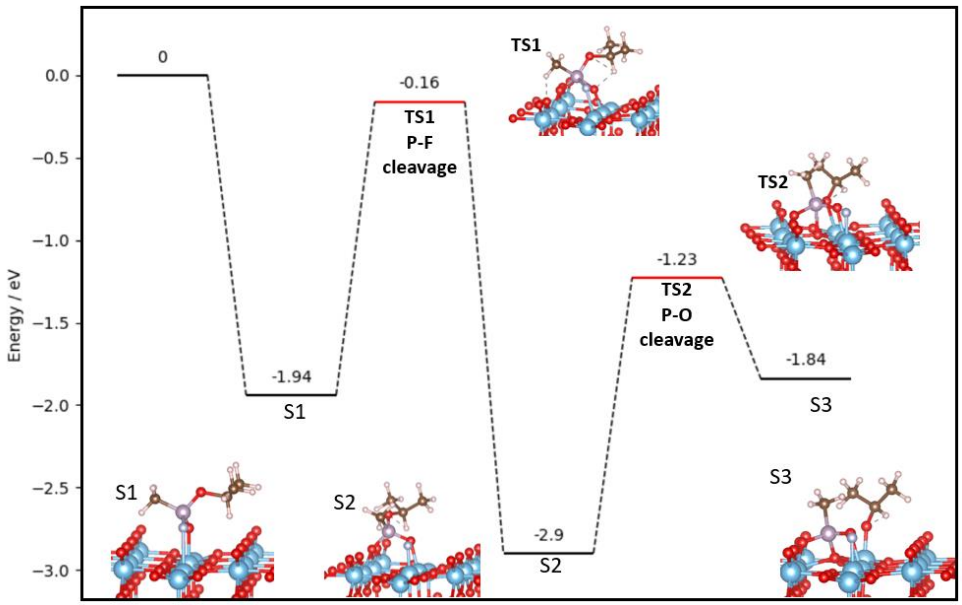

Figure 38 Sarin decomposition on pristine TiO_2(110) initiated with P-F bond cleavage.

3.3.2.3. O_{alko}-C bond cleavage initiated path

After having a general idea of how well P-F bond and P-O_{alko} bond cleavage barriers compare to P-O bond cleavage in the case of DMMP, we explored the ability of surface oxygen to activate the O_{alko}-C bond as well. O_{alko}-C bond cleavage can only be cleaved from geometry A (Fig. 25). This is analogous to DMMP's O_{III}-C_{III} bond. The barrier to cleave this bond is 1.17 eV. This is very close to the barrier to cleave the O_{III}-C_{III} bond in DMMP which stands at 1.2 eV. Oalko-C bond cleavage results in an intermediate that is more stable by 0.29 eV. This is equal to the case of DMMP where the O_{III}-C_{III} brings the system downhill by 0.29 eV as well. We conclude that the bond strength and the ability of the surface to activate the O-C bond for sarin and DMMP are almost identical. Figure 28 depicts these bond cleavage steps.

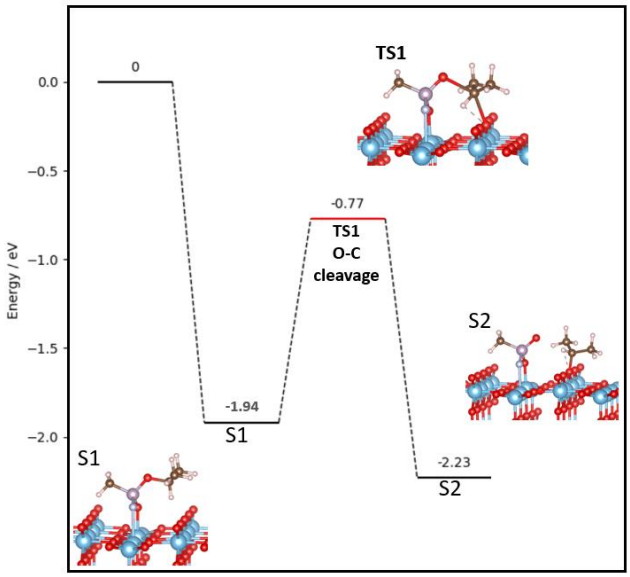

Figure 39 O-C bond cleavage on molecularly adsorbed sarin on pristine TiO_2 (110).

3.3.3. Sarin decomposition pathway on defective r-TiO_2(110)

Lastly, we probe the effect of surface defects, mainly oxygen vacancy towards the activation of P-F and P-O_{alko} bonds. As described in section 3.2, surface oxygen vacancy may help the activation of P-OCH_3 bond cleavage in the case of DMMP. Here we perform similar calculations on sarin to see if sarin may exhibit similar behavior.

3.3.3.1. Sarin adsorption modes on the defective surface

DFT calculations found 4 stable adsorption modes of sarin on defective TiO2(110) surface. In all four cases, sarin interacts with the surface via the P=O group filling the surface oxygen vacancy. Figure 29 shows the four molecular adsorption geometries, named Defect A, B, C, and D. Defect A configuration involves only P=O bond occupying the oxygen vacancy, with adsorption energy of -2.00 eV. Additional interaction between F-Ti (Defect B) sees a decrease in adsorption energy to -1.95 eV. In geometry defect C additional stabilization occurs via van der Waals interaction between the alkoxy and surface titania row with an adsorption energy of -2.13 eV. The most stable sarin adsorption geometry, defect D, is very much analogous to the best adsorption geometry of DMMP on the defective surface where there is an interaction between the oxygen of alkoxy and surface Ti^{4+}. This final and best geometry yields adsorption energy of 2.2 eV. Overall, the additional interaction stemming from alkoxy with surface stabilizes the system, whereas the interaction between fluorine and surface destabilizes the system. Fluorine does not want to form close interaction with surface Ti_{5c}.

Subsequent decomposition from molecular adsorption follows geometry defect D for P-O cleavage and geometry B for P-F cleavage.

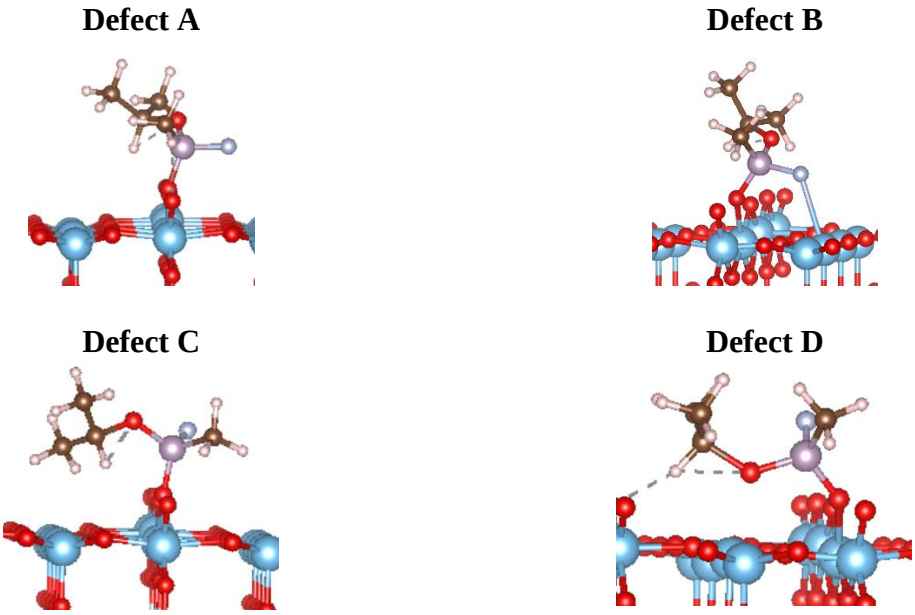

Figure 40 Stable molecular adsorption of sarin on defective TiO2(110) surface.

3.3.3.2. P-O and P-F bond cleavage initiated path

Similar to the case of DMMP decomposition, following the P-O_{alko} bond cleavage sarin could conform to two possible intermediates, one in which the fluorine group of sarin facing towards ('up' pathway) or away ('down' pathway) from surface isopropoxy. In any case, P-O_{alko} bond cleavage has barriers of 1.16 eV (for TS1 up) and 1.05 eV (for TS1 down) respectively. These barriers are lower in comparison to the barriers to cleave P-O bond in the case of DMMP which requires energies of 1.41 and 1.47 eV. We postulate that this is due to the size difference between fluorine (on sarin) and methoxy (on DMMP), which reduces any hindrance during the bond cleaving process. P-Oalko bond cleavage yields intermediate S1 up (F facing towards isopropoxy) and S1 down (F facing away from isopropoxy) with comparable energies with the molecularly adsorbed sarin (S1). The energies are 2.1 and 2.24 eV respectively. Qualitative-wise this step is very similar to the case of DMMP whereupon P-O bond cleavage, the resulting intermediates have similar stability with the molecularly adsorbed DMMP state.

Subsequent P-F bond cleavage yields intermediate S2, leaving a residue of PO_3CH_3 species on the surface. Transferring F either on the same or different row from the previously adsorbed isopropoxy does not result in a significant difference in energy (-2.08 and -2.1 eV for F and isopropoxy on the same and different row, respectively). In the case of DMMP, however, the isomer where the two methoxys are adsorbed beside each other is slightly less stable by 0.21 eV in comparison when the two methoxys are adsorbed on different Ti rows.

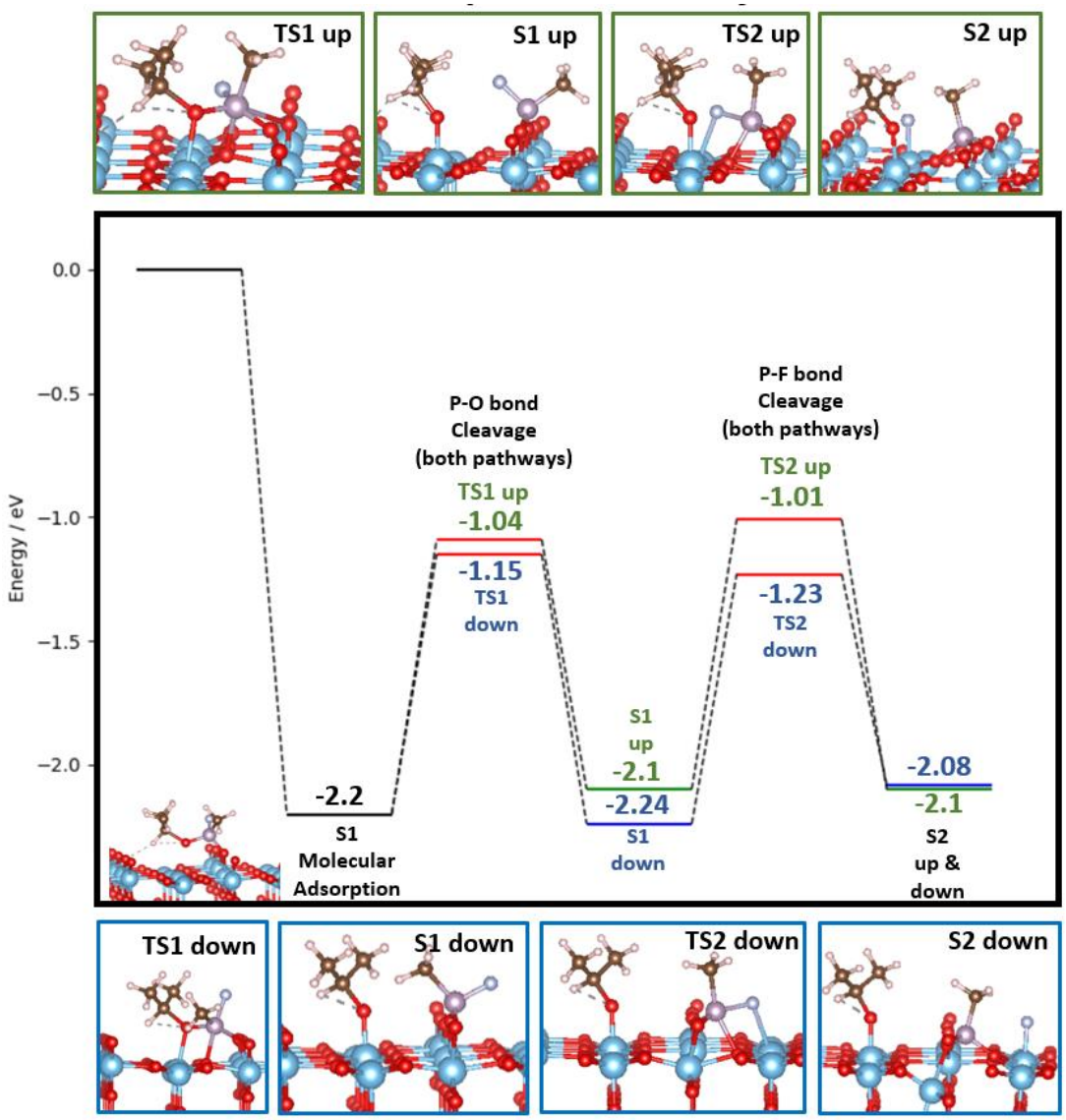

Figure 41 Decomposition pathway of Sarin on defective TiO_2(110) initiated via P-O_{alko} bond cleavage.

Finally, we also tried to see the possibility to cleave the P-F bond from molecularly adsorbed sarin namely geometry defect B (fig. 29). We have tried to bring fluorine closer to Ti_{5c} prior to optimization, with a result of fluorine actually moving away from the surface post-optimization. At this point, a pathway seems to be difficult, though not impossible. We performed a small thermodynamic analysis and found that the intermediate after P-F bond cleavage with phosphor center re-establishing tetrahedral coordination with neighboring bridging oxygen is more stable by a whopping 0.79 eV, in comparison to P-O_{alko} bond cleavage which only brings down the energy of the system by only 0.04 eV. This is particularly interesting as DMMP lacks the fluorine bond (replaced with methoxy instead), and thus may not be able to simulate this part of sarin chemistry very well.

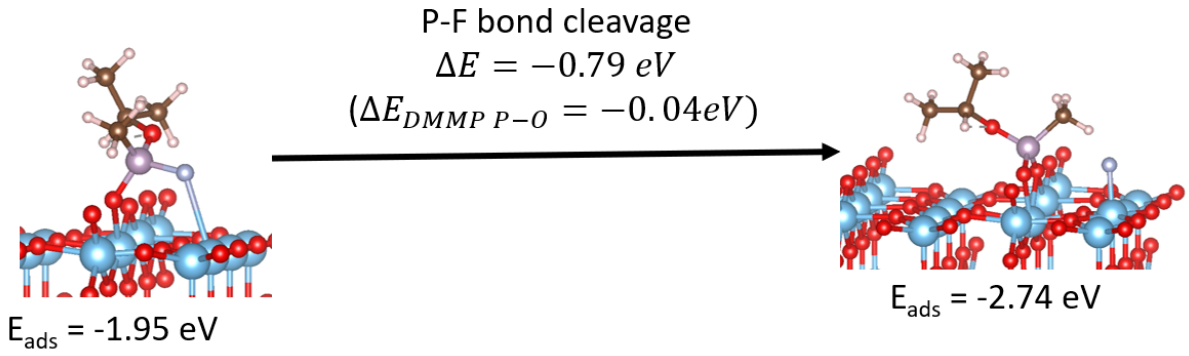

Figure 42 Thermodynamic analysis of P-F bond cleavage of Sarin on the defective surface.

If we compare the feasibility of P-F bond cleavage of sarin on both pristine and defective surfaces, there has been a tendency for P-F bond cleavage to have a lower barrier, and additionally resulting in more stable intermediates in comparison to P-O_{alko} bond cleavage. Meanwhile, DMMP only qualitatively resembles the chemistry of P-O_{alko} bond cleavage as it lacks any cyanide group.

3.3.4. Conclusion

On the pristine surface, screening of sarin adsorption modes on r-TiO2(110) yields two structures that closely resemble DMMP's best adsorption mode. Sarin interacts via its oxo constituent (P=O) and surface Ti_{5c} with additional interaction either from its fluoride or alkoxy group with neighboring surface Ti_{5c}. P-F and P-O_{alko} bond cleavage both have high barriers with the P-F bond being slightly lower. O-C bond cleavage is still the kinetically accessible pathway.

On the defective surface, most stable sarin adsorption is still analogous to DMMP's chemistry; sarin adsorbing via oxo substituent (P=O) filling in the oxygen vacancy site with the alkoxy substituent (O-i-Pr) interacting with nearby Ti_{5c}. Interestingly, fluorine does not prefer to interact with surface Ti_{5c}. Decomposition via P-O_{alko} bond cleavage in the case of sarin is almost identical to the case of DMMP.P-F bond cleavage to have a slightly lower barrier in comparison to both P-O_{alko} bond cleavage. Lastly, despite fluorine not preferring to interact with surface Ti_{5c}, thermodynamic analysis shows that P-F bond cleavage yield to dramatically more stable intermediate. This indicates a slight difference between the chemistry of DMMP and sarin. To conclude, we found that DMMP and sarin resemble similar adsorption and decomposition characteristic when it is initialized via P-O_{alko} or O-C bond cleavage. P-F bond cleavage may yield interesting chemistry of sarin that is of interest for future studies.

4. Final Conclusions & Closing Remarks

This thesis aims to elucidate the reason behind the different reactivity of DMMP across different metal oxides. In part one, DFT, XPS, and STM were used to elucidate three decomposition pathways of DMMP on hematite supported iron oxide thin films (Fe_3O_4(111)/Fe_2O_3(0001)). We discovered the vital role of the mobility of Lewis basic oxygen from the interface between bulk Fe_2O_3(0001) and surface Fe_3O_4(111) film toward the surface, to help to stabilize the remaining phosphorus-containing intermediates during decomposition. This process initiates the formation of dimethyl ether (DME) that is unique to the case of iron oxide. Other gas phase products: methanol and formaldehyde, are resulting from the activation of surface methoxy species coming from the P-O bond cleavage of DMMP.

In part two, we elucidate the pathways, reaction barriers, and kinetics of the DMMP decomposition on pristine and defective r-TiO_2 (110). In contrast to Fe_3O_4(111), TPD measurements showed that no DME is being produced, with only the formation of small amounts of methanol and formaldehyde. Compared to iron oxide, the reactivity of DMMP on TiO_2(110) is low, although titania serves as an excellent surface to trap both molecular DMMP and its decomposition products. Dissociation on the pristine surface is initiated via O-CH_3 bond cleavage, though kinetically feasible at high temperatures only. Oxygen vacancies help lower the barrier of the P-OCH_3 bond cleavage and may serve as active sites.

Lastly, in part 3, we investigate selected decomposition pathways of sarin on r-TiO_2(110) to probe the appropriateness of DMMP as its simulant. On pristine and defective surfaces, we found that sarin behaves almost identical to DMMP, exhibiting high barrier to cleave both P-F and P-O_{alko} bonds. However, calculations show that the P-F bond is somewhat weaker and easier to break in comparison to the P-O_{alko} bond. Thermodynamic studies of P-F bond cleavage show that the intermediate is greatly stabilized upon transfer of F towards surface Ti. This is an indication that sarin decomposition may be more facile than DMMP due to the different bond strength between P-O and P-F bond. Despite this minor difference, we conclude that DMMP is an adequate simulant as its major decomposition pathways qualitatively exhibit similar features as sarin.

Theoretical studies can play an important role in helping us understand the underlying process seen in experimental results. Possible future works would be to extend the knowledge we have on the interaction between CWA and metal oxide on the molecular level by start adding catalytic species that can enhance the reactivity of the surface. One of the key goals that can be used as a starting parameter to design such catalytic species is to find a supported catalyst that can stabilize active surface oxygen to help lower the high bond activation barrier for oxidative decomposition. For example, the utilization of nanoparticles or single-atom catalysts added on metal oxides is an exciting solution that should be considered. Sub-nanoparticle metals are known to undergo rearrangements under gas exposure, which may form interesting peroxo-states that are reactive for decomposition. Theoretical studies may be used to overcome the challenge to characterize such nanoparticle stability reactive conditions.[5] Additionally, such dopants should be considered together with defects as well as these have been shown to present important impacts on the stability of chemisorbed DMMP. As a final remark, theoretical studies may give experimentalist guidance on what to look for when designing a combination of good dopant and metal oxide.

5. Bibliography

(1) Smithson, a. E. A.; Levy, L. Rethinking the Lessons of Tokyo. *Ataxia Chem. Biol. Terror. Threat US response. Washington, DC, Henry L. Stimson Cent.* **2000**.

(2) Okumura, T.; Hisaoka, T.; Yamada, A.; Naito, T.; Isonuma, H.; Okumura, S.; Miura, K.; Sakurada, M.; Maekawa, H.; Ishimatsu, S.; Takasu, N.; Suzuki, K. The Tokyo Subway Sarin Attack - Lessons Learned. In *Toxicology and Applied Pharmacology*; 2005. https://doi.org/10.1016/j.taap.2005.02.032.

(3) Chulov, M. Sarin Used in April Syria Attack, Chemical Weapons Watchdog Confirms. *The Guardian*. 2017.

(4) Tabassis, L. The Convention on the Prohibition of the Development, Production, Stockpiling and Use of Chemical Weapons and on Their Destruction (Chemical Weapons Convention). In *Making Treaties Work: Human Rights, Environment and Arms Control*; 2007. https://doi.org/10.1017/CBO9780511494345.013.

(5) Miyaki, K.; Nishiwaki, Y.; Maekawa, K.; Ogawa, Y.; Asukai, N.; Yoshimura, K.; Etoh, N.; Matsumoto, Y.; Kikuchi, Y.; Kumagai, N.; Omae, K. Effects of Sarin on the Nervous System of Subway Workers Seven Years after the Tokyo Subway Sarin Attack. *J. Occup. Health* **2005**. https://doi.org/10.1539/joh.47.299.

(6) Zappa, D.; Galstyan, V.; Kaur, N.; Munasinghe Arachchige, H. M. M.; Sisman, O.; Comini, E. "Metal Oxide -Based Heterostructures for Gas Sensors"- A Review. *Analytica Chimica Acta*. 2018. https://doi.org/10.1016/j.aca.2018.09.020.

(7) Oh, S. W.; Kim, Y. H.; Yoo, D. J.; Oh, S. M.; Park, S. J. Sensing Behaviour of Semconducting Metal Oxides for the Detection of Organophosphorus Compounds. *Sensors Actuators B. Chem.* **1993**. https://doi.org/10.1016/0925-4005(93)85411-3.

(8) Li, Y. X.; Koper, O.; Atteya, M.; Klabunde, K. J. Adsorption and Decomposition of Organophosphorus Compounds on Nanoscale Metal Oxide Particles. In Situ GC-MS Studies of Pulsed Microreactions over Magnesium Oxide. *Chem. Mater.* **1992**. https://doi.org/10.1021/cm00020a019.

(9) Sharma, N.; Kakkar, R. Recent Advancements on Warfare Agents/Metal Oxides Surface Chemistry and Their Simulation Study. *Adv. Mater. Lett.* **2013**. https://doi.org/10.5185/amlett.2012.12493.

(10) Rusu, C. N.; Yates, J. T. Adsorption and Decomposition of Dimethyl Methylphosphonate on TiO2. *J. Phys. Chem. B* **2000**. https://doi.org/10.1021/jp002560q.

(11) Sheinker, V. N.; Mitchell, M. B. Quantitative Study of the Decomposition of Dimethyl Methylphosphonate (DMMP) on Metal Oxides at Room Temperature and Above. *Chem. Mater.* **2002**. https://doi.org/10.1021/cm010758x.

(12) Paukku, Y.; Michalkova, A.; Leszczynski, J. Adsorption of Dimethyl Methylphosphonate and Trimethyl Phosphate on Calcium Oxide: An Ab Initio Study. *Struct. Chem.* **2008**. https://doi.org/10.1007/s11224-008-9287-x.

(13) Walenta, C. A.; Xu, F.; Tesvara, C.; O'Connor, C. R.; Sautet, P.; Friend, C. M. Facile

Decomposition of Organophosphonates by Dual Lewis Sites on a Fe3O4(111) Film. *J. Phys. Chem. C* **2020**. https://doi.org/10.1021/acs.jpcc.0c01708.

(14) Zappa, D.; Bertuna, A.; Comini, E.; Kaur, N.; Poli, N.; Sberveglieri, V.; Sberveglieri, G. Metal Oxide Nanostructures: Preparation, Characterization and Functional Applications as Chemical Sensors. *Beilstein J. Nanotechnol.* **2017**. https://doi.org/10.3762/bjnano.8.122.

(15) Kim, H. J.; Lee, J. H. Highly Sensitive and Selective Gas Sensors Using P-Type Oxide Semiconductors: Overview. *Sensors and Actuators, B: Chemical*. 2014. https://doi.org/10.1016/j.snb.2013.11.005.

(16) Tomchenko, A. A.; Harmer, G. P.; Marquis, B. T. Detection of Chemical Warfare Agents Using Nanostructured Metal Oxide Sensors. *Sensors Actuators B Chem.* **2005**, *108* (1–2), 41–55. https://doi.org/10.1016/j.snb.2004.11.059.

(17) Szinicz, L. History of Chemical and Biological Warfare Agents. *Toxicology* **2005**. https://doi.org/10.1016/j.tox.2005.06.011.

(18) Moyer, R. A.; Sidell, F. R.; Salem, H. Nerve Agents. In *Encyclopedia of Toxicology: Third Edition*; 2014. https://doi.org/10.1016/B978-0-12-386454-3.00635-7.

(19) Sanderson, H. Chemical Warfare Agents. In *Encyclopedia of Environmental Health*; Elsevier, 2011; pp 587–596. https://doi.org/10.1016/B978-0-444-52272-6.00386-X.

(20) Ganesan, K.; Raza, S. K.; Vijayaraghavan, R. Chemical Warfare Agents. *J. Pharm. Bioallied Sci.* **2010**, *2* (3), 166–178. https://doi.org/10.4103/0975-7406.68498.

(21) Newmark, J. Nerve Agents. *Neurologist*. 2007. https://doi.org/10.1097/01.nrl.0000252923.04894.53.

(22) Chauhan, S.; Chauhan, S.; D'Cruz, R.; Faruqi, S.; Singh, K. K.; Varma, S.; Singh, M.; Karthik, V. Chemical Warfare Agents. *Environmental Toxicology and Pharmacology*. 2008. https://doi.org/10.1016/j.etap.2008.03.003.

(23) Kaushik, M.; Hanmaiahgari, P. R. The United Nations. In *SpringerBriefs in Applied Sciences and Technology*; 2017. https://doi.org/10.1007/978-981-10-2377-4_6.

(24) Holstege, C. P.; Kirk, M.; Sidell, F. R. Chemical Warfare: Nerve Agent Poisoning. *Crit. Care Clin.* **1997**. https://doi.org/10.1016/S0749-0704(05)70374-2.

(25) Walenta, C. A.; Xu, F.; Tesvara, C.; O'Connor, C. R.; Sautet, P.; Friend, C. M. Facile Decomposition of Organophosphonates by Dual Lewis Sites on a Fe 3 O 4 (111) Film . *J. Phys. Chem. C* **2020**. https://doi.org/10.1021/acs.jpcc.0c01708.

(26) Lukey, B. J.; Romano, J. A.; Harry, S.; Salem, H.; Ternay Jr., A. L.; Smart, J. K. Brief History and Use of Chemical Warfare Agents in Warfare and Terrorism. In *Chemical Warfare Agents*; 2019. https://doi.org/10.1201/9781498769235-1.

(27) Watson, A.; Opresko, D.; Young, R. A.; Hauschild, V.; King, J.; Bakshi, K. Organophosphate Nerve Agents. In *Handbook of Toxicology of Chemical Warfare Agents: Second Edition*; 2015. https://doi.org/10.1016/B978-0-12-800159-2.00009-9.

(28) Wiener, S. W.; Hoffman, R. S. Nerve Agents: A Comprehensive Review. *Journal of*

Intensive Care Medicine. 2004. https://doi.org/10.1177/0885066603258659.

(29) Moyer, R. A.; Salem, H. V-Series Nerve Agents: Other than VX. In *Encyclopedia of Toxicology: Third Edition*; 2014. https://doi.org/10.1016/B978-0-12-386454-3.00668-0.

(30) King, A. M.; Aaron, C. K. Organophosphate and Carbamate Poisoning. *Emergency Medicine Clinics of North America*. 2015. https://doi.org/10.1016/j.emc.2014.09.010.

(31) Bajgar, J. Organophosphates{plus 45 Degree Rule}Nerve Agent Poisoning: Mechanism of Action, Diagnosis, Prophylaxis, And Treatment. *Adv. Clin. Chem.* **2004**. https://doi.org/10.1016/S0065-2423(04)38006-6.

(32) National Institute for Occupational Safety and Health. *Pocket Guide to Chemical Hazards*; 2007.

(33) Decker, J. A.; Rogers, H. W. Revised Airborne Exposure Limits for Chemical Warfare Agents. *NATO Secur. through Sci. Ser. C Environ. Secur.* **2006**. https://doi.org/10.1007/1-4020-3137-8_31.

(34) Quintero, Y. C.; Nagarajan, R. Molecular and Dissociative Adsorption of DMMP, Sarin and Soman on Dry and Wet TiO2(110) Using Density Functional Theory. *Surf. Sci.* **2018**. https://doi.org/10.1016/j.susc.2018.04.002.

(35) Trubitsyn, D. A.; Vorontsov, A. V. Experimental Study of Dimethyl Methylphosphonate Decomposition over Anatase TiO 2. *J. Phys. Chem. B* **2005**, *109* (46), 21884–21892. https://doi.org/10.1021/jp053793q.

(36) Agrawal, M.; Sava Gallis, D. F.; Greathouse, J. A.; Sholl, D. S. How Useful Are Common Simulants of Chemical Warfare Agents at Predicting Adsorption Behavior? *J. Phys. Chem. C* **2018**. https://doi.org/10.1021/acs.jpcc.8b08856.

(37) Xiang, H. F.; Xu, H. Y.; Wang, Z. Z.; Chen, C. H. Dimethyl Methylphosphonate (DMMP) as an Efficient Flame Retardant Additive for the Lithium-Ion Battery Electrolytes. *J. Power Sources* **2007**. https://doi.org/10.1016/j.jpowsour.2007.05.001.

(38) Maloney, K. M.; Chung, J. Y. L. A General Procedure for the Preparation of β-Ketophosphonates. *J. Org. Chem.* **2009**. https://doi.org/10.1021/jo901552k.

(39) Talmage, S.; Watson, A.; Hauschild, V.; Munro, N.; King, J. Chemical Warfare Agent Degradation and Decontamination. *Curr. Org. Chem.* **2007**. https://doi.org/10.2174/138527207779940892.

(40) Jang, Y. J.; Kim, K.; Tsay, O. G.; Atwood, D. A.; Churchill, D. G. Update 1 of: Destruction and Detection of Chemical Warfare Agents. *Chemical Reviews*. 2015. https://doi.org/10.1021/acs.chemrev.5b00402.

(41) Gupta, R. C. *Handbook of Toxicology of Chemical Warfare Agents*; Elsevier, 2015. https://doi.org/10.1016/C2013-0-15402-5.

(42) Munro, N. B.; Talmage, S. S.; Griffin, G. D.; Waters, L. C.; Watson, A. P.; King, J. F.; Hauschild, V. The Sources, Fate, and Toxicity of Chemical Warfare Agent Degradation Products. *Environmental Health Perspectives*. 1999.

https://doi.org/10.1289/ehp.99107933.

(43) Small, M. J. Compounds Formed from the Chemical Decontamination of HD, GB, VX and Their Environmental Fate. In *Technical Report*; 1984.

(44) Rosenblatt, D. H.; Small, M. J.; Kimmell, T. A.; Anderson, A. W. *Background Chemistry for Chemical Warfare Agents and Decontamination Processes in Support of Delisting Waste Streams at the U.S. Army Dugway Proving Ground, Utah*; 1996.

(45) Epstein, J.; Rosenblatt, D. H. Kinetics of Some Metal Ion-Catalyzed Hydrolyses of Isopropyl Methylphosphonofluoridate (GB) at 25°. *J. Am. Chem. Soc.* **1958**, *80* (14), 3596–3598. https://doi.org/10.1021/ja01547a027.

(46) Epstein, J.; Demek, M. M. Detection and Estimation of Organophosphorus Compounds with Hydroxamic Acids Using a Chemical Analog of the Cholinesterase Inhibition Method. *Anal. Chem.* **1967**. https://doi.org/10.1021/ac60254a039.

(47) Rosenblatt, D. H.; Miller, T. A.; Dacre, J. C.; Muul, I.; Cogley, D. R. *Problem Definition Studies on Potential Environmental Pollutants II: Physical, Chemical, Toxicological, and Biological Properties of 16 Substances.*; 1975.

(48) Dey, A. Semiconductor Metal Oxide Gas Sensors: A Review. *Materials Science and Engineering B: Solid-State Materials for Advanced Technology*. 2018. https://doi.org/10.1016/j.mseb.2017.12.036.

(49) Kim, C. S.; Lad, R. J.; Tripp, C. P. Interaction of Organophosphorous Compounds with TiO2 and WO3 Surfaces Probed by Vibrational Spectroscopy. *Sensors Actuators B Chem.* **2001**, *76* (1–3), 442–448. https://doi.org/10.1016/S0925-4005(01)00653-0.

(50) Chen, D. A.; Ratliff, J. S.; Hu, X.; Gordon, W. O.; Senanayake, S. D.; Mullins, D. R. Dimethyl Methylphosphonate Decomposition on Fully Oxidized and Partially Reduced Ceria Thin Films. *Surf. Sci.* **2010**, *604* (5–6), 574–587. https://doi.org/10.1016/j.susc.2009.12.028.

(51) Ratliff, J. S.; Tenney, S. A.; Hu, X.; Conner, S. F.; Ma, S.; Chen, D. A. Decomposition of Dimethyl Methylphosphonate on Pt, Au, and Au-Pt Clusters Supported on TiO 2 (110). *Langmuir* **2009**. https://doi.org/10.1021/la802361q.

(52) Ma, S.; Zhou, J.; Kang, Y. C.; Reddic, J. E.; Chen, D. A. Dimethyl Methylphosphonate Decomposition on Cu Surfaces: Supported Cu Nanoclusters and Films on TiO 2(110). *Langmuir* **2004**. https://doi.org/10.1021/la048594x.

(53) Trotochaud, L.; Head, A. R.; Tsyshevsky, R.; Pletincx, S.; Yu, Y.; Karslioglu, O.; Eichhorn, B. W.; Kuklja, M. M.; Bluhm, H. Adsorption and Decomposition of a Chemical Warfare Agent Simulant on Copper and Molybdenum Oxides. In *Abstracts of Papers, 253rd ACS National Meeting & Exposition, San Francisco, CA, United States, April 2-6, 2017*; 2017.

(54) Mitchell, M. B.; Sheinker, V. N.; Mintz, E. A. Adsorption and Decomposition of Dimethyl Methylphosphonate on Metal Oxides. *J. Phys. Chem. B* **1997**. https://doi.org/10.1021/jp972724b.

(55) Mitchell, M. B.; Sheinker, V. N.; Tesfamichael, A. B.; Gatimu, E. N.; Nunley, M. Decomposition of Dimethyl Methylphosphonate (DMMP) on Supported Cerium and Iron Co-Impregnated Oxides at Room Temperature. *J. Phys. Chem. B* **2003**. https://doi.org/10.1021/jp021836m.

(56) Mitchell, M. B.; Sheinker, V. N.; Cox, W. W. Room Temperature Reaction of Ozone and Dimethyl Methylphosphonate (DMMP) on Alumina-Supported Iron Oxide. *J. Phys. Chem. C* **2007**. https://doi.org/10.1021/jp066533x.

(57) Henderson, M. A.; Jin, T.; White, J. M. A TPD/AES Study of the Interaction of Dimethyl Methylphosphonate with Iron Oxide (.Alpha.-Fe2O3) and Silicon Dioxide. *J. Phys. Chem.* **1986**, *90* (19), 4607–4611. https://doi.org/10.1021/j100410a027.

(58) Trotochaud, L.; Head, A. R.; Büchner, C.; Yu, Y.; Karslıoğlu, O.; Tsyshevsky, R.; Holdren, S.; Eichhorn, B.; Kuklja, M. M.; Bluhm, H. Room Temperature Decomposition of Dimethyl Methylphosphonate on Cuprous Oxide Yields Atomic Phosphorus. *Surf. Sci.* **2019**. https://doi.org/10.1016/j.susc.2018.10.003.

(59) Segal, S. R.; Cao, L.; Suib, S. L.; Tang, X.; Satyapal, S. Thermal Decomposition of Dimethyl Methylphosphonate over Manganese Oxide Catalysts. *J. Catal.* **2001**, *198* (1), 66–76. https://doi.org/10.1006/jcat.2000.3126.

(60) Tang, X.; Hicks, Z.; Wang, L.; Ganteför, G.; Bowen, K. H.; Tsyshevsky, R.; Sun, J.; Kuklja, M. M. Adsorption and Decomposition of Dimethyl Methylphosphonate on Size-Selected (MoO 3) 3 Clusters. *Phys. Chem. Chem. Phys.* **2018**, *20* (7), 4840–4850. https://doi.org/10.1039/C7CP08427G.

(61) Holdren, S.; Tsyshevsky, R.; Fears, K.; Owrutsky, J.; Wu, T.; Wang, X.; Eichhorn, B. W.; Kuklja, M. M.; Zachariah, M. R. Adsorption and Destruction of the G-Series Nerve Agent Simulant Dimethyl Methylphosphonate on Zinc Oxide. *ACS Catal.* **2019**, *9* (2), 902–911. https://doi.org/10.1021/acscatal.8b02999.

(62) Mitchell, M. B.; Sheinker, V. N.; Mintz, E. A. Adsorption and Decomposition of Dimethyl Methylphosphonate on Metal Oxides. *J. Phys. Chem. B* **1997**, *101* (51), 11192–11203. https://doi.org/10.1021/jp972724b.

(63) Fan, G.; Wang, Y.; Hu, M.; Luo, Z.; Zhang, K.; Li, G. Template Free Synthesis of Hollow Ball-like Nano-Fe2O3 and Its Application to the Detection of Dimethyl Methylphosphonate at Room Temperature. *Sensors* **2012**. https://doi.org/10.3390/s120404594.

(64) Zhu, Y.; Cheng, Z.; Xiang, Q.; Chen, X.; Xu, J. Synthesis of Functionalized Mesoporous TiO2-SiO2 with Organic Fluoroalcohol as High Performance DMMP Gas Sensor. *Sensors Actuators, B Chem.* **2017**. https://doi.org/10.1016/j.snb.2016.10.080.

(65) Templeton, M. K.; Weinberg, W. H. Adsorption and Decomposition of Dimethyl Methylphosphonate on an Aluminum Oxide Surface. *J. Am. Chem. Soc.* **1985**. https://doi.org/10.1021/ja00287a018.

(66) Pehrsson, P.; Gordon, W.; Balow, R.; Barlow, D.; Bermudez, V. M.; Iordanov, I.; Knox, C.; Lundin, J.; Wynne, J. H.; Karwacki, C. J.; Peterson, G. W. DMMP Reactivity on

Zirconium Hydroxide under in Operando Conditions. In *Abstracts of Papers, 251st ACS National Meeting & Exposition, San Diego, CA, United States, March 13-17, 2016*; 2016.

(67) Wang, G.; Sharp, C.; Plonka, A. M.; Wang, Q.; Frenkel, A. I.; Guo, W.; Hill, C.; Smith, C.; Kollar, J.; Troya, D.; Morris, J. R. Mechanism and Kinetics for Reaction of the Chemical Warfare Agent Simulant, DMMP(g), with Zirconium(IV) MOFs: An Ultrahigh-Vacuum and DFT Study. *J. Phys. Chem. C* **2017**. https://doi.org/10.1021/acs.jpcc.7b00070.

(68) Ruffley, J. P.; Goodenough, I.; Luo, T. Y.; Richard, M.; Borguet, E.; Rosi, N. L.; Johnson, J. K. Design, Synthesis, and Characterization of Metal-Organic Frameworks for Enhanced Sorption of Chemical Warfare Agent Simulants. *J. Phys. Chem. C* **2019**. https://doi.org/10.1021/acs.jpcc.9b05574.

(69) Plonka, A. M.; Wang, Q.; Gordon, W. O.; Balboa, A.; Troya, D.; Guo, W.; Sharp, C. H.; Senanayake, S. D.; Morris, J. R.; Hill, C. L.; Frenkel, A. I. In Situ Probes of Capture and Decomposition of Chemical Warfare Agent Simulants by Zr-Based Metal Organic Frameworks. *J. Am. Chem. Soc.* **2017**, *139* (2), 599–602. https://doi.org/10.1021/jacs.6b11373.

(70) Head, A. R.; Tsyshevsky, R.; Trotochaud, L.; Yu, Y.; Kyhl, L.; Karslıoğlu, O.; Kuklja, M. M.; Bluhm, H. Adsorption of Dimethyl Methylphosphonate on MoO 3 : The Role of Oxygen Vacancies. *J. Phys. Chem. C* **2016**, *120* (51), 29077–29088. https://doi.org/10.1021/acs.jpcc.6b07340.

(71) Hong, R. Y.; Feng, B.; Chen, L. L.; Liu, G. H.; Li, H. Z.; Zheng, Y.; Wei, D. G. Synthesis, Characterization and MRI Application of Dextran-Coated Fe3O4 Magnetic Nanoparticles. *Biochem. Eng. J.* **2008**. https://doi.org/10.1016/j.bej.2008.07.009.

(72) Cheng, F. Y.; Su, C. H.; Yang, Y. S.; Yeh, C. S.; Tsai, C. Y.; Wu, C. L.; Wu, M. T.; Shieh, D. Bin. Characterization of Aqueous Dispersions of Fe3O4 Nanoparticles and Their Biomedical Applications. *Biomaterials* **2005**. https://doi.org/10.1016/j.biomaterials.2004.03.016.

(73) Xu, C.; Sun, S. New Forms of Superparamagnetic Nanoparticles for Biomedical Applications. *Advanced Drug Delivery Reviews*. 2013. https://doi.org/10.1016/j.addr.2012.10.008.

(74) Pour, A. N.; Housaindokht, M. R.; Tayyari, S. F.; Zarkesh, J. Fischer-Tropsch Synthesis by Nano-Structured Iron Catalyst. *J. Nat. Gas Chem.* **2010**. https://doi.org/10.1016/S1003-9953(09)60059-1.

(75) Dictor, R. A.; Bell, A. T. Fischer-Tropsch Synthesis over Reduced and Unreduced Iron Oxide Catalysts. *J. Catal.* **1986**. https://doi.org/10.1016/0021-9517(86)90043-6.

(76) Weiss, W.; Ranke, W. Surface Chemistry and Catalysis on Well-Defined Epitaxial Iron-Oxide Layers. *Progress in Surface Science*. 2002. https://doi.org/10.1016/S0079-6816(01)00056-9.

(77) Resasco, D. E. Dehydrogenation by Heterogeneous Catalysts. *Encycl. Catal.* **2002**.

(78) Lee, E. H. Iron Oxide Catalysts for Dehydrogenation of Ethylbenzene in the Presence of

Steam. *Catal. Rev.* **1974**. https://doi.org/10.1080/01614947408071864.

(79) Goergen, S.; Yin, C.; Yang, M.; Lee, B.; Lee, S.; Wang, C.; Wu, P.; Boucher, M. B.; Kwon, G.; Seifert, S.; Winans, R. E.; Vajda, S.; Flytzani-Stephanopoulos, M. Structure Sensitivity of Oxidative Dehydrogenation of Cyclohexane over FeOx and Au/Fe3O4 Nanocrystals. *ACS Catal.* **2013**. https://doi.org/10.1021/cs3007582.

(80) Tauster, S. J.; Fung, S. C.; Baker, R. T. K.; Horsley, J. A. Strong Interactions in Supported-Metal Catalysts. *Science (80-.).* **1981**. https://doi.org/10.1126/science.211.4487.1121.

(81) Yang, X.-F.; Wang, A.; Qiao, B.; Li, J.; Liu, J.; Zhang, T. Single-Atom Catalysts: A New Frontier in Heterogeneous Catalysis. *Acc. Chem. Res.* **2013**, *46* (8), 1740–1748. https://doi.org/10.1021/ar300361m.

(82) Wei, H.; Liu, X.; Wang, A.; Zhang, L.; Qiao, B.; Yang, X.; Huang, Y.; Miao, S.; Liu, J.; Zhang, T. FeOx-Supported Platinum Single-Atom and Pseudo-Single-Atom Catalysts for Chemoselective Hydrogenation of Functionalized Nitroarenes. *Nat. Commun.* **2014**, *5* (1), 5634. https://doi.org/10.1038/ncomms6634.

(83) Qiao, B.; Wang, A.; Yang, X.; Allard, L. F.; Jiang, Z.; Cui, Y.; Liu, J.; Li, J.; Zhang, T. Single-Atom Catalysis of CO Oxidation Using Pt1/FeOx. *Nat. Chem.* **2011**. https://doi.org/10.1038/nchem.1095.

(84) Parkinson, G. S. Iron Oxide Surfaces. *Surface Science Reports*. 2016. https://doi.org/10.1016/j.surfrep.2016.02.001.

(85) Goering, E.; Gold, S.; Lafkioti, M.; Schütz, G. Vanishing Fe 3d Orbital Moments in Single-Crystalline Magnetite. *Europhys. Lett.* **2006**. https://doi.org/10.1209/epl/i2005-10359-8.

(86) Kiejna, A.; Ossowski, T.; Pabisiak, T. Surface Properties of the Clean and Au / Pd Covered Fe 3 O 4 (111): DFT and DFT + U Study. **2012**, *125414* (December 2011), 1–11. https://doi.org/10.1103/PhysRevB.85.125414.

(87) Grau-Crespo, R.; Al-Baitai, A. Y.; Saadoune, I.; De Leeuw, N. H. Vacancy Ordering and Electronic Structure of γ-Fe2O 3 (Maghemite): A Theoretical Investigation. *J. Phys. Condens. Matter* **2010**. https://doi.org/10.1088/0953-8984/22/25/255401.

(88) Yang, T.; Wen, X. D.; Ren, J.; Li, Y. W.; Wang, J. G.; Huo, C. F. Surface Structures of Fe3O4 (111), (110), and (001)-A Density Functional Theory Study. *Ranliao Huaxue Xuebao/Journal Fuel Chem. Technol.* **2010**. https://doi.org/10.1016/s1872-5813(10)60024-2.

(89) Noh, J.; Osman, O. I.; Aziz, S. G.; Winget, P.; Brédas, J. L. A Density Functional Theory Investigation of the Electronic Structure and Spin Moments of Magnetite. *Sci. Technol. Adv. Mater.* **2014**. https://doi.org/10.1088/1468-6996/15/4/044202.

(90) Yu, X.; Huo, C. F.; Li, Y. W.; Wang, J.; Jiao, H. Fe 3O 4 Surface Electronic Structures and Stability from GGA + U. *Surf. Sci.* **2012**. https://doi.org/10.1016/j.susc.2012.02.003.

(91) Lemire, C.; Meyer, R.; Henrich, V. E.; Shaikhutinov, S.; Freund, H. J. The Surface

Structure of Fe3O4(111) Films as Studied by CO Adsorption. *Surf. Sci.* **2004**. https://doi.org/10.1016/j.susc.2004.08.033.

(92) Ritter, M.; Weiss, W. Fe3O4(111) Surface Structure Determined by LEED Crystallography. *Surf. Sci.* **1999**. https://doi.org/10.1016/S0039-6028(99)00518-X.

(93) Shaikhutdinov, S. K.; Ritter, M.; Wang, X. G.; Over, H.; Weiss, W. Defect Structures on Epitaxial Fe3O4(111) Films. *Phys. Rev. B - Condens. Matter Mater. Phys.* **1999**. https://doi.org/10.1103/PhysRevB.60.11062.

(94) Barbieri, A.; Weiss, W.; Van Hove, M. A.; Somorjai, G. A. Magnetite Fe3O4(111): Surface Structure by LEED Crystallography and Energetics. *Surf. Sci.* **1994**. https://doi.org/10.1016/0039-6028(94)90832-X.

(95) Roddatis, V. V.; Su, D. S.; Kuhrs, C.; Ranke, W.; Schlögl, R. Transmission Electron Microscopy Investigation of Fe3O4 Films Grown on (111) Pt Substrates. *Thin Solid Films* **2001**. https://doi.org/10.1016/S0040-6090(01)01240-8.

(96) Santos-Carballal, D.; Roldan, A.; Grau-Crespo, R.; de Leeuw, N. H. A DFT Study of the Structures, Stabilities and Redox Behaviour of the Major Surfaces of Magnetite Fe3O4. *Phys. Chem. Chem. Phys.* **2014**. https://doi.org/10.1039/c4cp00529e.

(97) Monti, M.; Santos, B.; Mascaraque, A.; Rodríguez De La Fuente, O.; Niño, M. A.; Menteş, T. O.; Locatelli, A.; McCarty, K. F.; Marco, J. F.; De La Figuera, J. Magnetism in Nanometer-Thick Magnetite. *Phys. Rev. B - Condens. Matter Mater. Phys.* **2012**. https://doi.org/10.1103/PhysRevB.85.020404.

(98) Grillo, M. E.; Finnis, M. W.; Ranke, W. Surface Structure and Water Adsorption on Fe3 O4 (111): Spin-Density Functional Theory and on-Site Coulomb Interactions. *Phys. Rev. B - Condens. Matter Mater. Phys.* **2008**. https://doi.org/10.1103/PhysRevB.77.075407.

(99) Ahdjoudj, J.; Martinsky, C.; Minot, C.; Van Hove, M. A.; Somorjai, G. A. Theoretical Study of the Termination of the Fe3O4 (111) Surface. *Surf. Sci.* **1999**. https://doi.org/10.1016/S0039-6028(99)01008-0.

(100) Noh, J.; Osman, O. I.; Aziz, S. G.; Winget, P.; Bre, J. Magnetite Fe 3 O 4 (111) Surfaces : Impact of Defects on Structure , Stability , and Electronic Properties. **2015**, *4* (111). https://doi.org/10.1021/acs.chemmater.5b02885.

(101) Liang, M.; Fan, K.; Pan, Y.; Jiang, H.; Wang, F.; Yang, D.; Lu, D.; Feng, J.; Zhao, J.; Yang, L.; Yan, X. Fe3O4 Magnetic Nanoparticle Peroxidase Mimetic-Based Colorimetric Assay for the Rapid Detection of Organophosphorus Pesticide and Nerve Agent. *Anal. Chem.* **2013**. https://doi.org/10.1021/ac302781r.

(102) Zhang, X.; Wang, H.; Yang, C.; Du, D.; Lin, Y. Preparation, Characterization of Fe3O4 at TiO2 Magnetic Nanoparticles and Their Application for Immunoassay of Biomarker of Exposure to Organophosphorus Pesticides. *Biosens. Bioelectron.* **2013**. https://doi.org/10.1016/j.bios.2012.09.047.

(103) Chen, R.; Tao, C. A.; Zhang, Z.; Chen, X.; Liu, Z.; Wang, J. Layer-by-Layer Fabrication of Core-Shell Fe3O4@UiO-66-NH2 with High Catalytic Reactivity toward the Hydrolysis of Chemical Warfare Agent Simulants. *ACS Appl. Mater. Interfaces* **2019**.

https://doi.org/10.1021/acsami.9b14099.

(104) YIN, L. L.; KONG, X. Y.; ZHANG, Y.; JI, Y. Q. Facile Synthesis of the Magnetic Metal Organic Framework Fe3O4@UiO-66-NH2 for Separation of Strontium. *Biomedical and Environmental Sciences*. 2018. https://doi.org/10.3967/bes2018.065.

(105) Carlucci, C.; Degennaro, L.; Luisi, R. Titanium Dioxide as a Catalyst in Biodiesel Production. *Catalysts*. 2019. https://doi.org/10.3390/catal9010075.

(106) Miyoshi, A.; Nishioka, S.; Maeda, K. Water Splitting on Rutile TiO2-Based Photocatalysts. *Chemistry - A European Journal*. 2018. https://doi.org/10.1002/chem.201800799.

(107) Kavan, L.; Grätzel, M.; Gilbert, S. E.; Klemenz, C.; Scheel, H. J. Electrochemical and Photoelectrochemical Investigation of Single-Crystal Anatase. *J. Am. Chem. Soc.* **1996**. https://doi.org/10.1021/ja954172l.

(108) Zhang, J.; Zhou, P.; Liu, J.; Yu, J. New Understanding of the Difference of Photocatalytic Activity among Anatase, Rutile and Brookite TiO2. *Phys. Chem. Chem. Phys.* **2014**. https://doi.org/10.1039/c4cp02201g.

(109) Anpo, M.; Yamashita, H.; Ichihashi, Y.; Ehara, S. Photocatalytic Reduction of CO2 with H2O on Various Titanium Oxide Catalysts. *J. Electroanal. Chem.* **1995**. https://doi.org/10.1016/0022-0728(95)04141-A.

(110) Obee, T. N.; Satyapal, S. Photocatalytic Decomposition of DMMP on Titania. *J. Photochem. Photobiol. A Chem.* **1998**. https://doi.org/10.1016/S1010-6030(98)00372-4.

(111) Fujishima, A.; Rao, T. N.; Tryk, D. A. Titanium Dioxide Photocatalysis. *J. Photochem. Photobiol. C Photochem. Rev.* **2000**, *1* (1), 1–21. https://doi.org/10.1016/S1389-5567(00)00002-2.

(112) Linsebigler, A. L.; Lu, G.; Yates, J. T. Photocatalysis on TiO2 Surfaces: Principles, Mechanisms, and Selected Results. *Chem. Rev.* **1995**. https://doi.org/10.1021/cr00035a013.

(113) O'Regan, B.; Grätzel, M. A Low-Cost, High-Efficiency Solar Cell Based on Dye-Sensitized Colloidal TiO2 Films. *Nature* **1991**. https://doi.org/10.1038/353737a0.

(114) Chung, I.; Lee, B.; He, J.; Chang, R. P. H.; Kanatzidis, M. G. All-Solid-State Dye-Sensitized Solar Cells with High Efficiency. *Nature* **2012**. https://doi.org/10.1038/nature11067.

(115) Engineering, P.; Wales, N. S. Novel Uses of Titanium Dioxide for Silicon Solar Cells. *Electr. Eng.* **2002**.

(116) Kay, A.; Grätzel, M. Low Cost Photovoltaic Modules Based on Dye Sensitized Nanocrystalline Titanium Dioxide and Carbon Powder. *Sol. Energy Mater. Sol. Cells* **1996**. https://doi.org/10.1016/0927-0248(96)00063-3.

(117) Zhao, H.; Pan, F.; Li, Y. A Review on the Effects of TiO2 Surface Point Defects on CO2 Photoreduction with H2O. *Journal of Materiomics*. 2017.

https://doi.org/10.1016/j.jmat.2016.12.001.

(118) Tang, H.; Su, Y.; Zhang, B.; Lee, A. F.; Isaacs, M. A.; Wilson, K.; Li, L.; Ren, Y.; Huang, J.; Haruta, M.; Qiao, B.; Liu, X.; Jin, C.; Su, D.; Wang, J.; Zhang, T. Classical Strong Metal–Support Interactions between Gold Nanoparticles and Titanium Dioxide. *Sci. Adv.* **2017**. https://doi.org/10.1126/sciadv.1700231.

(119) Çelik, V.; Ünal, H.; Mete, E.; Ellialtıoğlu, Ş. Theoretical Analysis of Small Pt Particles on Rutile <math Display="inline"> <mrow> <msub> <mrow> <mtext>TiO</Mtext> </Mrow> <mn>2</Mn> </Msub> <mrow> <mo>(</Mo> <mrow> <mn>110</Mn> </Mrow> <mo>)</Mo> </Mrow> </Mrow> </Math> Surfaces. *Phys. Rev. B* **2010**, *82* (20), 205113. https://doi.org/10.1103/PhysRevB.82.205113.

(120) Chang, T. Y.; Tanaka, Y.; Ishikawa, R.; Toyoura, K.; Matsunaga, K.; Ikuhara, Y.; Shibata, N. Direct Imaging of Pt Single Atoms Adsorbed on TiO2 (110) Surfaces. *Nano Lett.* **2014**. https://doi.org/10.1021/nl403520c.

(121) Bagheri, S.; Muhd Julkapli, N.; Bee Abd Hamid, S. Titanium Dioxide as a Catalyst Support in Heterogeneous Catalysis. *Scientific World Journal*. 2014. https://doi.org/10.1155/2014/727496.

(122) Helali, Z.; Markovits, A.; Minot, C.; Abderrabba, M. Metal Atom Adsorption on a Defective TiO2-x Support. *Chem. Phys. Lett.* **2014**. https://doi.org/10.1016/j.cplett.2014.01.019.

(123) Cai, Y.; Bai, Z.; Chintalapati, S.; Zeng, Q.; Feng, Y. P. Transition Metal Atoms Pathways on Rutile TiO2 (110) Surface: Distribution of Ti3+ States and Evidence of Enhanced Peripheral Charge Accumulation. *J. Chem. Phys.* **2013**. https://doi.org/10.1063/1.4801025.

(124) Tang, Y.; Asokan, C.; Xu, M.; Graham, G. W.; Pan, X.; Christopher, P.; Li, J.; Sautet, P. Rh Single Atoms on TiO2 Dynamically Respond to Reaction Conditions by Adapting Their Site. *Nat. Commun.* **2019**, *10* (1), 1–18. https://doi.org/10.1038/s41467-019-12461-6.

(125) Han, F.; Kambala, V. S. R.; Srinivasan, M.; Rajarathnam, D.; Naidu, R. Tailored Titanium Dioxide Photocatalysts for the Degradation of Organic Dyes in Wastewater Treatment: A Review. *Applied Catalysis A: General*. 2009. https://doi.org/10.1016/j.apcata.2009.02.043.

(126) Gaya, U. I.; Abdullah, A. H. Heterogeneous Photocatalytic Degradation of Organic Contaminants over Titanium Dioxide: A Review of Fundamentals, Progress and Problems. *Journal of Photochemistry and Photobiology C: Photochemistry Reviews*. 2008. https://doi.org/10.1016/j.jphotochemrev.2007.12.003.

(127) Khaki, M. R. D.; Shafeeyan, M. S.; Raman, A. A. A.; Daud, W. M. A. W. Application of Doped Photocatalysts for Organic Pollutant Degradation - A Review. *Journal of Environmental Management*. 2017. https://doi.org/10.1016/j.jenvman.2017.04.099.

(128) Zhao, J.; Lee, D. T.; Yaga, R. W.; Hall, M. G.; Barton, H. F.; Woodward, I. R.; Oldham, C. J.; Walls, H. J.; Peterson, G. W.; Parsons, G. N. Ultra-Fast Degradation of Chemical Warfare Agents Using MOF–Nanofiber Kebabs. *Angew. Chemie Int. Ed.* **2016**, *55* (42),

13224–13228. https://doi.org/https://doi.org/10.1002/anie.201606656.

(129) Panayotov, D. A.; Morris, J. R. Catalytic Degradation of a Chemical Warfare Agent Simulant: Reaction Mechanisms on TiO2-Supported Au Nanoparticles. *J. Phys. Chem. C* **2008**. https://doi.org/10.1021/jp7118668.

(130) Gupta, S. M.; Tripathi, M. A Review of TiO2 Nanoparticles. *Chinese Sci. Bull.* **2011**, *56* (16), 1639–1657. https://doi.org/10.1007/s11434-011-4476-1.

(131) Braun, J. H.; Baidins, A.; Marganski, R. E. TiO2 Pigment Technology: A Review. *Prog. Org. Coatings* **1992**. https://doi.org/10.1016/0033-0655(92)80001-D.

(132) Bourikas, K.; Kordulis, C.; Lycourghiotis, A. Titanium Dioxide (Anatase and Rutile): Surface Chemistry, Liquid-Solid Interface Chemistry, and Scientific Synthesis of Supported Catalysts. *Chemical Reviews*. 2014. https://doi.org/10.1021/cr300230q.

(133) Vu, N. H.; Le, H. V.; Cao, T. M.; Pham, V. V.; Le, H. M.; Nguyen-Manh, D. Anatase-Rutile Phase Transformation of Titanium Dioxide Bulk Material: A DFT+U Approach. *J. Phys. Condens. Matter* **2012**. https://doi.org/10.1088/0953-8984/24/40/405501.

(134) Wei, X.; Skomski, R.; Balamurugan, B.; Sun, Z. G.; Ducharme, S.; Sellmyer, D. J. Magnetism of TiO and TiO2 Nanoclusters. *J. Appl. Phys.* **2009**. https://doi.org/10.1063/1.3074509.

(135) Diebold, U. The Surface Science of Titanium Dioxide. *Surface Science Reports*. 2003. https://doi.org/10.1016/s0167-5729(02)00100-0.

(136) Diebold, U. Structure and Properties of TiO2 Surfaces: A Brief Review. *Appl. Phys. A Mater. Sci. Process.* **2003**. https://doi.org/10.1007/s00339-002-2004-5.

(137) Kiejna, A.; Pabisiak, T.; Gao, S. W. The Energetics and Structure of Rutile TiO2(110). *J. Phys. Condens. Matter* **2006**. https://doi.org/10.1088/0953-8984/18/17/009.

(138) Pacchioni, G. Oxygen Vacancy: The Invisible Agent on Oxide Surfaces. *ChemPhysChem*. 2003. https://doi.org/10.1002/cphc.200300835.

(139) Wendt, S.; Schaub, R.; Matthiesen, J.; Vestergaard, E. K.; Wahlström, E.; Rasmussen, M. D.; Thostrup, P.; Molina, L. M.; Lægsgaard, E.; Stensgaard, I.; Hammer, B.; Besenbacher, F. Oxygen Vacancies on TiO2(1 1 0) and Their Interaction with H2O and O2: A Combined High-Resolution STM and DFT Study. *Surf. Sci.* **2005**. https://doi.org/10.1016/j.susc.2005.08.041.

(140) Sánchez-Sánchez, C.; González, C.; Jelinek, P.; Méndez, J.; De Andres, P. L.; Martín-Gago, J. A.; López, M. F. Understanding Atomic-Resolved STM Images on TiO2(110)-(1 × 1) Surface by DFT Calculations. *Nanotechnology* **2010**. https://doi.org/10.1088/0957-4484/21/40/405702.

(141) Diebold, U.; Lehman, J.; Mahmoud, T.; Kuhn, M.; Leonardelli, G.; Hebenstreit, W.; Schmid, M.; Varga, P. Intrinsic Defects on a TiO2(110)(1 × 1) Surface and Their Reaction with Oxygen: A Scanning Tunneling Microscopy Study. *Surf. Sci.* **1998**. https://doi.org/10.1016/S0039-6028(98)00356-2.

(142) Dulub, O.; Valentin, C. Di; Selloni, A.; Diebold, U. Structure, Defects, and Impurities at the Rutile TiO2(0 1 1)-(2 × 1) Surface: A Scanning Tunneling Microscopy Study. *Surf. Sci.* **2006**. https://doi.org/10.1016/j.susc.2006.06.042.

(143) Ganduglia-Pirovano, M. V.; Hofmann, A.; Sauer, J. Oxygen Vacancies in Transition Metal and Rare Earth Oxides: Current State of Understanding and Remaining Challenges. *Surface Science Reports*. 2007. https://doi.org/10.1016/j.surfrep.2007.03.002.

(144) Pan, X.; Yang, M.-Q.; Fu, X.; Zhang, N.; Xu, Y.-J. Defective TiO2 with Oxygen Vacancies: Synthesis, Properties and Photocatalytic Applications. *Nanoscale* **2013**, *5* (9), 3601. https://doi.org/10.1039/c3nr00476g.

(145) Wei, H.; Liu, X.; Wang, A.; Zhang, L.; Qiao, B.; Yang, X.; Huang, Y.; Miao, S.; Liu, J.; Zhang, T. FeOx-Supported Platinum Single-Atom and Pseudo-Single-Atom Catalysts for Chemoselective Hydrogenation of Functionalized Nitroarenes. *Nat. Commun.* **2014**, *5* (1), 5634. https://doi.org/10.1038/ncomms6634.

(146) Di Valentin, C.; Pacchioni, G.; Selloni, A. Electronic Structure of Defect States in Hydroxylated and Reduced Rutile TiO2(110) Surfaces. *Phys. Rev. Lett.* **2006**. https://doi.org/10.1103/PhysRevLett.97.166803.

(147) Morgan, B. J.; Watson, G. W. A DFT + U Description of Oxygen Vacancies at the TiO2 Rutile (1 1 0) Surface. *Surf. Sci.* **2007**. https://doi.org/10.1016/j.susc.2007.08.025.

(148) Li, H.; Guo, Y.; Robertson, J. Calculation of TiO2 Surface and Subsurface Oxygen Vacancy by the Screened Exchange Functional. *J. Phys. Chem. C* **2015**. https://doi.org/10.1021/acs.jpcc.5b02430.

(149) Cheng, H.; Selloni, A. Surface and Subsurface Oxygen Vacancies in Anatase TiO2 and Differences with Rutile . *Phys. Rev. B* **2009**. https://doi.org/10.1103/physrevb.79.092101.

(150) Gong, X. Q.; Khorshidi, N.; Stierle, A.; Vonk, V.; Ellinger, C.; Dosch, H.; Cheng, H.; Selloni, A.; He, Y.; Dulub, O.; Diebold, U. The 2 × 1 Reconstruction of the Rutile TiO2(0 1 1) Surface: A Combined Density Functional Theory, X-Ray Diffraction, and Scanning Tunneling Microscopy Study. *Surf. Sci.* **2009**. https://doi.org/10.1016/j.susc.2008.10.034.

(151) Henderson, M. A. Structural Sensitivity in the Dissociation of Water on TiO2 Single-Crystal Surfaces. *Langmuir* **1996**. https://doi.org/10.1021/la960360t.

(152) de Armas, R. S.; Oviedo, J.; San Miguel, M. A.; Sanz, J. F. Methanol Adsorption and Dissociation on TiO 2 (110) from First Principles Calculations. *J. Phys. Chem. C* **2007**, *111* (27), 10023–10028. https://doi.org/10.1021/jp0717701.

(153) Nowotny, M. K.; Sheppard, L. R.; Bak, T.; Nowotny, J. Defect Chemistry of Titanium Dioxide. Application of Defect Engineering in Processing of TiO 2 -Based Photocatalysts. *J. Phys. Chem. C* **2008**, *112* (14), 5275–5300. https://doi.org/10.1021/jp077275m.

(154) Ohno, T.; Sarukawa, K.; Tokieda, K.; Matsumura, M. Morphology of a TiO2 Photocatalyst (Degussa, P-25) Consisting of Anatase and Rutile Crystalline Phases. *J. Catal.* **2001**, *203* (1), 82–86. https://doi.org/10.1006/jcat.2001.3316.

(155) Yu, Y. Y.; Gong, X. Q. CO Oxidation at Rutile TiO2(110): Role of Oxygen Vacancies

and Titanium Interstitials. *ACS Catal.* **2015**. https://doi.org/10.1021/cs501900q.

(156) Schaub, R.; Thostrup, P.; Lopez, N.; Lægsgaard, E.; Stensgaard, I.; Nørskov, J. K.; Besenbacher, F. Oxygen Vacancies as Active Sites for Water Dissociation on Rutile TiO2(110). *Phys. Rev. Lett.* **2001**. https://doi.org/10.1103/PhysRevLett.87.266104.

(157) Schaub, R.; Wahlström, E.; Rønnau, A.; Lægsgaard, E.; Stensgaard, I.; Besenbacher, F. Oxygen-Mediated Diffusion of Oxygen Vacancies on the TiO2(110) Surface. *Science (80-.).* **2003**. https://doi.org/10.1126/science.1078962.

(158) Pabisiak, T.; Kiejna, A. Energetics of Oxygen Vacancies at Rutile TiO2(110) Surface. *Solid State Commun.* **2007**. https://doi.org/10.1016/j.ssc.2007.08.043.

(159) Diebold, U.; Madey, T. E. TiO 2 by XPS . *Surf. Sci. Spectra* **1996**. https://doi.org/10.1116/1.1247794.

(160) Pan, J. -M.; Maschhoff, B. L.; Diebold, U.; Madey, T. E. Interaction of Water, Oxygen, and Hydrogen with TiO 2 (110) Surfaces Having Different Defect Densities . *J. Vac. Sci. Technol. A Vacuum, Surfaces, Film.* **1992**. https://doi.org/10.1116/1.577986.

(161) Göpel, W.; Rocker, G.; Feierabend, R. Intrinsic Defects of TiO2(110): Interaction with Chemisorbed O2, H2, CO, and CO2. *Phys. Rev. B* **1983**. https://doi.org/10.1103/PhysRevB.28.3427.

(162) Moss, J. A.; Szczepankiewicz, S. H.; Park, E.; Hoffmann, M. R. Adsorption and Photodegradation of Dimethyl Methylphosphonate Vapor at TiO 2 Surfaces. *J. Phys. Chem. B* **2005**. https://doi.org/10.1021/jp052057j.

(163) Panayotov, D. A.; Morris, J. R. Uptake of a Chemical Warfare Agent Simulant (DMMP) on TiO 2 : Reactive Adsorption and Active Site Poisoning. *Langmuir* **2009**, *25* (6), 3652–3658. https://doi.org/10.1021/la804018b.

(164) Panayotov, D. A.; Morris, J. R. Thermal Decomposition of a Chemical Warfare Agent Simulant (DMMP) on TiO 2 : Adsorbate Reactions with Lattice Oxygen as Studied by Infrared Spectroscopy. *J. Phys. Chem. C* **2009**, *113* (35), 15684–15691. https://doi.org/10.1021/jp9036233.

(165) Zhou, J.; Varazo, K.; Reddic, J. .; Myrick, M. .; Chen, D. A. Decomposition of Dimethyl Methylphosphonate on TiO2(110): Principal Component Analysis Applied to X-Ray Photoelectron Spectroscopy. *Anal. Chim. Acta* **2003**, *496* (1–2), 289–300. https://doi.org/10.1016/S0003-2670(03)01008-0.

(166) Bermudez, V. M. Quantum-Chemical Study of the Adsorption of DMMP and Sarin on γ-Al 2 O 3. *J. Phys. Chem. C* **2007**, *111* (9), 3719–3728. https://doi.org/10.1021/jp066439g.

(167) Yang, L.; Taylor, R.; De Jong, W. A.; Hase, W. L. A Model DMMP/TiO2 (110) Intermolecular Potential Energy Function Developed from Ab Initio Calculations. *J. Phys. Chem. C* **2011**. https://doi.org/10.1021/jp1112137.

(168) Yang, L.; Tunega, D.; Xu, L.; Govind, N.; Sun, R.; Taylor, R.; Lischka, H.; Dejong, W. A.; Hase, W. L. Comparison of Cluster, Slab, and Analytic Potential Models for the Dimethyl Methylphosphonate (DMMP)/TiO2(110) Intermolecular Interaction. *J. Phys.*

Chem. C **2013**. https://doi.org/10.1021/jp404898v.

(169) Trubitsyn, D. A.; Vorontsov, A. V. Molecular and Reactive Adsorption of Dimethyl Methylphosphonate over (001) and (100) Anatase Clusters. *Comput. Theor. Chem.* **2013**. https://doi.org/10.1016/j.comptc.2013.07.031.

(170) Sholl, D. S.; Steckel, J. A. *Density Functional Theory: A Practical Introduction*; 2009. https://doi.org/10.1002/9780470447710.

(171) Koch, W.; Holthausen, M. C. *A Chemist's Guide to Density Functional Theory*; 2001. https://doi.org/10.1002/3527600043.

(172) Cramer, C. J. *Essentials of Computational Chemistry Theories and Models*; 2004. https://doi.org/10.1021/ci010445m.

(173) Marthinsen, A. *Https://Youtu.Be/SXvhDLCycxc*; 2016.

(174) Kresse, G.; Furthmüller, J. Efficient Iterative Schemes for Ab Initio Total-Energy Calculations Using a Plane-Wave Basis Set. *Phys. Rev. B - Condens. Matter Mater. Phys.* **1996**. https://doi.org/10.1103/PhysRevB.54.11169.

(175) Perdew, J. P.; Burke, K.; Ernzerhof, M. Generalized Gradient Approximation Made Simple. *Phys. Rev. Lett.* **1996**. https://doi.org/10.1103/PhysRevLett.77.3865.

(176) Steinmann, S. N.; Corminboeuf, C. Comprehensive Benchmarking of a Density-Dependent Dispersion Correction. *J. Chem. Theory Comput.* **2011**. https://doi.org/10.1021/ct200602x.

(177) Steinmann, S. N.; Corminboeuf, C. A System-Dependent Density-Based Dispersion Correction. *J. Chem. Theory Comput.* **2010**. https://doi.org/10.1021/ct1001494.

(178) Dudarev, S.; Botton, G. Electron-Energy-Loss Spectra and the Structural Stability of Nickel Oxide: An LSDA+U Study. *Phys. Rev. B - Condens. Matter Mater. Phys.* **1998**. https://doi.org/10.1103/PhysRevB.57.1505.

(179) Łodziana, Z. Surface Verwey Transition in Magnetite. *Phys. Rev. Lett.* **2007**. https://doi.org/10.1103/PhysRevLett.99.206402.

(180) Jeng, H. T.; Guo, G. Y.; Huang, D. J. Charge-Orbital Ordering in Low-Temperature Structures of Magnetite: GGA+U Investigations. *Phys. Rev. B - Condens. Matter Mater. Phys.* **2006**. https://doi.org/10.1103/PhysRevB.74.195115.

(181) Condon, N. G.; Murray, P. W.; Leibsle, F. M.; Thornton, G.; Lennie, A. R.; Vaughan, D. J. Fe3O4(111) Termination of α-Fe2O3(0001). *Surf. Sci.* **1994**. https://doi.org/10.1016/0039-6028(94)91360-9.

(182) Makov, G.; Payne, M. C. Periodic Boundary Conditions in Ab Initio Calculations. *Phys. Rev. B* **1995**. https://doi.org/10.1103/PhysRevB.51.4014.

(183) Crampton, A. S.; Cai, L.; Janvelyan, N.; Zheng, X.; Friend, C. M. Methanol Photo-Oxidation on Rutile TiO2 Nanowires: Probing Reaction Pathways on Complex Materials. *J. Phys. Chem. C* **2017**. https://doi.org/10.1021/acs.jpcc.7b01385.

(184) Walenta, C. A.; Crampton, A. S.; Xu, F.; Heiz, U.; Friend, C. M. Chemistry of Methanol and Ethanol on Ozone-Prepared α-Fe2O3(0001). *J. Phys. Chem. C* **2018**. https://doi.org/10.1021/acs.jpcc.8b07574.

(185) Xu, F.; Chen, W.; Walenta, C. A.; O'Connor, C. R.; Friend, C. M. Dual Lewis Site Creation for Activation of Methanol on Fe3O4(111) Thin Films. *Chem. Sci*. **2020**. https://doi.org/10.1039/c9sc06149e.

(186) Kuhlenbeck, H.; Shaikhutdinov, S.; Freund, H. J. Well-Ordered Transition Metal Oxide Layers in Model Catalysis - A Series of Case Studies. *Chemical Reviews*. 2013. https://doi.org/10.1021/cr300312n.

(187) Genuzio, F.; Sala, A.; Schmidt, T.; Menzel, D.; Freund, H. J. Interconversion of α-Fe2O3 and Fe3O4 Thin Films: Mechanisms, Morphology, and Evidence for Unexpected Substrate Participation. *J. Phys. Chem. C* **2014**. https://doi.org/10.1021/jp504020a.

(188) Mitchell, M. B.; Sheinker, V. N.; Cox, W. W.; Gatimu, E. N.; Tesfamichael, A. B. The Room Temperature Decomposition Mechanism of Dimethyl Methylphosphonate (DMMP) on Alumina-Supported Cerium Oxide - Participation of Nano-Sized Cerium Oxide Domains. *J. Phys. Chem. B* **2004**. https://doi.org/10.1021/jp035590c.

(189) Meier, M.; Hulva, J.; Jakub, Z.; Pavelec, J.; Setvin, M.; Bliem, R.; Schmid, M.; Diebold, U.; Franchini, C.; Parkinson, G. S. Water Agglomerates on Fe3O4(001). *Proc. Natl. Acad. Sci. U. S. A.* **2018**. https://doi.org/10.1073/pnas.1801661115.

(190) Tian, Y.; Plonka, A. M.; Ebrahim, A. M.; Palomino, R. M.; Senanayake, S. D.; Balboa, A.; Gordon, W. O.; Troya, D.; Musaev, D. G.; Morris, J. R.; Mitchell, M. B.; Collins-Wildman, D. L.; Hill, C. L.; Frenkel, A. I. Correlated Multimodal Approach Reveals Key Details of Nerve-Agent Decomposition by Single-Site Zr-Based Polyoxometalates. *J. Phys. Chem. Lett.* **2019**. https://doi.org/10.1021/acs.jpclett.9b01002.

(191) Kim, K.; Tsay, O. G.; Atwood, D. A.; Churchill, D. G. Destruction and Detection of Chemical Warfare Agents. *Chemical Reviews*. 2011. https://doi.org/10.1021/cr100193y.

(192) Jeon, S.; Schweigert, I. V.; Pehrsson, P. E.; Balow, R. B. Kinetics of Dimethyl Methylphosphonate Adsorption and Decomposition on Zirconium Hydroxide Using Variable Temperature in Situ Attenuated Total Reflection Infrared Spectroscopy. *ACS Appl. Mater. Interfaces* **2020**. https://doi.org/10.1021/acsami.9b21846.

(193) Li, X.; Paier, J. Partial Oxidation of Methanol on the Fe 3 O 4 (111) Surface Studied by Density Functional Theory. *J. Phys. Chem. C* **2019**. https://doi.org/10.1021/acs.jpcc.8b10557.

(194) Kresse, G.; Furthmüller, J. Software VASP, Vienna. *Phys. Rev. B* **1996**.

(195) Steinmann, S. N.; Corminboeuf, C. A Generalized-Gradient Approximation Exchange Hole Model for Dispersion Coefficients. *J. Chem. Phys.* **2011**. https://doi.org/10.1063/1.3545985.

(196) Blöchl, P. E. Projector Augmented-Wave Method. *Phys. Rev. B* **1994**. https://doi.org/10.1103/PhysRevB.50.17953.

(197) Kresse G.a Joubert, D. . From Ultrasoft Pseudopotentials to the Projector Augmented-Wave Method. *Phys. Rev. B - Condens. Matter Mater. Phys.* **1999**.

(198) Anisimov, V. I.; Aryasetiawan, F.; Lichtenstein, A. I. First-Principles Calculations of the Electronic Structure and Spectra of Strongly Correlated Systems: The LDA + U Method. *Journal of Physics Condensed Matter*. 1997. https://doi.org/10.1088/0953-8984/9/4/002.

(199) Deskins, N. A.; Rousseau, R.; Dupuis, M. Distribution of Ti3+ Surface Sites in Reduced TiO2. *J. Phys. Chem. C* **2011**. https://doi.org/10.1021/jp2001139.

(200) Wang, F.; Wei, S.; Zhang, Z.; Patzke, G. R.; Zhou, Y. Oxygen Vacancies as Active Sites for H2S Dissociation on the Rutile TiO2(110) Surface: A First-Principles Study. *Phys. Chem. Chem. Phys.* **2016**. https://doi.org/10.1039/c5cp06835e.

(201) Sakamaki, K.; Itoh, K.; Fujishima, A.; Gohshi, Y. Surface Density of States of TiO 2 (110) Single Crystal and Adsorbed Molecular Observation by Scanning Tunneling Microscopy and Tunneling Spectroscopy . *J. Vac. Sci. Technol. A Vacuum, Surfaces, Film.* **1990**. https://doi.org/10.1116/1.576354.

(202) Ohno, T.; Sarukawa, K.; Tokieda, K.; Matsumura, M. Morphology of a TiO2 Photocatalyst (Degussa, P-25) Consisting of Anatase and Rutile Crystalline Phases. *J. Catal.* **2001**, *203* (1), 82–86. https://doi.org/10.1006/jcat.2001.3316.

(203) Shen, M.; Henderson, M. A. Identification of the Active Species in Photochemical Hole Scavenging Reactions of Methanol on TiO2. *J. Phys. Chem. Lett.* **2011**. https://doi.org/10.1021/jz201242k.

(204) Henderson, M. A.; Otero-Tapia, S.; Castro, M. E. The Chemistry of Methanol on the TiO2(110) Surface: The Influence of Vacancies and Coadsorbed Species. *Faraday Discuss.* **1999**. https://doi.org/10.1039/a902070e.

(205) Zhou, J.; Ma, S.; Kang, Y. C.; Chen, D. A. Dimethyl Methylphosphonate Decomposition on Titania-Supported Ni Clusters and Films: A Comparison of Chemical Activity on Different Ni Surfaces. *J. Phys. Chem. B* **2004**. https://doi.org/10.1021/jp040185m.

(206) Housaindokht, M. R.; Zamand, N. A DFT Study of Associative and Dissociative Chemical Adsorption of DMMP onto SnO2(110) Surface Nano-Cluster. *Struct. Chem.* **2015**. https://doi.org/10.1007/s11224-014-0465-8.